

Radiative capture cross sections for nuclear astrophysics in activation experiments

Dissertation

zur Erlangung des Doktorgrades
der Naturwissenschaften

vorgelegt am Fachbereich Physik
der Johann Wolfgang Goethe - Universität
in Frankfurt am Main

von

Markus Reich

geboren am 4. Juli 1987
in Frankfurt am Main

Frankfurt am Main 2022

(D30)

Vom Fachbereich Physik der
Johann Wolfgang Goethe-Universität
als Dissertation angenommen.

Dekan: Prof. Dr. Roger Erb

Gutachter: Prof. Dr. René Reifarth

Gutachter: Prof. Dr. Christoph Langer

Datum der Disputation: 15.03.2023

Abstract

In order to understand the origin of the elements in the universe, one must understand the nuclear reactions by which atomic nuclei are transformed. There are many different astrophysical environments that fulfill the conditions of different nucleosynthesis processes. Even though great progress has been made in recent decades in understanding the origin of the elements in the universe, some questions remain unanswered. In order to understand the processes, it is necessary to measure cross sections of the involved reactions and constrain theoretical model predictions. A variety of methods have been developed to measure nuclear reaction cross sections relevant for nuclear astrophysics. In this thesis, two different experiments and their results, both using the well-established activation method, are presented.

A measurement of the proton capture cross section on the p-nuclide ^{96}Ru was performed at the Institute of Structure and Nuclear Astrophysics ISNAP - Notre Dame, USA. The main goal of this experiment was to compare the results with those obtained by Mei et al. in a pioneering experiment using the method of inverse kinematics at the GSI Helmholtzzentrum für Schwerionenforschung GmbH - Darmstadt, Germany. Therefore, the activations were taken out at the same center of mass energies of 9 MeV, 10 MeV and 11 MeV. Another activation was taken out at an energy of 3.2 MeV to compare the result to a measurement of Bork et al. who also used the activation method. While the results at 3.2 MeV agree quite well with those of Bork et al., the results at higher energies show significantly smaller cross sections than those measured by Mei et al.. Experimental details, the data analysis and sources of uncertainties are discussed.

The second part of this thesis describes a neutron capture cross section experiment. At the Institut für Kernphysik - Goethe Universität Frankfurt an experimental setup allows to produce quasi maxwell-distributed neutron fields to measure maxwell-averaged cross sections (MACS) relevant for s-process nucleosynthesis. The setup was upgraded by a fast electric linear guide to transport samples from the activation to the detection site. The cyclic activation of the sample allows to increase the signal-to-noise ratio and to measure neutron captures that lead to nuclei with half-lives on the order of seconds. In a first campaign, MACS of the reactions $^{51}\text{V}(n,\gamma)$, $^{107,109}\text{Ag}(n,\gamma)$ and $^{103}\text{Rh}(n,\gamma)$ were measured. The new components of the setup aswell as the data analysis framework are described and the results of the measurements are discussed.

Kurzübersicht

Um den Ursprung der Elemente im Universum zu verstehen, muss man die Kernreaktionen verstehen, durch die Atomkerne umgewandelt werden. Es existiert eine Vielzahl von Orten im Universum an welchen die Bedingungen unterschiedlicher Nukleosyntheseprozesse erfüllt sind. Obwohl in den letzten Jahrzehnten große Fortschritte zum Verständnis der Herkunft der Elemente im Universum erzielt wurden, bleiben bis heute einige Fragen unbeantwortet. Um die Nukleosyntheseprozesse zu verstehen ist es notwendig, Wirkungsquerschnitte der beteiligten Reaktionen zu messen und damit theoretische Vorhersagen zu verbessern. Um Wirkungsquerschnitte von Reaktionen die für die Astrophysik relevant sind zu bestimmen existiert eine Vielzahl von Methoden. In dieser Arbeit werden zwei Experimente und deren Ergebnisse vorgestellt, welche beide auf der Aktivierungsmethode beruhen.

Eine Messung des Protoneneinfangquerschnitts am p-Kern ^{96}Ru wurde am Institute of Structure and Nuclear Astrophysics ISNAP - Notre Dame, USA durchgeführt. Das Hauptziel dieses Experiments war es, die Ergebnisse mit denen von Mei et al. zu vergleichen, welche die Methode der inversen Kinematik am GSI Helmholtzzentrum für Schwerionenforschung GmbH - Darmstadt, Deutschland anwendeten. Um die Ergebnisse vergleichen zu können wurden die Aktivierungen bei den gleichen Schwerpunktsenergien von 9 MeV, 10 MeV und 11 MeV durchgeführt. Eine weitere Aktivierung wurde bei einer Energie von 3,2 MeV vorgenommen, um das Ergebnis mit einer Messung von Bork et al., die ebenfalls die Aktivierungsmethode verwendeten, zu vergleichen. Während die Ergebnisse bei 3,2 MeV recht gut mit denjenigen von Bork et al. übereinstimmen, zeigen die Ergebnisse bei höheren Energien signifikant kleinere Wirkungsquerschnitte als diejenigen, welche von Mei et al. bestimmt wurden. Experimentelle Details, die Datenanalyse und auftretende Unsicherheiten werden diskutiert.

Der zweite Teil dieser Arbeit beschreibt ein Experiment zur Bestimmung von Neutroneneinfangquerschnitten. Am Institut für Kernphysik der Goethe-Universität in Frankfurt ermöglicht ein experimenteller Aufbau die Erzeugung näherungsweise maxwellverteilter Neutronenfelder zur Messung von maxwell-gemittelten Wirkungsquerschnitten (MACS), die für die Nukleosynthese im s-Prozess relevant sind. Der Aufbau wurde um eine elektrische Linearführung erweitert, um Proben von der Aktivierungsposition vor einen Detektor zu transportieren. Die zyklische Aktivierung der Proben ermöglicht es, das Signal-zu-Rausch-Verhältnis zu erhöhen und Neutroneneinfänge zu messen, welche Kerne mit Halbwertszeiten in der Größenordnung von Sekunden produzieren. In einer ersten Messkampagne wurden MACS der Reaktionen $^{51}\text{V}(n,\gamma)$, $^{107,109}\text{Ag}(n,\gamma)$ und $^{103}\text{Rh}(n,\gamma)$ bestimmt. Die neuen Komponenten des Aufbaus sowie das Datenanalyse-Framework werden beschrieben und die Ergebnisse der Messungen mit bereits existierenden Daten verglichen und diskutiert.

Contents

1	Introduction	1
1.1	Nucleosynthesis of the elements	1
1.1.1	Primordial nucleosynthesis	1
1.1.2	Stellar fusion	2
1.1.3	Galactic cosmic rays	3
1.1.4	Nucleosynthesis beyond iron	3
1.2	Aims and objectives	6
1.2.1	Proton capture on ^{96}Ru	6
1.2.2	Cyclic neutron activations	9
2	Methods	11
2.1	Basic concepts of the activation analysis	11
2.2	Production and decay chains with branchings	14
2.3	Cyclic neutron activation analysis	18
2.4	Maxwell-averaged cross sections	21
2.5	Methods for the estimation and propagation of uncertainties	23
3	Experimental setup	25
3.1	Proton induced activation at ISNAP	25
3.1.1	Proton beam generation and transport	25
3.1.2	Target section	26
3.2	Cyclic neutron activation at IKF	27
3.2.1	Proton beam generation and transport	27
3.2.2	Target section	28
4	Postprocessing and analysis	33
4.1	Proton induced ruthenium activation	33
4.1.1	Proton capture on ^{96}Ru	33
4.1.2	Gamma spectra and peak content	34
4.1.3	Sample characterization	43
4.1.4	Beam energy	45
4.1.5	Beam intensity	46
4.1.6	Detection efficiency	47
4.1.7	Direct measurement of the $^{97g,m}\text{Rh}$ decay	51
4.1.8	Measurement of the daughter nucleus ^{97}Ru decay	54
4.1.9	Estimation of uncertainties	56
4.2	Cyclic neutron activation analysis	57
4.2.1	Measured reactions	57
4.2.2	Gamma spectra and peak content	59

4.2.3	Sample characterization	62
4.2.4	Integrated neutron flux	63
4.2.5	Detection efficiency	64
4.2.6	Time dependent correction factors	68
4.2.7	Iterative approach for $^{103}\text{Rh}(n,\gamma)$	70
4.2.8	Estimation of uncertainties	74
5	Results and discussion	79
5.1	Proton induced ruthenium activation	79
5.1.1	Cross section of $^{96}\text{Ru}(p, \gamma)$	79
5.2	Cyclic neutron activation	82
5.2.1	Neutron distribution and SACS	82
5.2.2	Cross section of $^{51}\text{V}(n,\gamma)$	83
5.2.3	Cross section of $^{107}\text{Ag}(n,\gamma)$	84
5.2.4	Cross section of $^{109}\text{Ag}(n,\gamma)$	84
5.2.5	Cross section of $^{103}\text{Rh}(n,\gamma)$	85
6	Conclusion and Outlook	87
7	Zusammenfassung	89
A	Disentangled uncertainties of the $^{103}\text{Rh}(n, \gamma)$ cross section	95
B	Parameters of the CNAA analysis	99
C	Equations for the production and decay of ^{97}Ru	103
D	Impact of different geometry parameters on the simulated efficiency	107
E	Effective proton energies for the activation of ruthenium	111

List of Figures

1.1	Solar abundance distribution of the elements	2
1.2	Nucleosynthesis process paths on the chart of nuclides	3
1.3	Gamow window	7
2.1	Evolution of the produced number of nuclei during an activation experiment	13
2.2	Activity evolution of a cyclic activation experiment.	19
2.3	Time structure of a cyclic neutron activation analysis	20
2.4	Schematic drawing of the 25 keV method using the proton capture on ${}^7\text{Li}$ for neutron production.	21
2.5	Maxwell-Boltzmandistribution and ${}^7\text{Li}$ neutron distribution	23
3.1	Experimental hall of the Institute for Structure and Nuclear Astrophysics (ISNAP) - Notre Dame [49].	26
3.2	Target section for the proton activation of ${}^{96}\text{Ru}$ at ISNAP.	27
3.3	Picture of the 2.5 MV Van-de-Graaff accelerator at the Institut für Kernphysik - Goethe Universität Frankfurt.	28
3.4	Top view of the CNA A setup with explanations	30
3.5	Visualization of the target section of the CNA A setup	30
3.6	Visualization of the counting section of the CNA A setup	31
4.1	Section of the chart of nuclides around ${}^{96}\text{Ru}$	33
4.2	Measured spectra of the ruthenium activation	34
4.3	Background spectrum of the ruthenium activation	35
4.4	Measured and simulated gamma spectra for the ruthenium activation at 3.2 MeV - $E_\gamma = 700\text{-}900$ keV	36
4.5	Measured and simulated gamma spectra for the ruthenium activation at 3.2 MeV - $E_\gamma = 1400\text{-}2300$ keV	36
4.6	Measured and simulated gamma spectra for the ruthenium activation at 3.2 MeV - $E_\gamma = 100\text{-}500$ keV	37
4.7	Time evolution of the 840 keV peak for the 3.2 MeV proton activation of ruthenium.	37
4.8	Time evolution of the 879 keV peak for the 3.2 MeV proton activation of ruthenium.	38
4.9	Time evolution of the 1586.66 keV peak for the 3.2 MeV proton activation of ruthenium.	38
4.10	Time evolution of the 2246 keV peak for the 3.2 MeV proton activation of ruthenium.	39

4.11	Measured spectrum for a proton energy of 9 MeV - [Measured and simulated gamma spectra for the ruthenium activation at 3.2 MeV - $E_\gamma = 800-900$ keV	42
4.12	Time evolution of the 421.55 keV peak for the 3.2 MeV proton activation of ruthenium.	42
4.13	Time evolution of the 189 keV peak for the 3.2 MeV proton activation of ruthenium.	43
4.14	Time evolution of the 421.55 keV peak for the 9 MeV proton activation of ruthenium.	43
4.15	Picture of a ruthenium sample used for the activation with protons.	44
4.16	NMR frequencies and their corresponding proton energies	45
4.17	Simulated effective proton energy distribution considering energy loss in the ruthenium layer for an incident proton energy of 3.238 MeV.	46
4.18	Time dependent current induced by protons on the target measured with a current integrator (one pulse corresponds to 10^{-8} C).	47
4.19	Visualization of the different geometry parameters in the efficiency simulations.	47
4.20	Dead layer analysis for the HPGe detector used for the ruthenium activation	49
4.21	Analysis of the distance between the sample and the detector	49
4.22	Simulated full energy peak efficiency of the HPGe detector used for the ruthenium activation	50
4.23	FX plot for 3.2 MeV	52
4.24	FX plot for 9 MeV	53
4.25	FX plot for 10 MeV	53
4.26	FX plot for 11 MeV	54
4.27	Monte Carlo simulated PDF's for 3.2 MeV and 9 MeV	55
4.28	Time dependent evolution of ^{97}Rh , ^{97m}Rh and ^{97}Ru during and after the irradiation with protons at $E_p = 8.99$ MeV.	56
4.29	Section of the chart of nuclides around ^{51}V	57
4.30	Section of the chart of nuclides around ^{107}Ag and ^{109}Ag	58
4.31	Section of the chart of nuclides around ^{103}Rh	59
4.32	Detector rate in the clover detector during an activation. The characteristic time intervals used for the analyses are shown.	60
4.33	Accumulated clover detector energy spectrum of $^{51}\text{V}(n,\gamma)$. The 1434.06 keV gamma line of ^{52}V β^- - decay used for the analysis is marked.	60
4.34	Accumulated clover detector energy spectrum of $^{107}\text{Ag}(n,\gamma)$. The 632.98 keV gamma line of ^{108}Ag β^- - decay used for the analysis is marked.	61
4.35	Accumulated clover detector energy spectrum of $^{109}\text{Ag}(n,\gamma)$. The 657.5 keV gamma line of ^{110}Ag β^- - decay used for the analysis is marked.	61
4.36	Accumulated clover detector energy spectrum of $^{103}\text{Rh}(n,\gamma)$. The 555.81 keV gamma line of ^{104}Rh ground state β^- - decay used for the analysis is marked.	62

4.37	Sample preparation and fixation to the transport system. On the left side the ^{51}V sample is shown. The sample is kept in a central position by a polyimide foil glued to a ring of polymere. The picture on the right shows the sample transport system with an empty ring clipped to the sample holder in front of the clover detector.	63
4.38	Visualization of the Clover geometry used in the detection efficiency simulations. The activated sample is shown in orange, the inner electrode of the active (transparent) crystal in blue.	65
4.39	Comparison of the simulated and measured efficiencies for different pairs of values for the sample distance and the inner dead layer thickness. The χ^2 is used as an estimator for the deviation between simulated and measured peak contents of the calibration sources ^{137}Cs , ^{133}Ba , ^{54}Mn and ^{22}Na	66
4.40	Determination of the distance between the sample and the detector for the CNAAs efficiency simulations.	67
4.41	Determination of the radius of the inactive cylindrical volume by finding the minimum χ^2 value of the measured and simulated calibration peaks.	68
4.42	Simulated full energy peak efficiency for the CNAAs. The green dots show the ϵ_{FEP} corrected for the noise suppression applied at low energies.	68
4.43	Analysis of the dead time correction for constant rates. The points are measured values of the normalized peak content in 1173 keV of the dead time monitor ^{60}Co for different event rates in the detector.	70
4.44	Simulated evolution of the produced ^{104}Rh for two different cross section ratios	71
4.45	Calculated decays per cycle for two different cross section ratios.	72
4.46	Simulated time evolution for $^{103}\text{Rh}(n,\gamma)$	73
4.47	Best fit result for the decays per cycle for $^{103}\text{Rh}(n,\gamma)$	74
4.48	χ^2 values for pairs of σ_g and σ_m . For the sake of visualization, the maximum χ^2 value on the z-axis is set to $1.5 \cdot 10^5$	74
4.49	Monte Carlo uncertainty analysis of $^{103}\text{Rh}(n,\gamma) - \sigma_g$ and $-\sigma_m$	78
4.50	Monte Carlo uncertainty analysis of $^{103}\text{Rh}(n,\gamma) - \sigma_{tot}$	78
5.1	Results of the total reaction cross section of $^{96}\text{Ru}(p,\gamma)$ at $E_p = 9, 10, 11$ MeV	81
5.2	Results of the partial and total reaction cross sections of $^{96}\text{Ru}(p,\gamma)$ around $E_p = 3$ MeV	82
5.3	Maxwell distributions of $k_B T = 25$ keV (grey) and $k_B T = 30$ keV (green) compared with the neutron spectra in the samples for the CNAAs setup for proton energies of $E_p = 1912$ keV (red) and $E_p = 1909$ keV (orange) simulated with PINO [81].	83
7.1	Ergebnisse der partiellen und des totalen Wirkungsquerschnittes der Reaktion $^{96}\text{Ru}(p,\gamma)$ um $E_p = 3$ MeV	90
7.2	Ergebnisse der Wirkungsquerschnitte für die Reaktion $^{96}\text{Ru}(p,\gamma)$ bei $E_p = 9, 10, 11$ MeV	91

7.3	Aufbau des Lithiumtargets zur Produktion von quasi-maxwellverteilten Neutronenenergien. Goldfolien vor und hinter den Proben wurden als Monitore zur Bestimmung des integrierten Neutronenflusses verwendet.	92
7.4	Visualisierung des Aufbaus zur zyklischen Aktivierung von Proben mit Neutronen am Institut für Kernphysik IKF - Goethe Universität Frankfurt. Links hinten ist das Lithiumtarget zur Produktion von Neutronen zu sehen, welches den Abschluss des Strahlrohres bildet. Auf der rechten Seite im Vordergrund ist der Detektor innerhalb der Abschirmung aus Paraffinblöcken dargestellt. Die Probe befindet sich in der Auszählungsposition vor dem Detektor.	92
7.5	Gemessene (rot) und simulierte (blau) Zerfälle pro Zyklus unter Berücksichtigung des zeitabhängigen Neutronenflusses.	93
A.1	Simulated uncertainty in σ_{grd} and σ_{iso} for λ_{grd} rolled with a gaussian probability distribution with a $1-\sigma$ width.	95
A.2	Simulated uncertainty in σ_{grd} and σ_{iso} for λ_{iso} rolled with a gaussian probability distribution with a $1-\sigma$ width.	96
A.3	Simulated uncertainty in σ_{grd} and σ_{iso} for $\phi(t_n)$ rolled with a gaussian probability distribution with a $1-\sigma$ width for each time bin.	97
A.4	Simulated uncertainty in σ_{grd} and σ_{iso} for decays per cycle rolled with a gaussian probability distribution with a $1-\sigma$ width (statistical error of accumulated counts per cycle).	98
D.1	Impact of the inner dead layer thickness on the ε_{FEP}	107
D.2	Impact of the outer dead layer thickness on the ε_{FEP}	108
D.3	Impact of sample distance on the ε_{FEP}	108
D.4	The ε_{FEP} with and without a 2 mm absorber plate of copper.	109
E.1	Simulated effective proton energy distribution considering energy loss in the ruthenium layer for incident proton energies of 9 MeV, 10 MeV and 11 MeV.	111

List of Tables

4.1	List of measured peak contents for the ruthenium activation	40
4.2	Isotopes produced by irradiating naturally composed ruthenium with protons (Data retrieved from [67]).	41
4.3	Characteristics of the samples used for proton induced activation of ruthenium.	44
4.4	NMR frequencies, their corresponding proton energies in the laboratory and the center of mass frame, and the mean energy loss of the protons inside the ruthenium layer simulated with Geant4.	45
4.5	Simulation correction factors for all peaks used for the ruthenium activation cross section calculations.	50
4.6	Characteristic time periods together with dead time correction factors f_{DT} of the full counting periods and the distance between sample and detector during the counting period.	52
4.7	Characteristic time periods for the analysis of the ^{97}Ru decay together with dead time correction factors f_{DT} and the distance between sample and detector during the counting period.	54
4.8	Overview of the cyclic neutron activation measurements.	62
4.9	Characteristics of the samples used for the cyclic neutron activations with the samples mass m , the molar mass M , the isotopic fraction and the areal particle density μ_{areal}	63
4.10	Induced activity of the gold monitors R_1 (upstream) and R_2 (downstream) and the related integrated neutron fluxes Φ_T for all cyclic activations.	64
5.1	Results of the cross sections of $^{96}\text{Ru}(p,\gamma)^{97g,m}\text{Rh}$ for an effective proton energy of 3.165 MeV. The cross sections are listed separately for the iterative (IT), the FX approach and the direct analysis of peaks coming from isomeric and ground state decays only.	79
5.2	Results of the cross sections of $^{96}\text{Ru}(p,\gamma)^{97g,m}\text{Rh}$. The cross sections are listed separately for the iterative and the FX approach.	80
5.3	Results for the total cross sections for $^{96}\text{Ru}(p,\gamma)^{97}\text{Rh}$ determined by measuring the electron capture decay of the daughter nucleus ^{97}Ru	80
5.4	Results for the total cross sections for $^{96}\text{Ru}(p,\gamma)^{97}\text{Rh}$ of the present work calculated as the weighted mean of the FX, the IT and the ^{97}Ru decay results compared to the results of Mei et al.[64].	81
5.5	Results of the cyclic neutron activation of vanadium.	84
5.6	Results of the cyclic neutron activation of ^{107}Ag	84
5.7	Results of the cyclic neutron activation of ^{109}Ag	84
5.8	Results of the cyclic neutron activation of ^{103}Rh	85

7.1	Results for the cross sections of the cyclic neutron activation.	93
B.1	Parameters of the cyclic neutron activation of ^{51}V with their corresponding relative uncertainties in percent.	99
B.2	Parameters of the cyclic neutron activation of ^{107}Ag with their corresponding relative uncertainties in percent.	100
B.3	Parameters of the cyclic neutron activation of ^{109}Ag with their corresponding relative uncertainties in percent.	100
B.4	Parameters of the cyclic neutron activation of ^{103}Rh with their corresponding relative uncertainties in percent. The factors $f_{iter.,i}$ contain the uncertainties of the decay constants λ_i , the uncertainty of the neutron flux in every time bin $\phi(t_n)$ and the statistical uncertainty of the peak content per cycle propagated into the ground state, the isomeric and the total cross section.	101

Chapter 1

Introduction

The field of nuclear astrophysics brings together the different disciplines of theoretical astrophysics, observational astronomy, cosmochemistry and nuclear physics. One of the leading questions of nuclear astrophysics is about the origin of the elements. The modification of atomic nuclei, commonly referred to as *nucleosynthesis*, has astonishingly far-reaching consequences and leads to insights into the evolution and fate of stars like our sun and the early evolution of the universe.

A large variety of possible reactions contribute to the nucleosynthesis of atomic nuclei and take place in different astrophysical environments under distinct conditions. It is the task of experimenters to measure the properties of atomic nuclei and their reactions in the laboratory and deliver nuclear physics input for theoretical models and extensive computer simulations. These measurements take place in a variety of accelerator facilities around the world.

One of the most critical tests of nucleosynthesis models is the solar abundance of the elements and their isotopes. This distribution derived from photospheric data of the sun and the composition of chondritic meteorites can be treated as a footprint of the composition of the protosolar disk and is shown in Figure 1.1. All nucleosynthesis processes that contribute complementary to the chemical evolution of the *interstellar medium* (ISM) should quantitatively explain this distribution.

The following chapter will give an overview of important nucleosynthesis processes and their astrophysical sites. It must be noted that this overview is by no means exhaustive and that there are many other proposed processes not mentioned here. Finally, the chapter ends with the motivations for the two experiments that form the core of this thesis.

1.1 Nucleosynthesis of the elements

1.1.1 Primordial nucleosynthesis

The first nucleosynthesis process took place in the first minutes of the evolution of the universe is called *primordial nucleosynthesis* or *big-bang nucleosynthesis* BBN. After the universe had cooled down sufficiently by expanding, first fusion reactions could take place and form the first light nuclei ^2H , ^3He , ^4He and a small amount of ^7Li . The observed abundances of the light elements in early generation stars together with the *cosmic background radiation* (CMB) provide powerful tools to constrain the standard model of cosmology [69] [85].

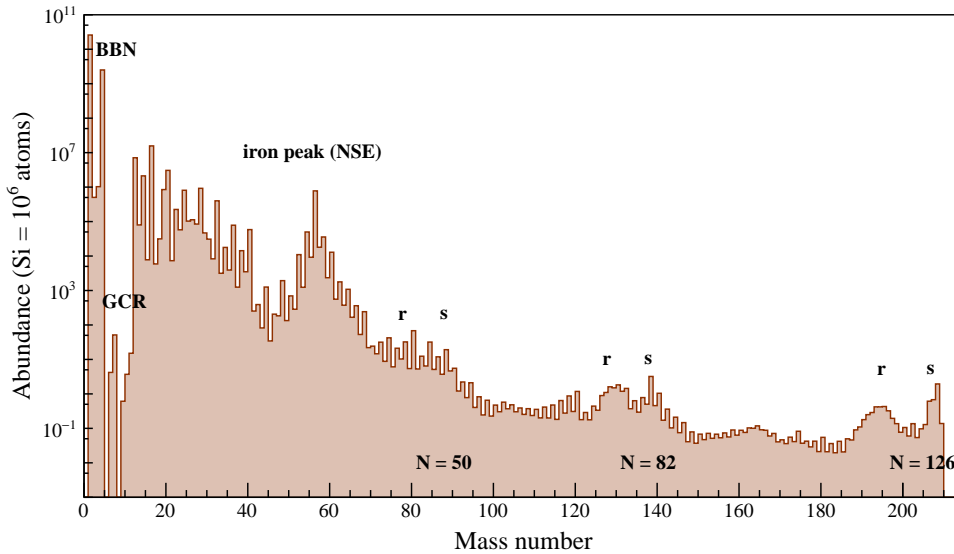


Figure 1.1: Solar abundance of the elements normalized to the abundance of silicon (Data retrieved from [61]).

1.1.2 Stellar fusion

Elements with mass numbers $A > 7$ could only be produced when the first stars were born. The gravitational collapse of a molecule cloud forms a protostar and temperature and density rise in its central region. When the temperature reaches about $T \sim 10^7$ K the *Coulomb barrier* between the light nuclei can first be overcome and fusion of hydrogen to helium ignites. There are two processes, the *proton-proton chain* (p-p chain) and the *carbon-nitrogen-oxygen cycle* (CNO cycle). The p-p chain is the dominant process in low mass stars with $M \leq M_{\odot}$ (with the solar mass $M_{\odot} = 1.998 \cdot 10^{30}$ kg) while the CNO cycle is the dominant process for stars with greater masses and core temperatures of $T > 17 \cdot 10^6$ K [89] if carbon is present as a catalyst. The fusion reactions of the light elements are *exothermic*, the mass of the products is smaller than the sum of the masses of the initial particles. This difference in mass is released as energy ($E = mc^2$) and the resulting gas and radiation pressure counters the gravitational force and keeps the star in a hydrostatic equilibrium. Depending on the initial mass of the star, fusion processes of heavier nuclei occur in later phases of the stellar evolution (*triple alpha process*, carbon burning, oxygen burning, silicon burning). The end point of the silicon burning, which takes place in the late evolution of stars with masses of $M = 8 - 11 M_{\odot}$, is ^{56}Ni , which decays via ^{56}Co into ^{56}Fe . At $A = 56$, the maximum binding energy per nucleon is reached and further fusion processes that would lead to heavier nuclei are *endothermic* and therefore do not contribute energy to keep the hydrostatic equilibrium. The nuclear fuel for the silicon burning runs out in minutes and the core starts to contract unopposed. The temperature in this phase exceeds $3 \cdot 10^9$ K and photodisintegration (γ, n), (γ, p) and (γ, α) lead to free neutrons, protons and α particles, which are captured rapidly again after their production. During this phase of *nuclear statistical equilibrium* (NSE), nuclei with low binding energies are destroyed in favor to tightly bound nuclei, which leads to an accumulation at the iron group [45]. The star ends its life in a core collapse supernova (SN Type II) and leaves behind a central object, either

a neutron star or a black hole.

In Figure 1.2, the path on the charts of nuclides of the stellar burning nucleosynthesis is indicated in orange with its end point at $A = 56$. The peak in the solar abundance distribution at the iron group is marked in Figure 1.1.

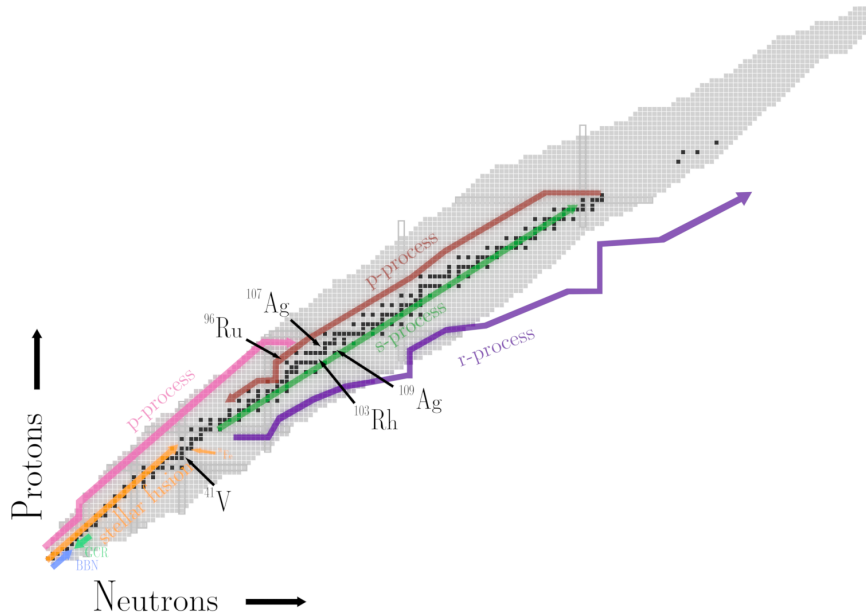


Figure 1.2: Paths of different nucleosynthesis processes on the chart of nuclides. Stable isotopes are drawn in black, unstable in gray.

1.1.3 Galactic cosmic rays

The observed abundances of Li, Be and B cannot be reproduced by taking only BBN into account. In stellar fusion environments the production of these light elements needs higher temperatures than their destruction. The production reaction of ${}^7\text{Li}$ through ${}^3\text{He}(\alpha, \gamma){}^7\text{Be}(e \nu){}^7\text{Li}$ for example runs at temperatures $T \sim 2 \cdot 10^7$ K, while its destruction through proton capture ${}^7\text{Li}(p, \alpha){}^3\text{He}$ runs at $T \sim 2 \cdot 10^6$ K [18]. The generally accepted source of ${}^6\text{Li}$, ${}^{10}\text{Be}$ and ${}^{11}\text{B}$ today is the spallation of CNO elements in the interstellar medium by *galactic cosmic rays* (GCR), mainly high energetic protons and α particles, while ${}^7\text{Li}$ was mainly produced during BBN [77]. However, until today it is not possible to reproduce the abundances of the light elements adequately and there are still open questions and discussions about alternative production mechanism like neutrino driven spallation during supernova explosions related to the production of LiBeB [57].

1.1.4 Nucleosynthesis beyond iron

It was recognized early that the coulomb repulsion suppresses the efficient production of elements heavier than iron in stellar fusion. The idea that neutron captures on a seed previously formed in stellar fusion can explain the existence and distribution of elements heavier than iron came up in the middle of the last century and is still accepted today [26]. The peak structure in the abundance of the elements (see Fig. 1.1) is a hint, that two neutron capture processes exist which differ in their

characteristic time scales and neutron densities. This peak structure has its origin in the relative stability of nuclei with closed neutron shells at $N = 50, 82, 126$. Assuming successive neutron capture and beta decay, the prominent stability of these nuclei lead to an accumulation of the abundance at strontium, barium and lead. Every peak has a neighboring peak at slightly lower mass numbers. These peaks are produced by neutron captures that occur on much shorter time scales. This leads to the production of nuclei far from stability and an accumulation at *waiting points* at closed neutron shells. The subsequent beta decays lead to the peaks, which are at lower mass numbers than those of the *slow* neutron capture process. These two neutron capture processes, the *slow* s-process and the *rapid* r-process, that are assumed to be responsible for the production of the vast majority of nuclei heavier than iron, are described in more detail in the following two chapters. After that, the production of proton-rich nuclei that cannot be produced by neutron captures is discussed.

s-process

An early s-process model was suggested by Burbidge, Burbidge, Fowler and Hoyle [26] in 1957, shortly after the discovery of the spectral profile of technetium Tc in *asymptotic giant branch* (AGB) stars by Meryill et al. in 1952 [65]. Due to the lack of details about the dynamics of the stellar processes, the phenomenological model is based on many simplifying assumptions like constant temperature and neutron density during the entire process. Despite these simplifications, this *classical* approach can reproduce the relative solar abundances of isotopes with masses of $A > 90$ in a surprisingly accurate way [53], but underestimates the production of isotopes with masses $A < 90$ significantly. This led to the assumption, that beside the *main* component which is responsible for the production of the heavy isotopes, a *weak* s-process is needed for a complete reproduction of the abundances.

As stated before, the astrophysical sites of the *main* s-process are AGB stars. After the core of a star has run out of fuel for the fusion of He, a degenerated C-O core remains. Stars with masses of $M < 10 M_{\odot}$ do not reach the temperature for carbon burning, therefore further fusion processes in the core are not possible. In a shell around the core, temperature and density are sufficient for H burning, which leads to an accumulation of He around the C-O core. Further compression and heating of the He shell ignites He burning, which explosively releases great amounts of energy. This is called *thermal pulse* (TP) and AGB stars in this phase *thermal pulsating* AGB stars (TP-AGB). The ignition of the He shell leads to zones of convection and the production of ^{13}C through the reaction $^{12}\text{C}(p,\gamma)^{13}\text{N}(\beta^+\nu_e)^{13}\text{C}$ by mixing with the H shell. The produced ^{13}C is important for the main s-process, because its alpha capture $^{13}\text{C}(\alpha,n)^{16}\text{O}$ is one of two sources of free neutrons. It takes place in the periods between two pulses, which last about 10^4 years and deliver neutron densities of $10^6 - 10^7 \text{ cm}^{-3}$ at a temperature of about $0.9 \cdot 10^8 \text{ K}$ [78].

During the short phase after the ignition of He, which lasts about some years, temperatures of about $2.5 \cdot 10^8 \text{ K}$ are sufficient to drive the reaction $^{22}\text{Ne}(\alpha,n)^{25}\text{Mg}$ which leads to fairly high neutron densities of 10^{10} cm^{-3} . Even if this neutron source only accounts for a small amount of the total neutron exposure in TP-AGB stars, it can play an important role in the resulting abundance of s-only isotopes [15].

As stated before, the main component of the s-process can reproduce only the abun-

dances of s-isotopes with $A > 90$, a complementary *weak* component can explain the major part of the production of the s-isotopes between iron Fe and strontium Sr [29]. This process is assumed to occur in massive stars with masses of $M > 10 M_{\odot}$ during their presupernova evolution phase. The main neutron production source again is $^{22}\text{Ne}(\alpha, n)^{25}\text{Mg}$, while ^{22}Ne is produced through proton capture on nitrogen and subsequent alpha capture on oxygen $^{14}\text{N}(\alpha, \gamma)^{18}\text{F}(\beta^+ \nu)^{18}\text{O}(\alpha, \gamma)^{22}\text{Ne}$, which was built during H-burning in the CNO cycle. The α capture on ^{18}O needs temperatures around $2.5 \cdot 10^8$ K and therefore the neutron production through $^{22}\text{Ne}(\alpha, n)$ becomes efficient in the end phase of He-burning at temperatures of about $3 - 3.5 \cdot 10^8$ K [73]. After the exhaustion of the He-burning, alphas produced during C shell burning through $^{12}\text{C}(^{12}\text{C}, \alpha)^{20}\text{Ne}$ keep the reaction $^{22}\text{Ne}(\alpha, n)$ running at a temperature of about $1 \cdot 10^9$ K [8]. To understand the final isotopic distribution released into the ISM, it is also important to consider the nucleosynthesis (mainly photodisintegrations) during the supernova explosion [72].

r-process

To reach the requirements of the r-process possible scenarios have to be much more extreme than those where the s-process takes place. Calculations of r-process nucleosynthesis have shown that a neutron density of about 10^{20} cm^{-3} and temperatures in the order of GK are needed to reproduce the r-process abundance [26]. Two different astrophysical sites were proposed, *core collapse supernovae* (CCSN) and *neutron star mergers* (NSM), while recent simulations lead to the assumption that the requirements for a full r-process are not reached in CCSN's ([7], [50]). In contrast, the observation of the gravitational waves of GW170817 by the LIGO and Virgo collaboration [1] in 2017 together with extensive observations with telescopes of the object could confirm the production of r-process nuclei and therefore validate NSM's as a site of r-process nucleosynthesis [59].

Nucleosynthesis network calculations of the r-process include about 5000 nuclei, most of them far from the valley of stability [40]. Neutron capture cross sections on these nuclei are usually predicted by theoretical Hauser-Feshbach (HF) statistical model calculations. While theoretical predictions of neutron capture cross sections close to stable nuclei can be reproduced in measurements within a factor of about 2, these uncertainties grow with the distance to the valley of stability to factors of 100 and even greater [59]. It is the task of future rare isotope beam facilities to measure r-process neutron capture cross sections to constrain theoretical model predictions and reduce the uncertainties of r-process calculations [79].

p-process

There exist about 35 proton-rich nuclei heavier than iron (generally referred to as *p-nuclei*) that cannot be produced through neutron capture reactions. Processes that lead to the production of these p-nuclei are summarized under the term *p-process*. Today, the generally accepted theory is that the p-nuclei are produced mainly by photodisintegrations on a seed previously formed in s- and r-process ([91], [9]). The required temperatures of about $2 - 3.5 \cdot 10^9$ K are assumed to be reached in CCSN [91] and in thermonuclear supernovae (SN Type Ia/b/c)[68], which are the most

promising sites where the p-process could take place. Close to the valley of stability, the nuclear mass flow is dominated by (γ, n) reactions and the path of the p-process on the chart of nuclides is pushed to the neutron-deficient side (see red line in Fig. 1.2). With lower neutron numbers, the neutron separation energy is rising and (γ, p) and (γ, α) reactions are dominating the nuclear mass flow. Nuclear network model calculations can reproduce the abundances of the p-nuclei with $A > 110$ reasonably well, but fail at the production of $^{92,94}\text{Mo}$ and $^{96,98}\text{Ru}$ significantly ([34], [74], [9]). The underproduction of these most abundant p-nuclei is still an open question and possible answers could lie in deficiencies of the astrophysical models, unconsidered astrophysical sites or the nuclear input such as the reaction rates [11]. As for the r-process, the vast majority of the nuclei involved in the p-process are unstable, and reaction rates are calculated with HF statistical model calculations. Even if it is far from reality from our point of view today to measure all about 20000 participating reaction cross sections for the p-process, the measurement of cross sections on unstable isotopes nevertheless is an important task of experimental nuclear astrophysics to constrain and test the theoretical model predictions.

1.2 Aims and objectives

1.2.1 Proton capture on ^{96}Ru

To get a complete picture of the nuclear evolution in an astrophysical scenario where p-process nucleosynthesis takes place, a huge number of nuclei and their reactions have to be considered. In core collapse supernovae the nuclear mass flow in the corresponding nuclear network is dominated by photodisintegrations (γ, n) , (γ, p) and (γ, α) , but also their inverse reactions occur [87]. For charged particle reactions the probability that a reaction takes place in an environment with a given temperature can be described by the so called *Gamow window*. The reaction rate for a pair of charged particles can be calculated by the following formula [48]:

$$\langle \sigma v \rangle = \left(\frac{8}{\pi \mu} \right)^{1/2} \left(\frac{1}{k_B T} \right)^{3/2} \int_0^\infty S(E) \exp \left(- \frac{E}{k_B T} - \sqrt{\frac{E_G}{E}} \right) dE \quad (1.1)$$

where μ is the reduced mass, $S(E)$ the astrophysical S factor and E_G the Gamow energy. The S factor was introduced with the intention of factoring out the exponential energy dependency of the total cross section resulting from the coulomb barrier and is defined as:

$$S(E) = \frac{E}{\exp(-2\pi\eta)} \sigma(E) \quad (1.2)$$

with the Sommerfeld parameter

$$\eta = \frac{Z_1 Z_2 e^2}{\hbar v} = 0.1575 \cdot Z_1 Z_2 \left(\frac{\mu}{E[\text{MeV}]} \right)^{1/2} \quad (1.3)$$

where Z_1 and Z_2 are the charge numbers of the particles involved, \hbar the reduced Planck constant and $E[\text{MEV}]$ the center of mass energy in MeV. The superposition

of the coulomb barrier penetration probability $\exp\left(-\sqrt{E_G/E}\right)$ and the probability that particles with a given energy exist defined by the high energy flank of the Maxwell-Boltzmann distribution $\exp(-E/(k_B T))$ leads to a peak for the reaction probability. This peak is called *Gamow peak* and it is shown in Figure 1.3.

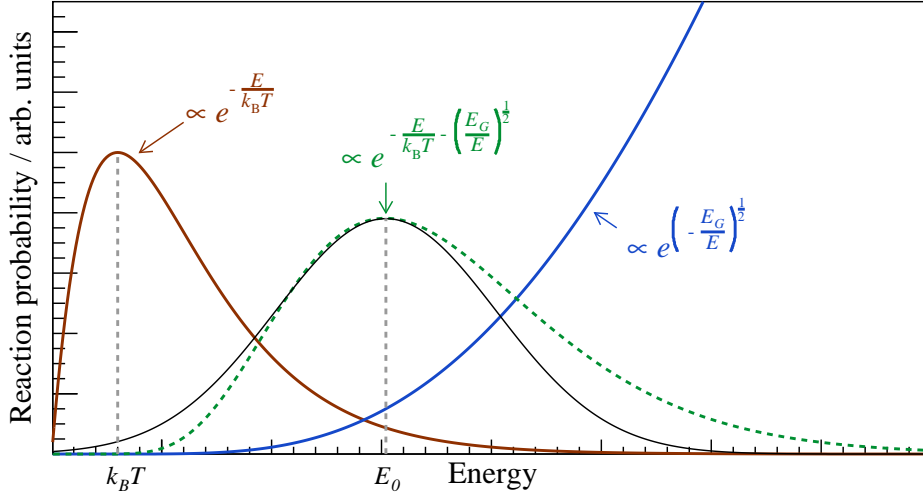


Figure 1.3: Visualization of the gamow peak that defines the energy range where charged particle reactions occur in an environment with the temperature T .

The maximum of the Gamow peak distribution can be calculated by deriving the integrand in Equation 1.1 with respect to the energy E :

$$E_0 = \left(\frac{\sqrt{E_G} k_B T}{2} \right)^{2/3}. \quad (1.4)$$

By approximating the Gamow peak with a Gaussian distribution [48]:

$$\exp\left(-\frac{E}{k_B T} - \sqrt{\frac{E_G}{E}}\right) \approx \exp\left(-\frac{3E_0}{k_B T}\right) \exp\left[-\left(\frac{E - E_0}{\Delta/2}\right)^{1/2}\right] \quad (1.5)$$

a width Δ of the Gamow window can be obtained:

$$\Delta = 4\sqrt{\frac{E_0 k_B T}{3}}. \quad (1.6)$$

The assumed temperatures in supernova explosions are between 1.8 and 3.7 GK ([76],[9]), what leads to a Gamow window for the proton capture on ^{96}Ru ranging from about 1.3 MeV to 4.3 MeV. Reaction cross sections predicted with Hauser-Feshbach statistical models are usually used as inputs for nuclear network calculations. An important goal of measurements for nuclear astrophysics is to measure the cross sections of relevant reactions in the energy range of the assumed Gamow window, thus providing a solid foundation for theoretical predictions. Since the cross sections for reactions between charged particles at low energies is small, this is not

always possible in practice due to a too high detection limit.

Applying the principle of detailed balance it is possible to calculate the reverse reaction rate of a nuclear reaction. However, the measurement of the reaction cross section in the direction with a positive Q-value (difference in mass between the products and the educts of a reaction) is preferred, because the impact of excited states which occur in the hot environment like the plasma in a star and therefore the uncertainty of the respective numeric calculations is reduced [75]. This implies, that cross section measurements of capture reactions are usually preferable to those of photodisintegrations, assuming both with the same accuracy.

With *classical* methods such as the activation method or the *in-beam* method it is challenging to perform cross section measurements on unstable isotopes. A sufficient amount of sample material has to be produced to reach a sufficient reaction rate during the irradiation in terms of the detection limit of the setup. For sufficiently long half-lives of the produced sample nuclides, this can be reached with some effort [86], but the limits are reached very quickly for shorter half-lives.

The method of *inverse kinematics* is able to overcome the limitations of the classical methods and offers the opportunity to perform cross section measurements on unstable isotopes. This method is already being used and further developed at GSI Helmholtzzentrum für Schwerionenforschung, Darmstadt (Germany) for first measurements. Two main components of the experimental setup are the *FRagment Separator* FRS, which is able to produce and separate a beam of exotic nuclei, and the *experimental storage ring* ESR in combination with a gas jet target crossing the beam in the ring. Isotopes produced due to the interaction of the beam and the gas target are identified by spatial separation in a dipole magnet and detected with double-sided silicon strip detectors (DSSSD) with a detection efficiency of close to 100%. In 2009, a first measurement of the proton capture ^{96}Ru was performed[64], followed by the measurement of the proton capture on ^{124}Xe in 2016 [83][38] and the measurement of the proton capture on ^{118}Te in 2019 (analysis still in progress [32]). With every new measurement the experimental setup as well as the data analysis is upgraded and improved. However, until today the results of these measurements could only be compared to theoretical model predictions. Because of this situation, one goal of the present thesis was to measure the proton capture cross section on ^{96}Ru at the same energies around $E_{CM} = 10\text{ MeV}$ as Mei et al. by using the well-known activation method. The same reaction was also measured by Bork et al. by means of an activation experiment at energies between 1.6 and 3.4 MeV inside the Gamow window[23]. To connect both available results the experiment was extended by one activation at a proton energy at 3.2 MeV.

1.2.2 Cyclic neutron activations

The activation method is a well-established experimental standard method to measure neutron capture cross sections at stellar neutron energies[13][44]. However, there are some limits of the method that prevent the measurement of cross sections of some reactions. The major *intrinsic* limitation is that only cross sections of isotopes that form an unstable isotope after the neutron capture are accessible with the activation method. But even if the produced isotope is unstable, limitations can occur that lead to a high detection limit:

- low amount of sample material
- limited neutron flux
- limited detection efficiency
- short half-life of the produced isotope
- low amount of radiation of the produced isotope
- long waiting time between irradiation and counting

Some of these limitations can be pushed by improving the experimental procedure. A method first mentioned by Anders et al. [6] and later described by Givens et al. [36] and Spyrou et al. [84] to improve the detection limit of an activation setup is the *Cyclic Activation Analysis* CAA. The difference to the conventional activation method is that after irradiation and subsequent counting, the samples are irradiated and counted again. Depending on the half-life of the isotope and the waiting time between irradiation and counting, the signal-to-noise SNR ratio of the summed events is increased compared to the SNR of a single activation[46]. By repeating this process and performing a cyclic activation of a sample, the detection limit and the precision of a neutron capture cross section measurement can be improved significantly.

The upgrade of the existing experimental setup for neutron activations at the Institut für Kernphysik - Goethe University Frankfurt to perform cyclic neutron activations was one of the goals of the present thesis. The new established sample transport system, the detection site and the data acquisition and analysis framework should be used for first neutron capture cross section measurements. The measurement campaign which was carried out together with Dr. Meiko Volkmandt aimed to measure the neutron capture cross sections on ^{19}F , ^{45}Sc , ^{115}In , $^{177-179}\text{Hf}$, ^{51}V , $^{107,109}\text{Ag}$ and ^{103}Rh . The analyses of the first six isotopes can be found in the work of Dr. Volkmandt [88], the analyses of the latter four isotopes are part of the present thesis.

Chapter 2

Methods

The following chapter introduces all tools and basics of the activation method that were used to determine the cross sections.

2.1 Basic concepts of the activation analysis

The main task of an activation measurement is to determine the cross section for a reaction of interest. The cross section is a measure for the probability, that a reaction occurs under given circumstances. Only reactions that lead to an unstable product are accessible for the activation method. A nuclear reaction can be written as $A(b, c)D$, where A is a target nucleus which is getting bombarded by incident particles b . The nucleus A converts to the product nucleus D , and a light particle c is emitted through the exit channel. Typical timescales in which nuclear reactions with incident particle energies of several keV take place are in the range of femtoseconds and shorter (10^{-15} s). For this species of nuclear reactions it is possible to describe the reaction as a two-staged process, where in a first step after the capture of the incident particle, the nucleus absorbs all of the energy. In a second step, the excited product nucleus decays under gamma and particle emission. For particle emission, the energy in the center of mass system has to be higher than the rest mass energy of the emitted particle. These capture cross sections are called "radiative", because the deexcitation of the product nucleus leads to gamma emission. The intermediate, short-lived nucleus is called a *compound nucleus* and a model that describes compound nuclei reactions was first introduced by Nils Bohr in 1936 [21]. For reactions in which the resulting product nucleus is stable, the direct measurement of the ejectiles emitted during the prompt deexcitation of the compound nucleus makes it possible to get access to the reaction cross section. Measurements of this kind are called *in-beam*, because the prompt emitted radiation gets detected during the irradiation.

For both methods, in-beam and activation, the cross section is determined by the reaction rate R (1/s) divided by the areal particle density of the sample μ_{areal} (cm^{-2}) times the rate of incident particles Φ (1/s) (see equation 2.1).

$$\sigma_{reaction} = \frac{R}{\mu_{areal} \cdot \Phi} \quad (2.1)$$

For the determination of the reaction rate R it is necessary to understand the time dependencies of the activity of the produced isotope.

$$\frac{dN}{dt} = -\lambda \cdot N = -A \quad (2.2)$$

The activity A (1/s) is defined as the number of decays that occur in one second, and is equal to the number of the present nuclei N times a factor λ (1/s) called the decay constant. The decay constant λ is connected to the half-life $t_{1/2}$ by $\lambda = \ln(2)/t_{1/2}$, the time it takes half of an initial number of nuclei to decay.

The differential equation 2.2 can be solved by integration, which leads to the general decay law:

$$N(t) = N_0 \cdot e^{-\lambda t} \quad (2.3)$$

$$A(t) = A_0 \cdot e^{-\lambda t} \quad (2.4)$$

An activation experiment proceeds in three stages: irradiation, transport and counting. To connect the events counted with a detector to the reaction rate during the irradiation, the time dependent evolution of the activity in all three stages must be considered.

$$\frac{dN}{dt} = -\lambda \cdot N + \sigma \cdot \Phi \cdot N_0^{sample} \quad (2.5)$$

During the irradiation phase, the decay of the isotope competes with its production. Hence, the differential equation 2.2 expands with a term $\sigma\Phi N_0$, the production rate. In general N_0^{sample} , the number of present sample nuclei, is a function of time, but in many practical cases the conversion rate of the sample isotope is small compared to the number of sample nuclei, and therefore it can be assumed as constant. Solving equation 2.5 and making the assumption, that at $t = 0$ the number of the produced nuclei is zero leads to:

$$\begin{aligned} N_{produced}(t_b) &= \frac{\sigma \cdot \Phi \cdot N_0^{sample}}{\lambda} (1 - e^{-\lambda t_b}) \\ &= \sigma \cdot \Phi \cdot N_0^{sample} \cdot f_{b,const} \end{aligned} \quad (2.6)$$

where t_b is the time of the irradiation phase and $N_{produced}$ the number of the product nuclei present at the end of the irradiation. The solution of the differential is only valid for a constant flux of incident particles ($\frac{d\Phi(t)}{dt} = 0$). In practice, this is not always the case. A varying flux of incident particles has to be taken into account by dividing the irradiation time into a sufficient amount of time intervals and solve the equation iteratively (see Equation 2.7). For the sake of clarity, time dependent correction factors f_x for the different stages are introduced.

$$\begin{aligned} N_{produced}(t_b) &= \sigma \cdot N_0^{sample} \cdot \sum_{i=0}^n \Phi_i \cdot \frac{1 - e^{-\lambda t_i}}{\lambda} \cdot e^{-\lambda t_i(n-i)} \\ &= \sigma \cdot N_0^{sample} \cdot f_b \end{aligned} \quad (2.7)$$

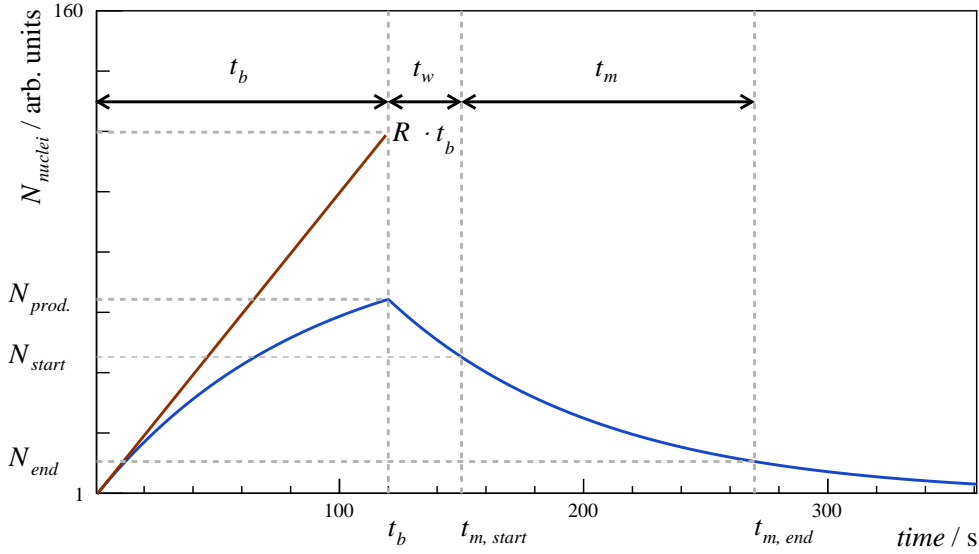


Figure 2.1: The evolution of the number of nuclei in an activation experiment depends on the production rate R , the half-life of the nucleus λ , time of irradiation t_b , waiting time t_w and counting period $t_m = t_{m,end} - t_{m,start}$. The three stages and their corresponding times are indicated by dashed lines. The red line shows the evolution of produced nuclei without decay.

After the irradiation phase, the sample gets transported to the counting site. In this phase, the produced isotopes decay without getting measured. This leads to a second time dependent correction factor f_w , where t_w is the time between the end of the irradiation phase and the beginning of the counting phase:

$$\begin{aligned} N_{decayed}(t_w) &= N_{produced} \cdot e^{-\lambda t_w} \\ &= N_{produced} \cdot f_w \end{aligned} \quad (2.8)$$

The third stage of the activation measurement is the counting phase. Integrating the solution of the free decay differential equation from the starting time of the counting phase to its end (t_m), one finds:

$$\begin{aligned} N_{counting}(t_m) &= N_{produced} \cdot e^{-\lambda t_w} \cdot (1 - e^{-\lambda t_m}) \\ &= N_{produced} \cdot f_w \cdot f_m \end{aligned} \quad (2.9)$$

In Figure 2.1 the typical time evolution of produced nuclei is shown. The common method to determine the number of nuclei decaying during the counting phase is gamma spectroscopy, where emitted photons with characteristic energies get detected. This method comes with limitations that lead to some correction factors, which allow the connection of the number of counted events C with the number of nuclei produced during the irradiation phase $N_{produced}$ (see Equation 2.10).

$$C = N_{produced} \cdot K_\gamma \cdot \epsilon_\gamma \cdot I_\gamma \cdot f_{DT} \cdot f_s \cdot f_b \cdot f_w \cdot f_m \quad (2.10)$$

The correction factors for gamma absorption K_γ , detection efficiency ϵ_γ , gamma intensity I_γ , cascade summing correction f_s and dead time f_{DT} are specific for the setup. The gamma absorption K_γ takes into account that emitted gamma radiation from the sample has to travel through sample material before reaching the active volume of the detector. By interacting with the material by photoelectric effect, Compton scattering or pair production, the incident photon can change its path and does not reach the active detector material or loses energy and therefore does not contribute to the full energy peak (or both). The index γ indicates that the factor depends on the energy of the relevant photon.

The detection efficiency ϵ_γ takes the fact into account that not all emitted photons of a sample reach the active detection volume. This depends mainly on geometrical circumstances like the distance between the sample and the detector, the solid angle coverage of the detector and the geometry of the active volume. In a gamma spectroscopy setup, only photons that deposit all of its energy inside the active volume of a detector contribute to the full energy peak. The meaning of the term *efficiency* is not unequivocal and can be used in different senses of meaning. In this thesis, whenever the term *efficiency* occurs, this refers to the full energy peak efficiency.

The gamma intensity I_γ is given by the probability, that the photon of interest gets emitted during the decay of a nuclei. In general, the deexcitation of a nucleus happens through a step-by-step deexcitation with more than one energy level involved. During such a cascade, many photons can be emitted in typical timescales of femto- to nanoseconds. If the time between the emission of two or more photons is shorter than the time resolution of the detection system (for semi-conductor germanium detectors typically in the order of nanoseconds ([30], [37]) their deposited energy adds together. This can lead to two different effects, *summing out* and *summing in*. If the photon of interest deposits its energy together with another photon of the same cascade fully or partially, the event gets registered at a higher energy and gets lost for the full energy peak. This is called *summing out*. *Summing in* happens, when the sum of two photons inside a cascade are adding together to the energy of the gamma of interest. These events contribute to the full energy peak and lead to a higher peak content.

The dead time correction factor f_{DT} takes the fact into account that for a short time period after an event was registered, the detection system is not able to detect another event. In general, the dead time correlates positively with the count rate. Finally, Equations 2.1, 2.7, 2.9 and 2.10 lead to the following equation for cross section calculation in an activation experiment:

$$\sigma = \frac{C}{\mu \cdot \phi \cdot K_\gamma \cdot \epsilon_\gamma \cdot I_\gamma \cdot f_b \cdot f_w \cdot f_m \cdot f_{DT}} \quad (2.11)$$

2.2 Production and decay chains with branchings

In the previous chapter the growth and decay of one nucleus during an activation experiment was described. There is also the case that the produced nuclide decays into a nuclide which is also unstable. Some isotopes convert through many successive decays until they reach a stable configuration. The amount of each isotope in such a chain of decays depends on their number, their half-life and the number and half-life of their mother isotope. The time-dependent evolution of a decay chain with

m involved isotopes is described by a system of differential equations (see Equation 2.12).

$$\begin{aligned}
 X_1 &\xrightarrow{\lambda_1} X_2 \xrightarrow{\lambda_2} X_3 \xrightarrow{\lambda_3} \dots \xrightarrow{\lambda_{m-1}} X_m \\
 \frac{dN_1}{dt} &= -\lambda_1 N_1 \\
 \frac{dN_2}{dt} &= -\lambda_2 N_2 + \lambda_1 N_1 \\
 \frac{dN_3}{dt} &= -\lambda_3 N_3 + \lambda_2 N_2 \\
 &\dots \\
 \frac{dN_m}{dt} &= -\lambda_m N_m + \lambda_{m-1} N_{m-1}
 \end{aligned} \tag{2.12}$$

In the year 1908, H. Bateman developed a method to find a solution for this system of differential equations describing nuclei transformation in successive decays [12]:

$$\begin{aligned}
 N_m(t) &= \lambda_1 \lambda_2 \lambda_3 \dots \lambda_{m-1} N_1(0) \sum_{i=1}^n C_i \exp(-\lambda_i t) \\
 C_i &= \prod_{j=1}^{j=n} \frac{1}{\lambda_j - \lambda_i} (i \neq j)
 \end{aligned} \tag{2.13}$$

There is only a small modification of Equation 2.13 needed if branching is taken into account. For a nuclide decaying through two channels with partial decay constants λ and λ' , the decay rate of X_1 is given by $(\lambda_1 + \lambda'_1)N_1$ and the formation rates of X_2 and X'_2 are $\lambda_1 N_1$ and $\lambda'_1 N_1$, the solution is given by:

$$\begin{aligned}
 N_m(t) &= \lambda_1^* \lambda_2^* \lambda_3^* \dots \lambda_{m-1}^* N_1(0) \sum_{i=1}^n C_i \exp(-\lambda_i t) \\
 C_i &= \prod_{j=1}^{j=n} \frac{1}{\lambda_j - \lambda_i} (i \neq j)
 \end{aligned} \tag{2.14}$$

where the λ_i^* 's represent the partial decay constant from the i 'th step in the chain to the $(i + 1)$ 'th step. In cases where many branches contribute, the solution of equations 2.12 during the irradiation gets lengthy. For the evolution of ^{97}Ru during the irradiation of ^{96}Ru with protons, the calculations can be found in Appendix C.

Some nuclei do not deexcitate promptly into their ground state after their formation, but remain in a long-lived state usually called *isomeric* state. While there is no rigid definition, half-lives of states that are stated as isomeric have half-lives that are many orders longer than typical half-lives of excited states. Isomeric states can have different channels of deexcitation. The direct decay to the ground state under gamma emission is called *internal transition* (IT), but also beta or alpha decays of isomeric states do exist.

In an activation experiment in which an isomeric state gets populated, there is not only additional emission coming from the decay of the isomeric state. If the isomeric state decays through IT to the ground state, the evolution over time of the ground state is also affected by the produced isomeric state. The system of differential equations describing the time evolution of an isomeric and ground state during an activation can be written as:

$$\begin{aligned}\frac{dN_m}{dt} &= Y_m - \lambda_m N_m \\ \frac{dN_g}{dt} &= Y_g - \lambda_g N_g + b_{IT} \lambda_m N_m.\end{aligned}\tag{2.15}$$

The branching ratio b_{IT} is given by the probability that a nuclide in the isomeric state decays through IT and feeds the ground state. The letters g and m indicate the ground state and the *metastable* isomeric state. The production yields Y_i are given by number of reactions that occur under irradiation in one second.

Using 2.13 and 2.14 and assuming a constant incident particle flux and a typical time structure of an activation experiment with an irradiation phase, a waiting phase and a counting phase, the solution of 2.15 can be written as:

$$\begin{aligned}\frac{C_m}{f_{sim,m}} &= Y_m \Lambda_3 \Lambda_6 \Lambda_9 \\ \frac{C_g}{f_{sim,g}} &= Y_g \Lambda_2 \Lambda_5 \Lambda_8 + Y_g (\Lambda_1 \Lambda_5 \Lambda_8 + \Lambda_3 \Lambda_4 \Lambda_8 + \Lambda_3 \Lambda_6 \Lambda_7).\end{aligned}\tag{2.16}$$

The factors $f_{sim,i}$ including the detection efficiency, summing corrections, absorption and the gamma intensity of the respective gamma lines. All Λ coefficients are functions of the half-lives λ_g and λ_m , the irradiation time t_b , the waiting time t_w , the counting time t_m and the IT branching b_{IT} .

$$\begin{aligned}
 \Lambda_1 &= \frac{b_{IT}}{\lambda_g} \left[1 - \frac{\lambda_m \lambda_g}{\lambda_m - \lambda_g} \left(\frac{e^{-\lambda_g t_b}}{\lambda_g} - \frac{e^{-\lambda_m t_b}}{\lambda_m} \right) \right] \\
 \Lambda_2 &= \frac{1}{\lambda_g} \left(1 - e^{-\lambda_g t_b} \right) \\
 \Lambda_3 &= \frac{1}{\lambda_m} \left(1 - e^{-\lambda_m t_b} \right) \\
 \Lambda_4 &= \frac{b_{IT} \lambda_m}{\lambda_m - \lambda_g} \left(e^{-\lambda_g t_w} - e^{-\lambda_m t_w} \right) \\
 \Lambda_5 &= e^{-\lambda_g t_w} \\
 \Lambda_6 &= e^{-\lambda_m t_w} \\
 \Lambda_7 &= b_{IT} \left[1 - \frac{\lambda_m \lambda_g}{\lambda_m - \lambda_g} \left(\frac{e^{-\lambda_g t_m}}{\lambda_g} - \frac{e^{-\lambda_m t_m}}{\lambda_m} \right) \right] \\
 \Lambda_8 &= 1 - e^{-\lambda_g t_m} \\
 \Lambda_9 &= 1 - e^{-\lambda_m t_m}
 \end{aligned} \tag{2.17}$$

By rearrangement it is possible to bring Equation 2.16 into a linear equation of the form ([55], [3]):

$$\begin{aligned}
 F &= X \cdot Y_m + Y_g \\
 F &= \frac{C_{peak}}{f_{sim,g} \Lambda_2 \Lambda_5 \Lambda_8}, X = \frac{(\Lambda_1 \Lambda_5 \Lambda_8 + \Lambda_3 \Lambda_4 \Lambda_8 + \Lambda_3 \Lambda_6 \Lambda_7) + \frac{f_{sim,m}}{f_{sim,g}} \Lambda_3 \Lambda_6 \Lambda_9}{\Lambda_2 \Lambda_5 \Lambda_8}.
 \end{aligned} \tag{2.18}$$

The measured peak content C_{peak} consists of the sum of the isomeric and the ground state contents $C_g + C_m$. By performing measurements with different irradiation, waiting and/or counting times it is possible to get pairs of (F, X) , which contain the information of the time evolution of the measured peak. By linear fitting of the data in the FX -plane, one can obtain the production yields to the isomeric (slope) and the ground state (y intercept) and therefore the cross section ratio.

Another approach that is used in the present thesis for calculating productions and decays with branchings offers the iterative calculation of the number of decays that occur during a measuring phase. For this method the experimental time is divided into a sufficient amount of time steps. In the case with an isomer that feeds the ground state through IT, the equations are given by:

$t = 0 :$

$$N_m^0 = 0$$

$$N_g^0 = 0$$

$0 < t < t_b :$

$$N_m^i = Y_m^i + N_m^{i-1} e^{-\lambda_m t_{step}} \quad (2.19)$$

$$N_g^i = Y_g^i + N_g^{i-1} e^{-\lambda_g t_{step}} + b_{IT} \lambda_m N_m^{i-1} e^{-\lambda_m t_{step}}$$

$t_b < t < t_{m,end} :$

$$N_m^i = N_m^{i-1} e^{-\lambda_m t_{step}}$$

$$N_g^i = N_g^{i-1} e^{-\lambda_g t_{step}} + b_{IT} \lambda_m N_m^{i-1} e^{-\lambda_m t_{step}}$$

Under the condition that the time steps t_{step} are short compared to the half-lives of the involved decays, this approximation is in a good agreement with the analytical approach. The number of decays N_{decays} that occur during a measurement phase $t_m = t_{m,end} - t_{m,start}$ is given by:

$$\sum_{i=t_{m,start}}^{t_{m,end}} A_{m,g}^i = \sum_{i=t_{m,start}}^{t_{m,end}} \lambda_{m,g} N_{m,g}^i = N_{decays} \quad (2.20)$$

Together with the iterative calculation of the evolution of the number of nuclei over time, a χ^2 Minimization was used to determine values for production yields and efficiency simulation parameters. The estimator in a general form is given by Equation 2.21.

$$\chi^2 = \frac{(X_{meas} - X_{sim})^2}{X_{sim}} \quad (2.21)$$

The minimum of χ^2 was determined by varying the input parameters of interest.

2.3 Cyclic neutron activation analysis

In an activation experiment, the number of produced nuclei is limited by the number of incident particles, the half-life of the nuclei of interest and the time of irradiation. Looking at Figure 2.1 and Equation 2.7 it turns out, that for a given number of incident particles and a given half-life, the number of produced nuclei runs into saturation and further expanding of the time of irradiation does not lead to a significant increase in produced nuclei. The following waiting time reduces the produced number of nuclei before the detection phase begins. For short lived nuclei combined

with low production cross sections, this can lead to an insufficient amount of counts in the detector by means of statistical uncertainty and detection limit.

A method to increase detectable events is the so called *Cyclic Activation Analysis* (CAA) or, if the incident particles are neutrons, the *Cyclic Neutron Activation Analysis* (CNAA). In Figure 2.3 the time structure of a cyclic activation is shown. The duration of one full cycle t_c is introduced as another characteristic time for the analysis. The formalism of CAA and possible advantages were described in detail by Spyrou and Given et al. ([84], [36]).

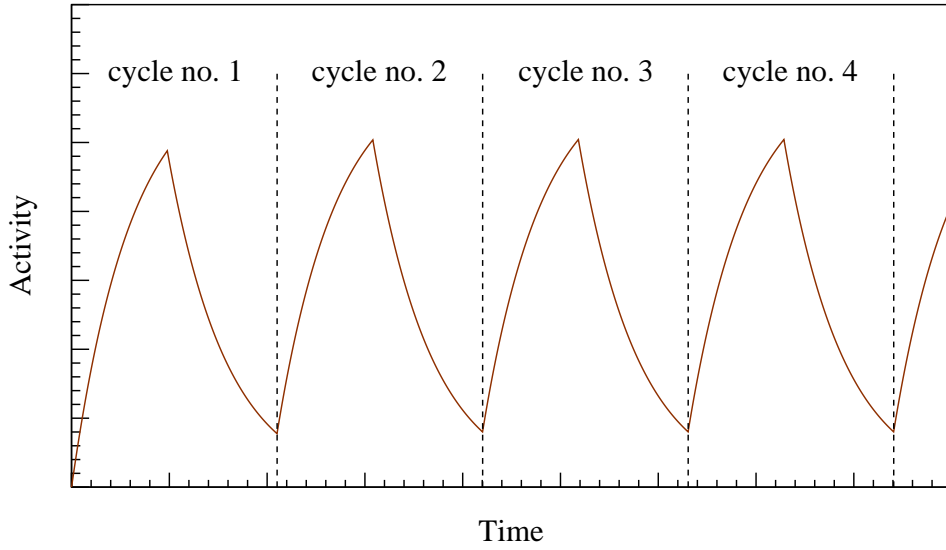


Figure 2.2: Activity evolution of a cyclic activation experiment.

The detector response for the first cycle C_1 is just the same as the one of a single activation discussed previously:

$$C_1 = \frac{\mu_{areal}\sigma\phi I_\gamma\epsilon}{\lambda}(1 - e^{-\lambda t_b})e^{-\lambda t_w}(1 - e^{-\lambda t_m}). \quad (2.22)$$

Assuming a constant production rate, for the second cycle, the detector response consists of the part produced during the second irradiation in addition to what's left of the first cycle:

$$C_2 = C_1(1 + e^{-\lambda t_c}). \quad (2.23)$$

For the n 'th cycle, the contributions of all previous cycles has to be considered:

$$C_n = C_1(1 + e^{-\lambda t_c} + e^{-2\lambda t_c} + e^{-3\lambda t_c} + \dots + e^{-(1-n)\lambda t_c}). \quad (2.24)$$

For the cumulative detector response C_{sum} , the detector responses of all cycles have to be summed up:

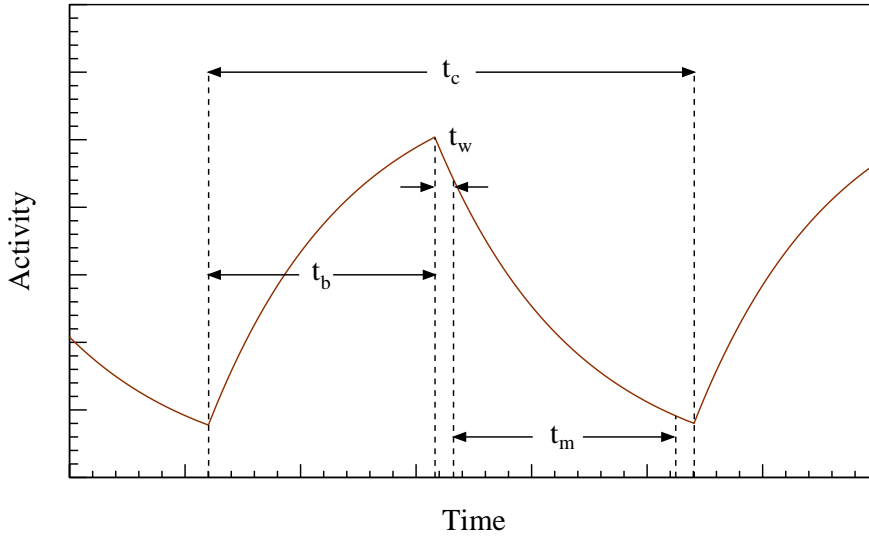


Figure 2.3: Time structure of a cyclic activation analysis. The evolution of the activity over time is shown together with the characterizing time windows t_b (time of irradiation), t_w (waiting time, where the sample gets transported from the activation site to the detection site), t_m (time window for counting) and t_c (the time of a full cycle).

$$\begin{aligned}
 C &= \sum_{i=1}^n C_i \\
 &= C_1 \left[\frac{n}{1 - e^{-\lambda t_c}} - \frac{e^{-\lambda t_c} (1 - e^{-n\lambda t_c})}{(1 - e^{-\lambda t_c})^2} \right] \\
 &= \frac{\mu_{areal} \phi \sigma I_\gamma \epsilon}{\lambda} \left[\frac{n}{1 - e^{-\lambda t_c}} - \frac{e^{-\lambda t_c} (1 - e^{-n\lambda t_c})}{(1 - e^{-\lambda t_c})^2} \right] \\
 &\quad \times (1 - e^{-\lambda t_b}) e^{-\lambda t_w} (1 - e^{-\lambda t_m})
 \end{aligned} \tag{2.25}$$

Equation 2.25 is only valid for a constant reaction rate during the irradiation phase and therefore only for a constant neutron flux. Assuming a constant neutron flux within every single cycle, but allowing different integrated neutron fluxes $\Phi_{T,i}$ for the cycles, results in the final expression for the cross section calculation in CAA:

$$\sigma = \frac{C_{sum}}{\mu_{areal} \Phi_T K_\gamma \epsilon_\gamma I_\gamma f_b f_w f_m f_{DT} f_s f_c} \tag{2.26}$$

where Φ_T is the full integrated neutron flux of the activation. The factor f_c contains all dependencies of the cycle time t_c and the integrated neutron flux per cycle $\Phi_{T,i}$ and is defined as follows:

$$f_c = \left(1 - \frac{\sum_{i=1}^k \Phi_T^i e^{-\lambda(k-i)t_c}}{\sum_{i=1}^k \Phi_T^i} \cdot e^{-\lambda t_c} \right) \cdot \frac{1}{1 - e^{-\lambda t_c}}. \quad (2.27)$$

2.4 Maxwell-averaged cross sections

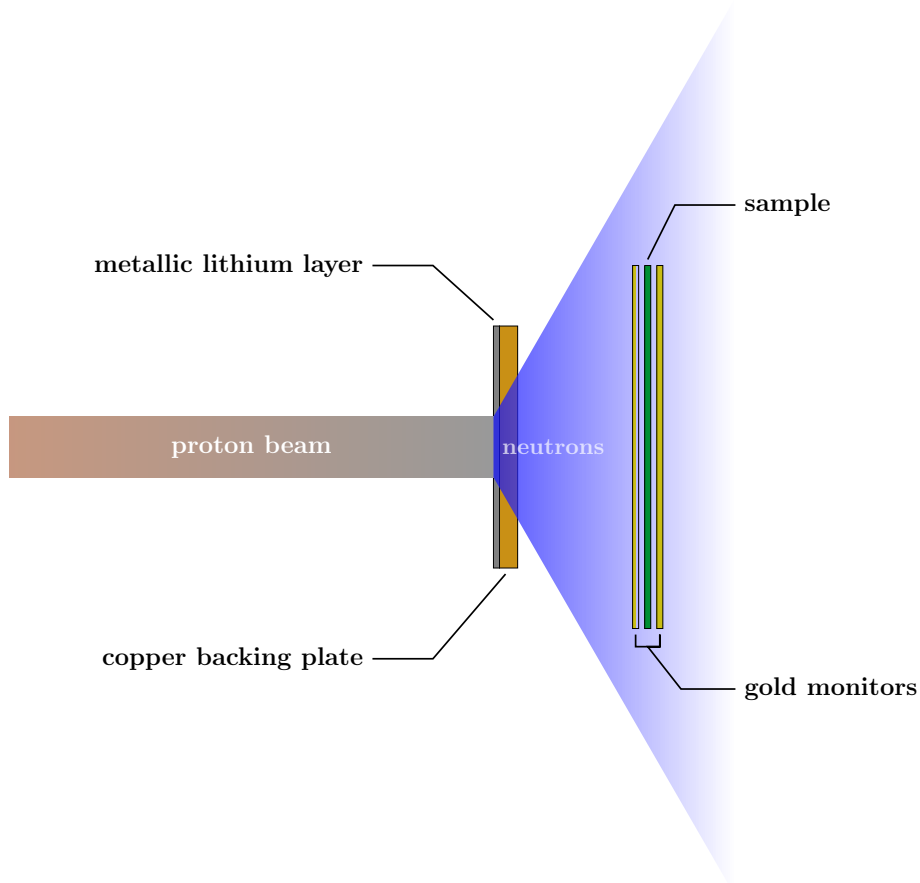


Figure 2.4: Schematic drawing of the 25 keV method using the proton capture on ${}^7\text{Li}$ for neutron production.

The neutrons produced in an astrophysical environment undergo many collisions before getting captured. Thus they are getting thermalized, and their energies follow a Maxwell-Boltzmann distribution (MB) (see Equation 2.28).

$$\Phi(E_n) = \frac{dN}{dE_n} \sim \sqrt{E_n} e^{-\frac{E_n}{k_b T}}$$

Φ := Maxwell-Boltzmann distribution
 E_n := Neutron energy
 N := Number of neutrons with energy E_n
 k_b := Boltzmann factor = $1.380649 \cdot 10^{-23} \frac{\text{J}}{\text{K}}$
 T := Temperature

(2.28)

A crucial parameter to determine the reaction rate between particles with masses m_1 and m_2 in an astrophysical environment with the temperature T is the *maxwell-averaged cross section* (MACS), that is defined by[78]:

$$\langle \sigma \rangle (k_B T) = \frac{\langle \sigma v \rangle}{v_T} = \frac{2}{\sqrt{\pi}} \frac{1}{(k_B T)^2} \int_0^\infty \sigma(E) E \exp\left(-\frac{E}{k_B T}\right) dE \quad (2.29)$$

where v_T is the most probable velocity for a given temperature $v_T = \sqrt{k_B T / \mu}$ with the reduced mass $\mu = m_1 \cdot m_2 / (m_1 + m_2)$. There are different neutron production reactions that offer the opportunity to produce quasi MB distributed neutron energies for different temperatures. By bombarding a metallic lithium target with protons the reaction ${}^7\text{Li}(p,n){}^7\text{Be}$ delivers a neutron energy distribution close to the MB with a temperature of $k_B T = 25$ keV [53]. For a proton energy of $E_p = 1912$ keV the neutron energy distribution is in a good agreement with the MB at $k_b T = 25$ keV (see Figure 2.5). Due to the fact that the proton energy lies just slightly above the neutron production threshold of $E_p = 1880.57(8)$ keV, the neutrons are kinematically boosted in forward direction creating a cone with an opening angle of 120° [13]. The setup for an activation with neutrons produced by the reaction ${}^7\text{Li}(p,n){}^7\text{Be}$ is shown in Figure 2.4.

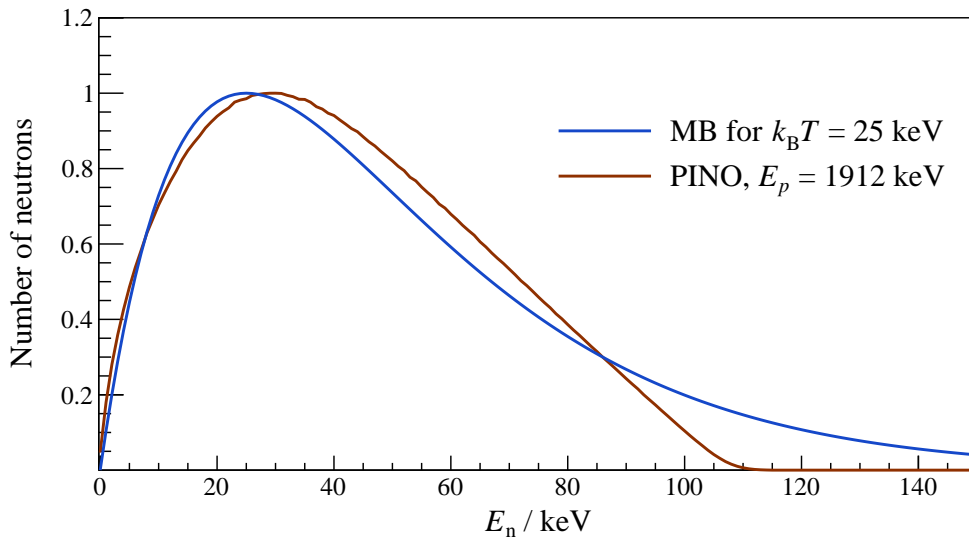


Figure 2.5: Comparison of a Maxwell-Boltzmann distribution for $k_B T = 25$ keV and the energy distribution of neutron produced by ${}^7\text{Li}(p,n){}^7\text{Be}$. The neutron energy spectrum was simulated with the simulation tool *protons in neutrons out* (PINO) [81] using a proton energy spread of 2 keV, a distance between lithium target and sample of 1 mm, a sample radius of 10 mm and a lithium layer thickness of 30 μm .

2.5 Methods for the estimation and propagation of uncertainties

The uncertainty of the result of an experiment is no less important than the value itself. A major underlying concept of science is the reproducibility of results. When researchers are getting the same results independently of each other, each using their own methods, reproducibility is achieved. But when can we say that the results are the *same*? In reality, a repeated measurement would never lead to the *exact* same result in the sense of infinite precision. Disturbances are responsible for a variance in the result of repeated experiments. This leads to an *uncertainty* corresponding to the measured result. The Joint Committee for Guides in Metrology offers the following definition of uncertainty[41]:

“parameter, associated with the result of a measurement, that characterizes the dispersion of the values that could reasonably be attributed to the measurand”

There are many different types and sources of possible uncertainties that can contribute to a result such as finite instrument resolution, a bias in the reading of an analogue display or the unknown impact of environmental conditions. A classification of different sources of uncertainties can be found in *Guide to the expression of uncertainty in measurement GUM* published by the Joint Committee for Guides in Metrology[41].

The uncertainties of the results of a model depends on the uncertainties of the

input parameters used for its determination. How these uncertainties propagate to the final result depends on the model and on correlations between the input parameters. The most common method used for the propagation of uncertainties was first formulated by Gauss in 1823 [35] and first suggested as a standard procedure in science and engineering by Kline in 1953 [54]. The main equation of this method in its general form is given by:

$$s_y^2 = \sum_{i=1}^m \left(\frac{\partial y}{\partial x_i} \cdot s_i \right)^2 + 2 \cdot \sum_{i=1}^{m-1} \sum_{j=i+1}^m \frac{\partial y}{\partial x_i} \frac{\partial y}{\partial x_j} s(x_i, x_j) \quad (2.30)$$

where s_y^2 is the variance in the result and s_y the related standard deviation. The second term of the equation accounts for correlations between the input parameters by considering the covariances $s(x_i, x_j)$ between each pair of the input parameters. A detailed description with its advantages and limits can be found in the *GUM*[41].

Another approach for the propagation of uncertainties in the present thesis is the Monte Carlo method. The main idea of the method is to use the probability density functions *PDF* of the uncertainties for each input parameter and draw a set of input parameter values $(x_1, x_2, x_3, \dots, x_n)$. By feeding the model with these randomly chosen parameters we gain the result of one sample. By repeating this procedure and by generating a sufficient amount of samples (typically of the order of at least 10^6 [4]) the *PDF* of the result is obtained. There are different approaches to derive the uncertainty from the resulting *PDF* depending on its distribution [58]. However, in the present thesis, all *PDF*'s of the output quantities are assumed to be gaussian with related standard deviations and mean values. A more detailed description of the Monte Carlo method for uncertainty propagation can be found in the *GUM - Supplement 2*[42].

Chapter 3

Experimental setup

The present thesis deals with two different experimental campaigns. The proton induced activation of ruthenium took place at the **I**nstitute for **S**tructure and **N**uclear **A**strophysics (ISNAP) of the University of Notre Dame - Indiana, USA. The cyclic neutron activations were performed at the **I**nstitut für **K**ernphysik (IKF) - Goethe Universität Frankfurt. The following chapters give an overview of the experimental setups.

3.1 Proton induced activation at ISNAP

3.1.1 Proton beam generation and transport

ISNAP offers numerous possibilities for particle beam productions. For the proton activations discussed in the present thesis, the FN 10 MV Tandem was used to accelerate protons extracted from a sputter ion source to energies of 3.2 MeV to 11 MeV. The general working mechanism of a tandem accelerator is similar to that of a Van-de-Graaff-Accelerator. A high *direct current* DC external voltage is charging a rubber belt, which transports positive charged ions into a hollow metal dome. A metal comb shaped electrode is connected to the dome. It allows electrons to transfer from the dome to the belt which neutralize positive charged ions. Because there is no electric field on the inside of a hollow conductor, the positive charge drifts to the outside surface of the dome. The maximum potential that is building up is limited by the corona charge leakage through the housing and is typically about 5 MV.

With a tandem accelerator like the FN 10 MV it is possible to increase the effective acceleration of charged particles by removing electrons from incident ions in the middle of the accelerator, where the potential reaches its positive maximum. This is accomplished with a carbon stripping foil placed in the middle of the acceleration path. Taking away at least two electrons of the accelerated particle can change the charge from negative to positive and therefore the force on the particle resulting from the electric field switches from attractive to repulsive, the particles travel through the potential two times. This leads to an effective potential of $2 \cdot U$ (or even greater, if more than two electrons are stripped). As an upgrade installed in the year 2000, the FN 10 MV rubber belt was exchanged by a pelletron chain consisting of cylindrical metal pellets connected by insulating nylon links. The main advantages are a higher terminal voltage stability and a higher durability compared

to the rubber belt [66].

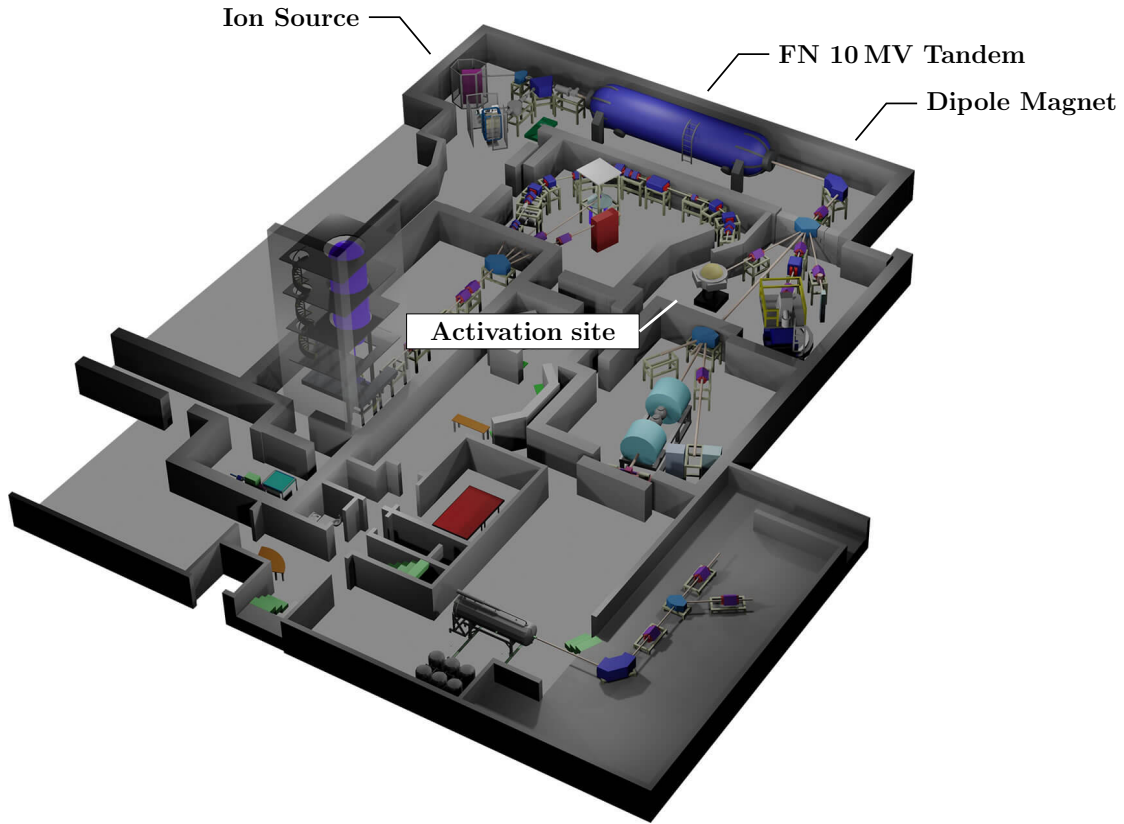


Figure 3.1: Experimental hall of the Institute for Structure and Nuclear Astrophysics (ISNAP) - Notre Dame [49].

After leaving the accelerator, the proton beam gets bent 90° by an energy analyzing dipole magnet. A second magnet guides the beam to the different experimental sites, in our case the R2D2-Beamline. Before hitting the target, the protons passing a segment of collimation and focus elements.

3.1.2 Target section

The proton activation target forms the end of the evacuated beam line. The cylindrically shaped samples with a diameter of 40 mm and a thickness of 1 mm are clamped into a sample holder that is mounted electrically isolated. To take away the heat load that is induced by the proton beam during the irradiation, the sample was cooled with a water flow on its backside. For a meaningful current measurement, a suppression voltage pushes secondary electrons back into the target chamber. The target chamber is connected to a current integrator to measure the full integrated charge and therefore the number of protons on the target and the time-dependent beam intensity. A sketch of the target section can be found in Figure 3.2.

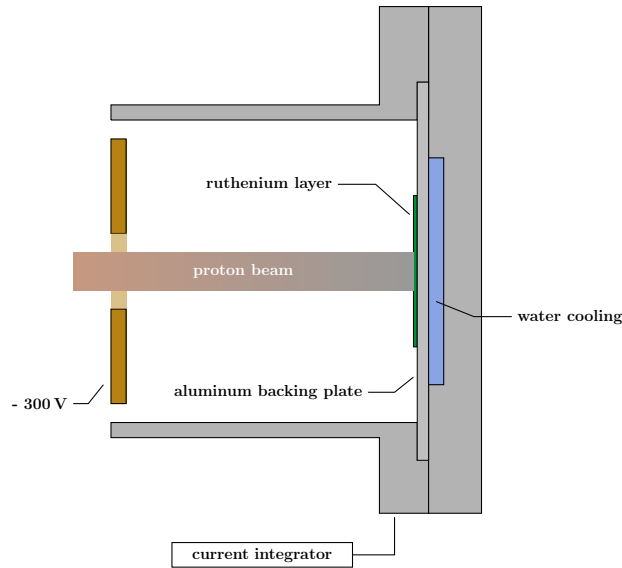


Figure 3.2: Target section for the proton activation of ^{96}Ru at ISNAP.

3.2 Cyclic neutron activation at IKF

The measurement of the neutron capture cross sections were carried out at the Institut für Kernphysik - Goethe Universität Frankfurt. Therefore, a cyclic transport of samples together with the detection and data analysis system was designed and built as an upgrade of the existing neutron production site. Details of the main elements of the setup are described in the following chapters.

3.2.1 Proton beam generation and transport

The protons are extracted from a *high frequency* (HF) ion source and accelerated with a single-ended electrostatic 2.5 MV Van-de-Graaff accelerator to the required energies of 1912 keV (see Fig. 3.3). An energy analyzing dipole ensures a narrow energy distribution at the target position with a spread of about 2 keV. With quadrupole lens magnets it is possible to focus the beam on the target position without major losses. A magnetic driven shutter was used to ensure that protons hitting the lithium target only in the phases, when the sample is in the activation position.

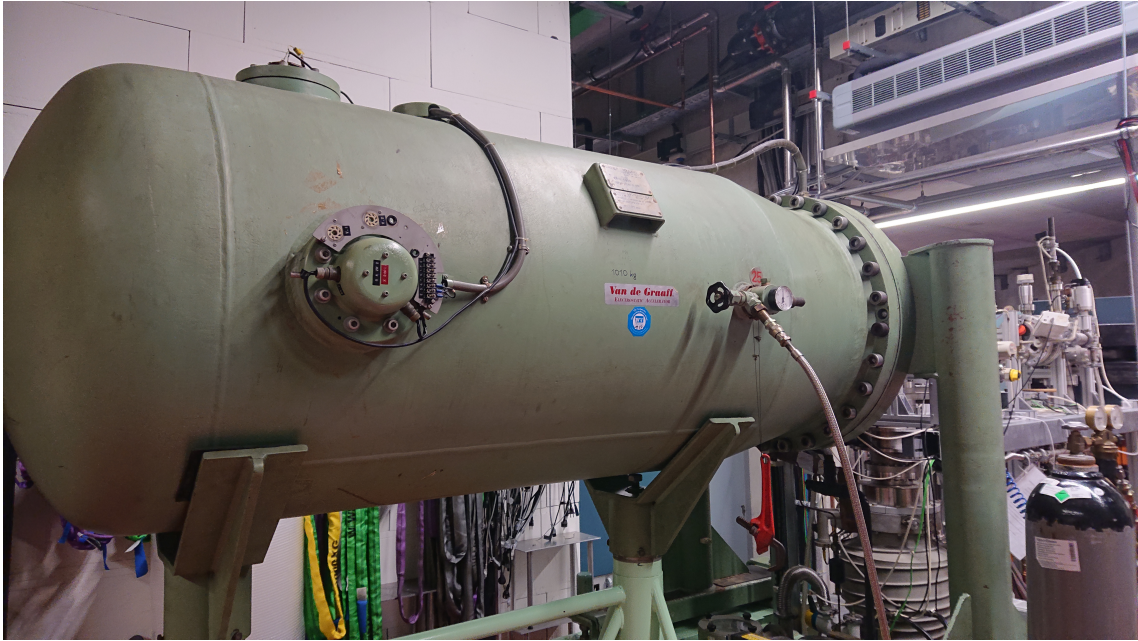


Figure 3.3: Picture of the 2.5 MV Van-de-Graaff accelerator at the Institut für Kernphysik - Goethe Universität Frankfurt.

3.2.2 Target section

The well-established neutron activation setup at IKF that has been used for numerous experiments in the past was upgraded to fulfill the requirements of a CNA. In the following, new components and their interactions are described. An overview of the setup can be found in Figure 3.4, a closer look on the activation site in Figure 3.5 and on the counting site in Figure 3.6.

The neutron production target consists of metallic lithium layer with a thickness of $\sim 20 \mu\text{m}$ and a diameter of $\sim 5 \text{mm}$ evaporated on a copper backing plate with a thickness of 0.5mm . The backing plate is soldered in a copper socket, that is connected to a water cooling system to take away the deposited heat load during the irradiation to prevent damage and degradation of the lithium layer. The neutron production target is mounted electrically isolated and connected with a *current integrator* (CI) to monitor the proton beam intensity on the target. The sample holder connected to the slide is designed in the form of a gallows to minimize the material which is inside the neutron cone during the activation. Beside the sample it carries two gold monitors, one in front of the sample and one behind it. These monitors are used to determine the full integrated neutron flux for the activation. In a distance of about 80cm behind the target, a *lithium glass* (Li-Glass) detector is mounted. In a Li-Glass detector, neutrons are captured through the reaction ${}^6\text{Li}(n,\alpha){}^3\text{H}$. The products of the reaction, e.g. the α particle and the triton do have only short ranges of about $6 \mu\text{m}$ and $36 \mu\text{m}$ inside the Li-Glass material and by the deposition of their energy they induce scintillation light. This light can be carried with a photomultiplier and the pulse height of the signal is proportional to the characteristic energy of the neutron capture reaction [63]. Because the rate of this signal is proportional to the neutron flux, the Li-Glass allows to monitor the time-dependent neutron flux.

The *linear guide control system* (LGCS) together with the electrically driven linear guide takes a crucial position in the setup by being responsible for the cyclic transport of the samples between the activation and the counting site. Furthermore, it fulfills the function of an independent master that determines the chronological sequence of the experiment. The *timing control system* (TCS) records the end point positions of the sample transport slide with position sensors at the activation and the counting site (PSA and PSC in Fig. 3.4). This information is used to open and close the shutter and therefore to make sure that neutrons are only produced when the sample is in the activation position. In addition, it provides timing information to the Data Acquisition DAQ, produces an event protocol of the timing structure and delivers the opportunity of live monitoring. For signal processing at the TCS a *general purpose input/output* (GPIO) interface with maximum square wave frequency of 70 kHz was used, an input output delay of less than 0.1 ms could be achieved.

On the counting site an n-type coaxial *high purity germanium* (HPGe) detector was installed to measure the gamma radiation of the activated samples. In an n-type HPGe, the germanium lattice is doped with donor impurities of the 5th group, typically arsenic or phosphorus. The impurities deliver additional weakly bounded valence electrons, which contribute to charge transport as a majority. Compared with p-type HPGe's, one advantage of n-type HPGe's is the lower sensitivity to radiation damage caused by neutrons [70]. The clover detector was surrounded by a lithium-enriched paraffin shielding of 10 cm thickness to prevent scattered neutrons from reaching the detector (see Fig.3.6). Paraffin as a hydrocarbon compound has a high cross section for neutron scattering and therefore thermalizes the neutrons quickly. Once thermalized, the high thermal capture cross section of ${}^6\text{Li}(n,\alpha)$ causes an effective absorption of the neutrons.

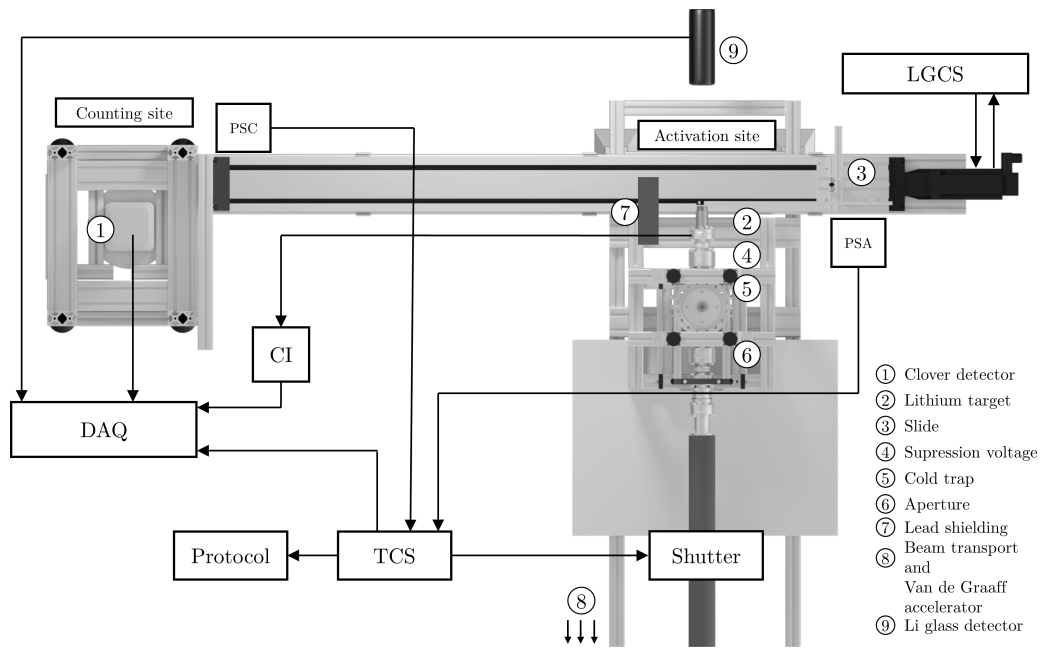


Figure 3.4: Top view of the CNA Setup at the IKF. The arrows indicate the signal paths of the communication between the linear guide control system (LGCS), the timing control system (TCS), the current integrator (CI), the lithium glass detector(9), the shutter and the data aquisition system (DAQ).

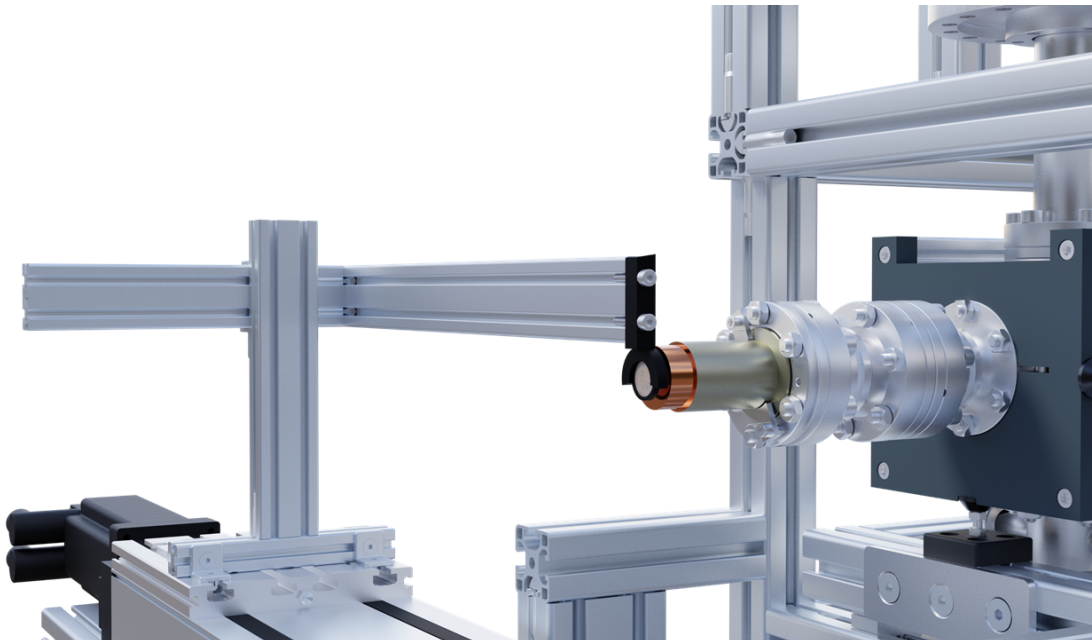


Figure 3.5: Visualization of the target section for cyclic neutron activation. The slide is in activation position with the sample in front of the neutron production target.

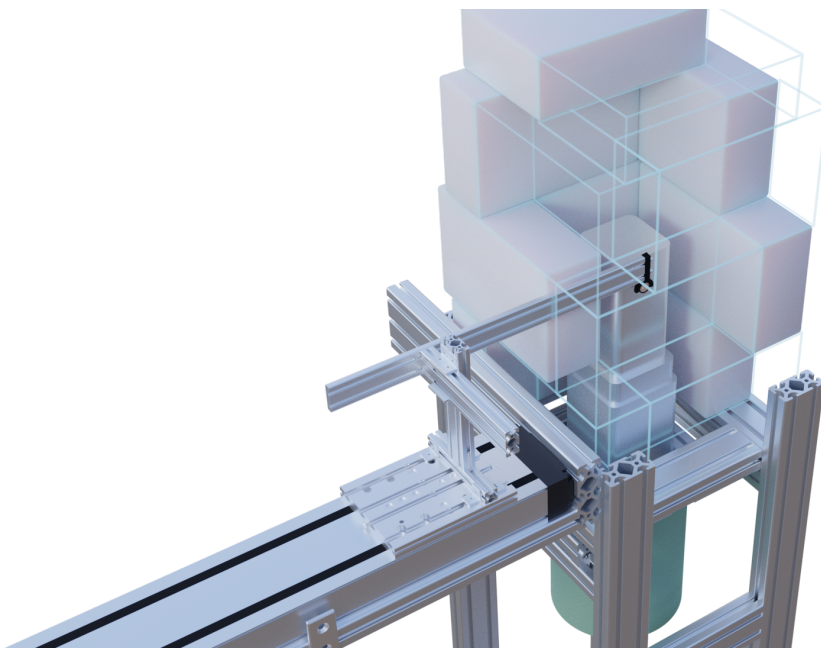


Figure 3.6: Visualization of the counting section for cyclic neutron activation. The slide is in counting position with the sample right in front of the clover detector.

Chapter 4

Postprocessing and analysis

4.1 Proton induced ruthenium activation

In the following section, the data analysis for the proton activation of ruthenium is presented. The aim of the section is to illustrate the extraction of all parameters needed for the cross section calculation from the measured data.

4.1.1 Proton capture on ^{96}Ru

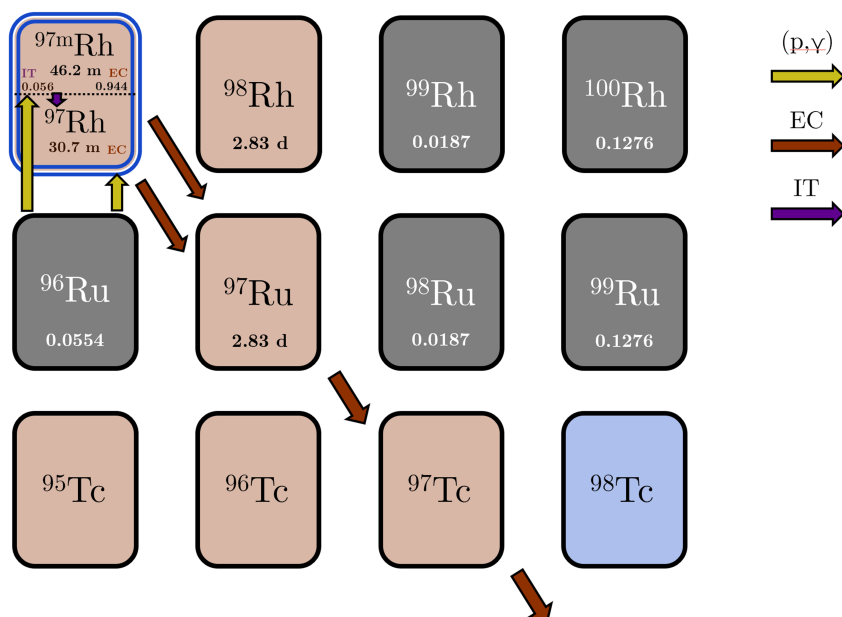


Figure 4.1: Section of the chart of nuclides around ^{96}Ru .

The path of the proton capture reaction on ^{96}Ru is shown in Figure 4.1 on the chart of nuclides. After the capture of a proton, the produced ^{97}Rh nucleus can deexcitate directly into the ground state or into an isomeric state with an excitation energy of 258.76 keV. The ground state of ^{97}Rh is undergoing an electron capture decay with a half-life of 30.7 min and converts into ^{97}Ru . The isomeric state of ^{97}Rh has a half-life of 46.2 min and branches into two different decay paths, an electron capture into ^{97}Ru with a probability of 94.4% and an internal transition into the ground

state with a probability of 5.6%. The three different reaction paths all lead to the daughter nucleus ^{97}Ru , which itself undergoes an electron capture with a half-life of 2.83 d and converts into ^{97}Tc .

Both electron capture decays of ^{97}Rh and the electron capture decay of ^{97}Ru lead to a sufficient amount of gamma radiation and therefore make it possible to measure the production cross section into the ground and the isomeric state of ^{97}Rh in an activation experiment. The gamma spectra and peak contents of the measurements will be discussed in the next chapter.

4.1.2 Gamma spectra and peak content

The number of decays was determined by counting the events in the peaks at the characteristic energies. For the identification of the peaks nuclear data was used [67]. To prevent systematic deviations in the measured peak contents one must ensure that there is no contribution of other decays to the peak content. The activation of naturally isotopic composed ruthenium with protons leads to many different produced isotopes with their own decay characteristics. Table 4.2 shows a (incomplete) list of reactions that possibly occur during the irradiations together with their produced isotopes, their half-lives and their reaction thresholds. In Figure 4.2 the measured spectra of the activations at proton energies of 3.2 MeV and 9 MeV are shown. In an energy range of 200 - 2500 keV more than 500 peaks could be identified.

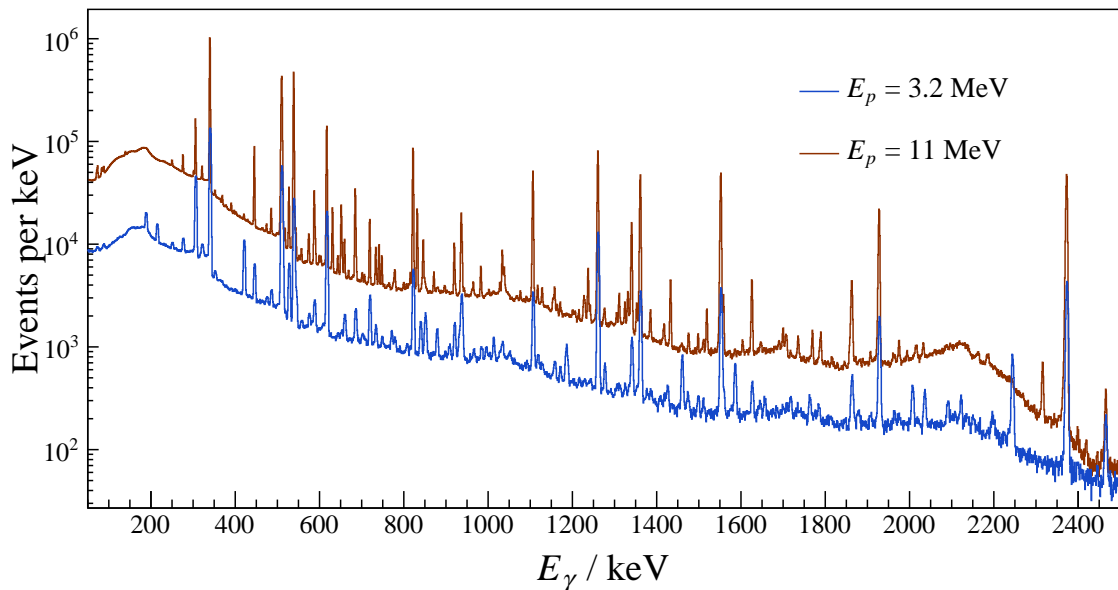


Figure 4.2: Measured spectra of the ruthenium activation for a proton energy of 3.2 MeV (blue) and 11 MeV (red).

The applied strategy to identify significant contributions of other decays inside the peaks of interest consists of three steps. In the first step, the environmental radiation at the detection site was measured with an empty setup without any sample. The taken spectrum for a measurement of 10 hours is shown in Figure 4.3. With this information it could be ensured that there is no significant contribution to any

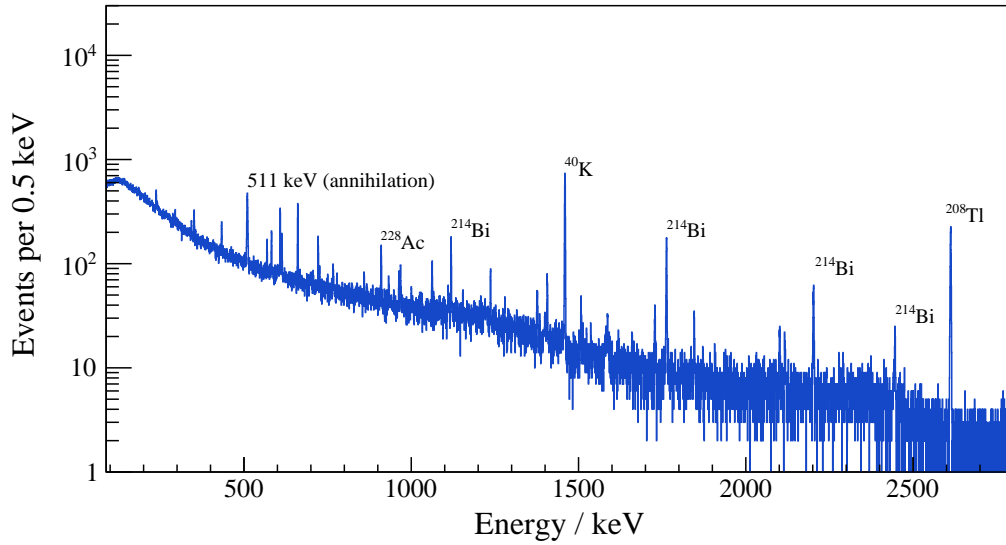


Figure 4.3: Background spectrum measured with the HPGe detector at ISNAP. Prominent peaks of the thorium and uranium decay series are labeled.

peak content that was used for the analysis.

In a second step, the simulations of the detection setup (see more in Chapter 4.1.6) were used to produce spectra of all possible decays of isotopes that could be produced during the irradiations. By broadening the simulated data with the detector energy resolution this method allows to identify overlapping peaks efficiently. Another advantage of this method is that for close detector geometries also peaks originating from cascade summing can be identified. Figure 4.6, 4.4 and 4.5 show a selection of the simulated spectra together with the measured spectra at a proton energy of 3.2 MeV. For the reason of clarity, not all spectra are shown.

In a third step of the peak identification, the evolution over time of all peaks used for the analysis was examined. Within the limits of uncertainties of the respective half-lives and the fits applied to the measured data, this can give a hint if there is any significant contribution to a peak of a nucleus with a different half-life.

Peaks coming from ground state and isomeric state could be identified and used for the analysis separately for the activation at a proton energy of 3.2 MeV. The peaks at energies of 840.13 keV and 878.8 keV can be assigned to the ground state decay of ^{97}Rh . The identification together with simulated spectra can be found in Figure 4.4. The result of the evolution over time of the peaks led to an agreement of the measured half-life with the evaluated half-life within the limits of uncertainty. The results of the analysis are shown in Figure 4.1.2 and 4.1.2.

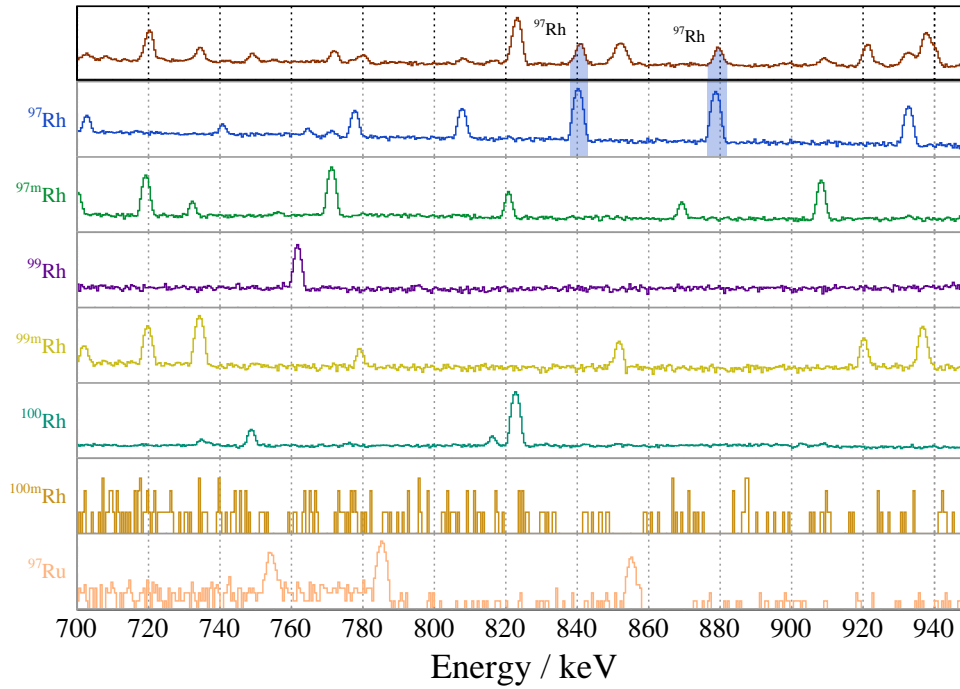


Figure 4.4: Measured gamma spectrum of the proton activation of ruthenium for a proton energy of 3.2 MeV (top red) and simulated decay spectra of isotopes produced during the irradiation. The source of the marked peaks at gamma energies of 840.13 keV and 878.80 keV is ground state electron capture decay of ^{97}Rh .

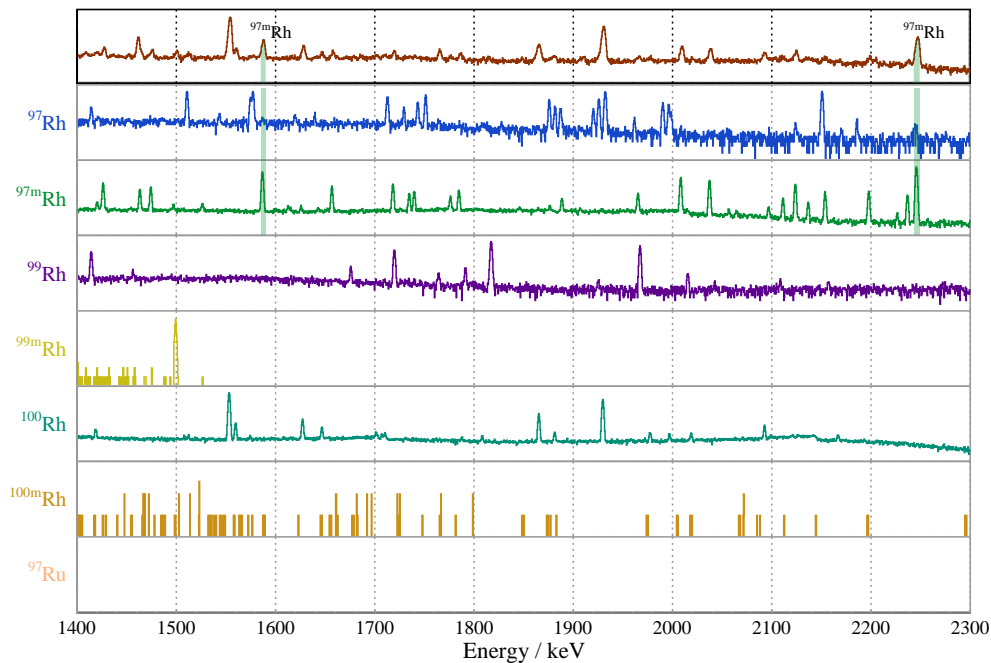


Figure 4.5: Measured gamma spectrum of the proton activation of ruthenium for a proton energy of 3.2 MeV (top red) and simulated decay spectra of isotopes produced during the irradiation. The source of the marked peaks at gamma energies of 1586.66 keV and 2245.6 keV is isomeric state electron capture decay of $^{97\text{m}}\text{Rh}$.

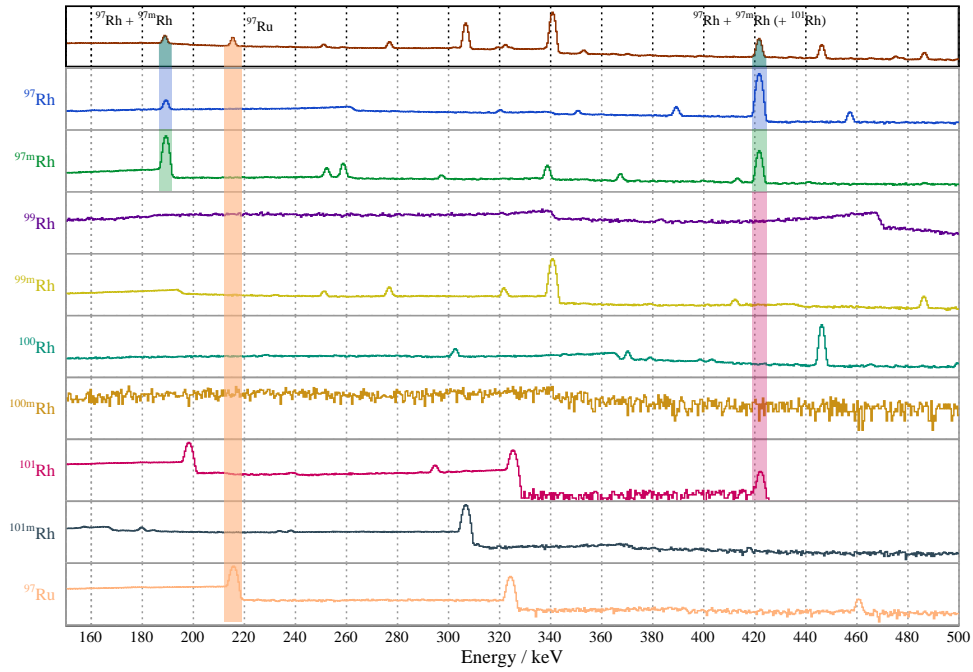


Figure 4.6: Measured gamma spectrum of the proton activation of ruthenium for a proton energy of 3.2 MeV (top red) and simulated decay spectra of isotopes produced during the irradiation. The peaks at energies of 189.21 keV and 421.55 keV contain contributions from ground state and isomeric state electron capture decay. The source of the peak at 215.7 keV is the electron capture decay of ^{97}Ru .

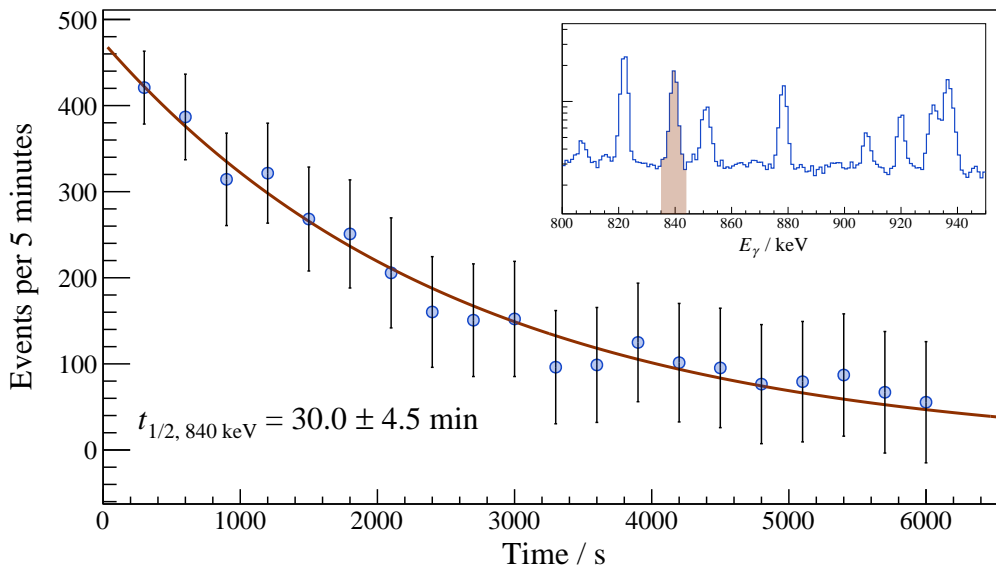


Figure 4.7: Time evolution of the 840 keV peak for the 3.2 MeV proton activation of ruthenium.

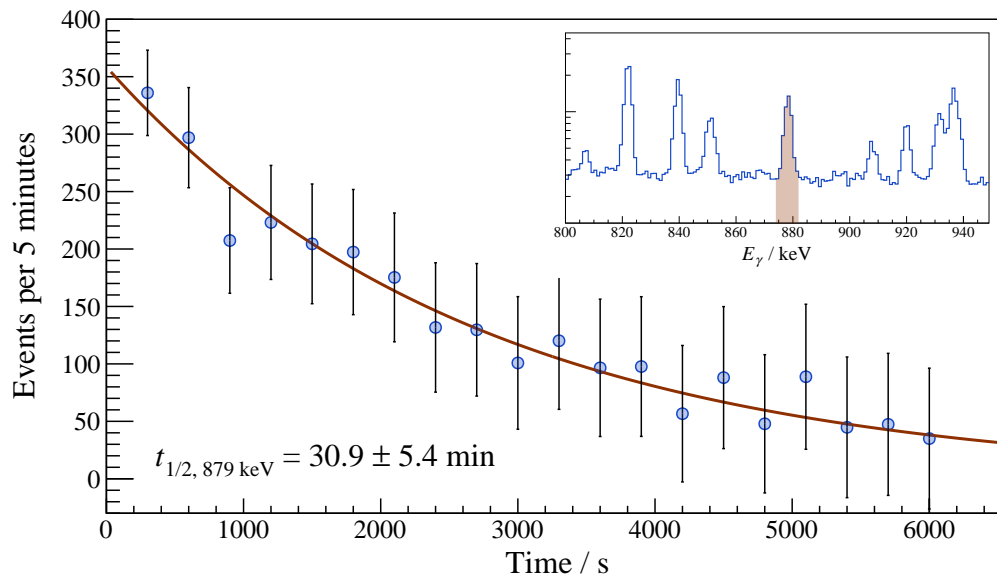


Figure 4.8: Time evolution of the 879 keV peak for the 3.2 MeV proton activation of ruthenium.

For the isomeric state, the three peaks at gamma energies of 189.21 keV (Fig. 4.6), 1586.66 keV and 2245.6 keV (Fig. 4.5) were used for the analysis. The evolution of these peaks over time are in agreement with the evaluated values for the half-life of the isomeric state and therefore no significant parasitic contribution could be identified (see Fig. 4.1.2, 4.1.2 and 4.1.2). The 189 keV receives a small contribution (<1%) from ground state decay of ^{97}Rh .

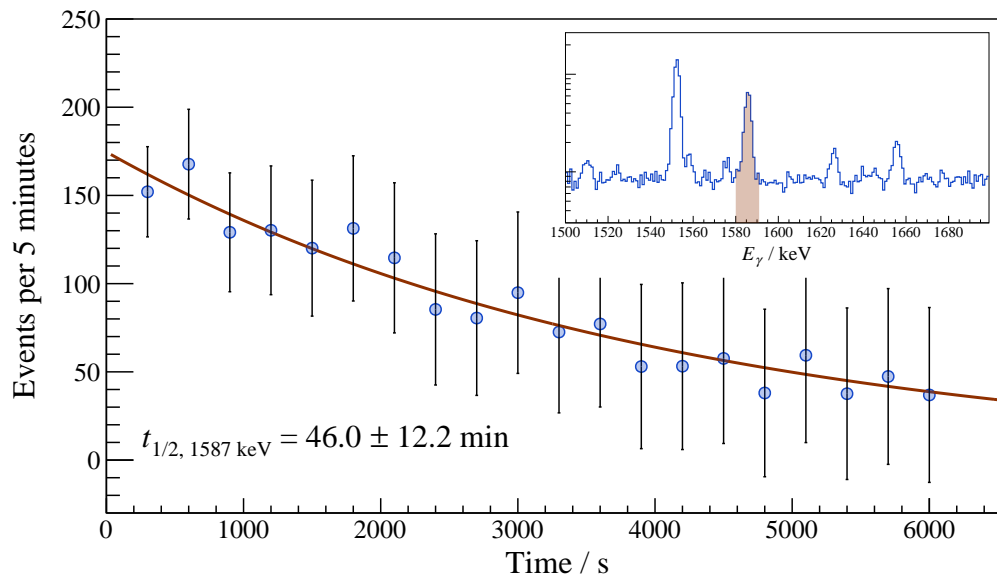


Figure 4.9: Time evolution of the 1586.66 keV peak for the 3.2 MeV proton activation of ruthenium.

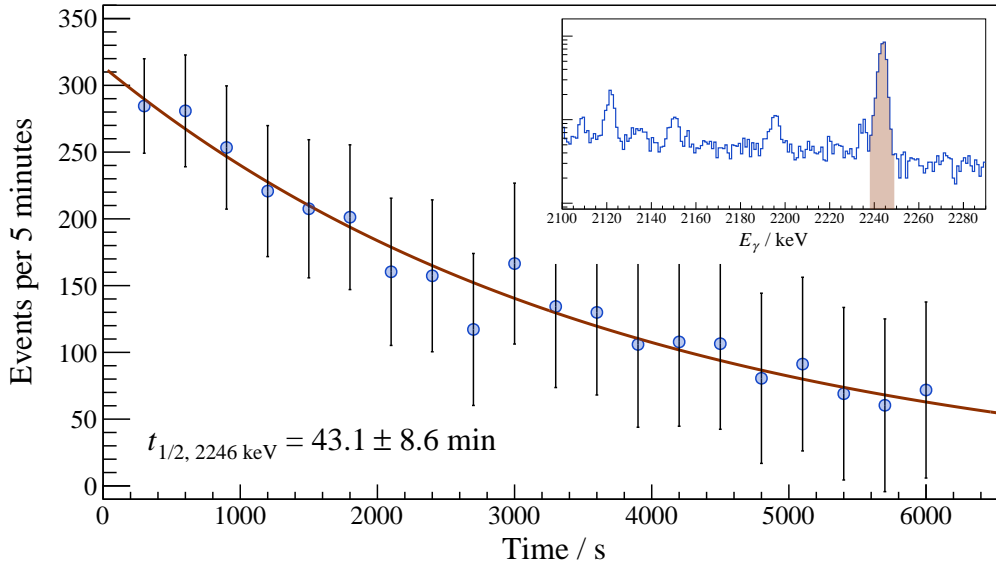


Figure 4.10: Time evolution of the 2246 keV peak for the 3.2 MeV proton activation of ruthenium.

For the activations at proton energies of 9, 10 and 11 MeV, the peak to background ratio for the peaks coming from ground state and isomeric state decays only were too low for a meaningful analysis (see Fig. 4.11). The only peak accessible was the one at 421.5 keV with contributions of ground state and isomeric decay of ^{97}Rh . The analyses of the half-life of the peak leads to a value that lies between the half-life of the ground state and the half-life of the isomeric state decay (see Fig. 4.1.2 and 4.1.2). The results of this analysis already are a hint that the cross section ratio σ_m/σ_g is bigger for the high proton energy activations than for the activation at 3.2 MeV. A more detailed analysis for the determination of the production yields into isomeric and ground state of ^{97}Rh follows in Chapter 4.1.7.

The peak contents and their corresponding statistical uncertainties can be found in Table 4.1.2.

3.2 MeV			
Source	Gamma energy	Counts	$\Delta C/C$ / %
^{97}Rh :	840.13 keV	4716	1.5
	878.80 keV	3529	1.7
^{97m}Rh :	1586.66 keV	2473	2
	2245.6 keV	4323	1.5
^{97}Rh and ^{97m}Rh :	421.55 keV	34770	0.5
9 MeV			
Source	Gamma energy	Counts	$\Delta C/C$ / %
^{97}Rh and ^{97m}Rh :	421.55 keV	7980	1.1
^{97}Ru :	215.70 keV	37940	0.5
10 MeV			
Source	Gamma energy	Counts	$\Delta C/C$ / %
^{97}Rh and ^{97}Ru :	421.55 keV	5521	1.4
^{97}Ru :	215.70 keV	10480	1
11 MeV			
Source	Gamma energy	Counts	$\Delta C/C$ / %
^{97}Rh and ^{97m}Rh :	421.55 keV	4840	1.4
^{97}Ru :	215.70 keV	27434	0.6

Table 4.1: Peak contents for all peaks together with their relative statistical uncertainties used for the cross section analysis of $^{96}\text{Ru}(p,\gamma)$. The counts in the peak at 215.70 keV coming from the decay of the daughter nuclide ^{97}Ru . The durations of the waiting and counting periods are longer than those for the measurements of the $^{97g,m}\text{Rh}$ decays (see Chapter 4.1.8).

Isotope	Reaction	Threshold	Decay mode	Half-life
⁹⁶ Rh	⁹⁶ Ru(p, n)	7.25 MeV	ε : 100%	9.9 min
^{96m} Rh	⁹⁶ Ru(p, n)	7.302 MeV	IT: 60% , ε : 40%	1.51 min
⁹⁷ Rh	⁹⁶ Ru(p, γ)	-	ε : 100%	30.7 min
^{97m} Rh	⁹⁶ Ru(p, γ)	-	IT: 5.6% , ε : 94.4%	46.2 min
⁹⁸ Rh	⁹⁸ Ru(p, n)	5.892 MeV	ε : 100%	8.72 min
⁹⁹ Rh	⁹⁸ Ru(p, γ)	-	ε : 100%	16.1 d
	⁹⁹ Ru(p, n)	2.855 MeV		
^{99m} Rh	⁹⁸ Ru(p, γ)	-	ε : 100%	4.7 hrs
	⁹⁹ Ru(p, n)	2.920 MeV		
¹⁰⁰ Rh	⁹⁹ Ru(p, γ)	-	ε : 100%	20.8 hrs
	¹⁰⁰ Ru(p, n)	4.463 MeV		
^{100m} Rh	⁹⁹ Ru(p, γ)	-	IT: 1.7% , ε : 98.3%	4.6 min
	¹⁰⁰ Ru(p, n)	4.571 MeV		
¹⁰¹ Rh	¹⁰⁰ Ru(p, γ)	-	ε : 100%	3.3 yrs
	¹⁰¹ Ru(p, n)	1.341 MeV		
	¹⁰² Ru(p, 2n)	10.652 MeV		
^{101m} Rh	¹⁰⁰ Ru(p, γ)	-	IT: 7.2% , ε : 92.8%	4.34 d
	¹⁰¹ Ru(p, n)	1.498 MeV		
	¹⁰² Ru(p, 2n)	10.809 MeV		
¹⁰² Rh	¹⁰¹ Ru(p, γ)	-	β^- : 22% , ε : 78%	207.3 d
	¹⁰² Ru(p, n)	3.136 MeV		
	¹⁰² Ru(p, 2n)	9.429 MeV		
^{102m} Rh	¹⁰¹ Ru(p, γ)	-	IT: 0.23% , ε : 99.77%	3.742 d
	¹⁰² Ru(p, n)	3.277 MeV		
	¹⁰² Ru(p, 2n)	9.570 MeV		
¹⁰⁴ Rh	¹⁰⁴ Ru(p, n)	1.937 MeV	β^- : 99.55% , ε : 0.45%	42.3 s
^{104m} Rh	¹⁰⁴ Ru(p, n)	2.066 MeV	IT: 99.87% , β^- : 0.13%	4.34 min
¹⁰⁵ Rh	¹⁰⁴ Ru(p, γ)	-	β^- : 100%	35.36 hrs
⁹⁷ Ru	⁹⁶ Rh(ε decay)	-	ε : 100%	2.83 d
	^{96m} Rh(ε decay)	-		
⁹³ Tc	⁹⁶ Ru(p, α)	-	ε : 100%	2.75 hrs
^{93m} Tc	⁹⁶ Ru(p, α)	-	ε : 22.6%, IT: 77.4%	43.5 min
⁹⁵ Tc	⁹⁸ Ru(p, α)	-	ε : 100%	20.0 hrs
^{95m} Tc	⁹⁸ Ru(p, α)	-	ε : 96.12%, IT: 3.88%	61 d
⁹⁶ Tc	⁹⁹ Ru(p, α)	-	ε : 100%	4.28 d
^{96m} Tc	⁹⁹ Ru(p, α)	-	ε : 2.00%, IT: 98.00%	51.5 min
⁹⁷ Tc	¹⁰⁰ Ru(p, α)	-	ε : 100%	4.21×10^6 yrs
	⁹⁷ Ru(ε decay)			
^{97m} Tc	¹⁰⁰ Ru(p, α)	-	ε : 3.94%, IT: 96.06%	91.0 d
	⁹⁷ Ru(ε decay)			
⁹⁸ Tc	¹⁰¹ Ru(p, α)	-	β^- : 100%	4.2×10^6 yrs
⁹⁹ Tc	¹⁰⁰ Ru(p, α)	-	β^- : 100%	2.11×10^5 yrs
^{99m} Tc	¹⁰⁰ Ru(p, α)	-	β^- : 3.7×10^{-3} %, IT: 100.0%	6.0 hrs
¹⁰¹ Tc	¹⁰⁴ Ru(p, α)	-	β^- : 100%	14.02 min

Table 4.2: Isotopes produced by irradiating naturally composed ruthenium with protons (Data retrieved from [67]).

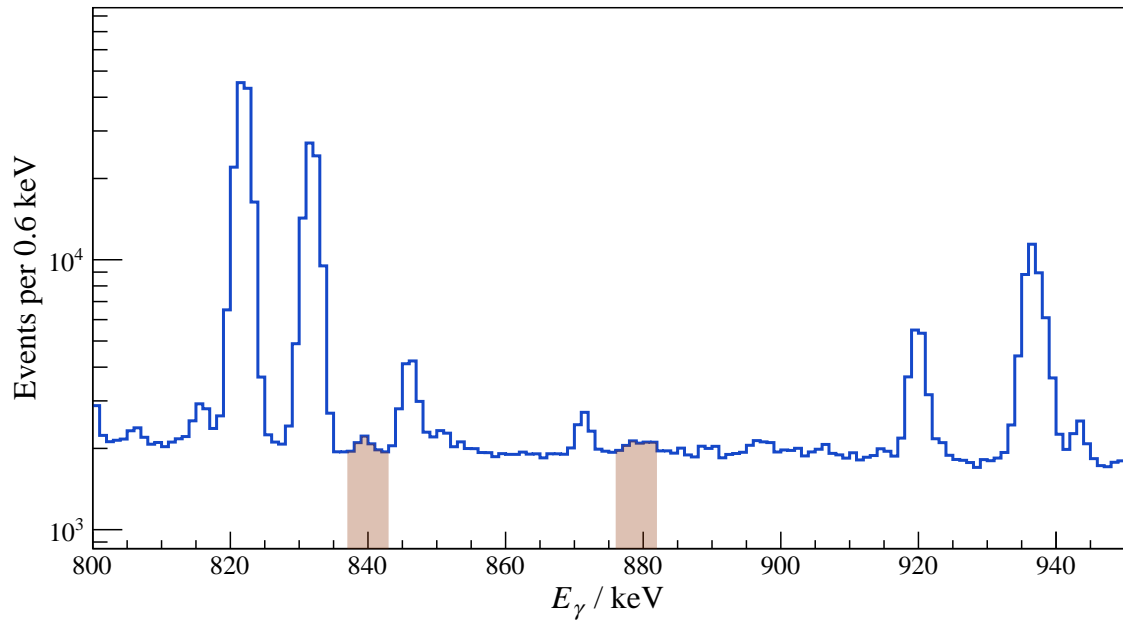


Figure 4.11: Peaks resulting from ground state decay of ^{97}Rh for a proton energy of 9 MeV at 840.13 keV and 878.8 keV. The peak to background ratio is too low for a meaningful determination of the peak contents.

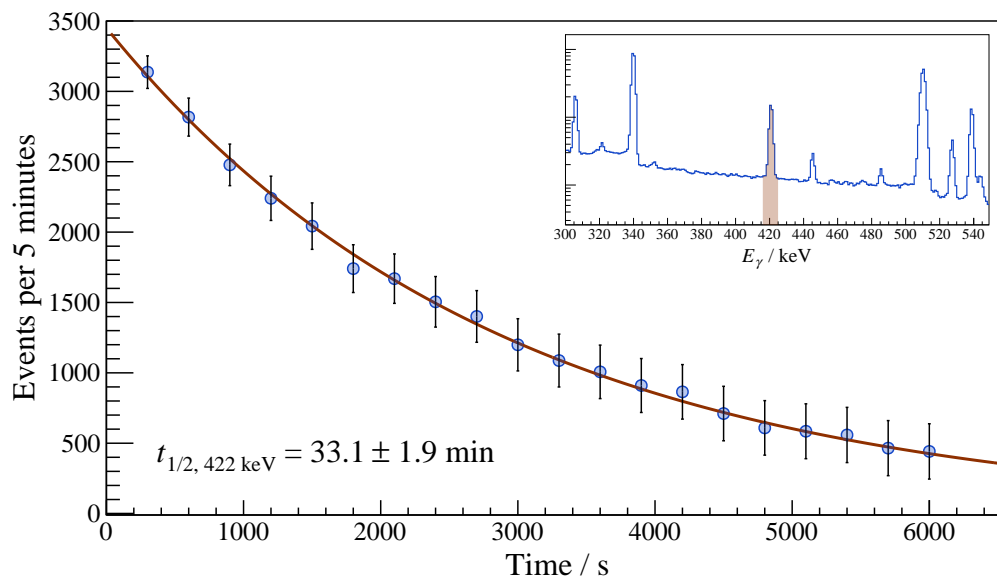


Figure 4.12: Time evolution of the 421.55 keV peak for the 3.2 MeV proton activation of ruthenium.

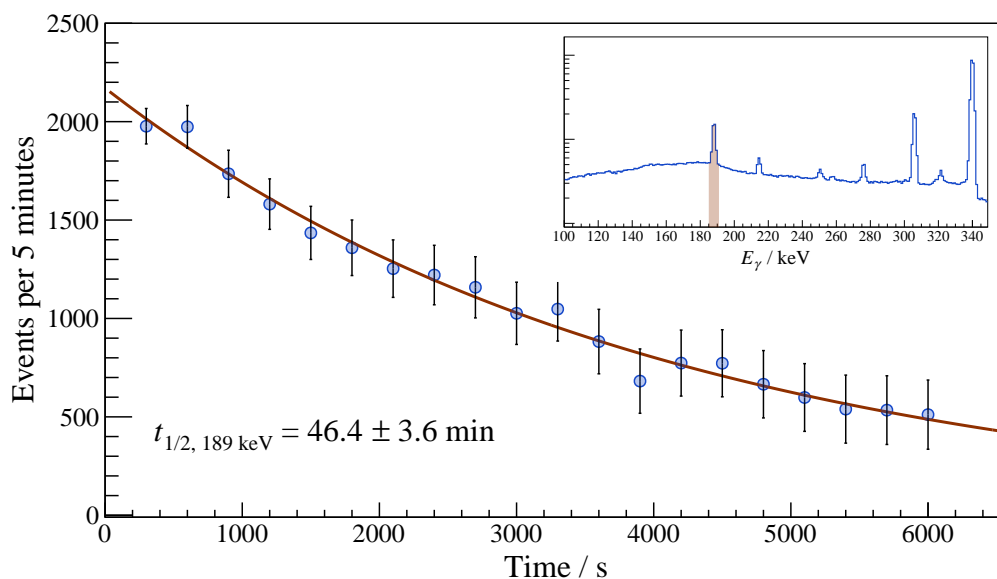


Figure 4.13: Time evolution of the 189 keV peak for the 3.2 MeV proton activation of ruthenium.

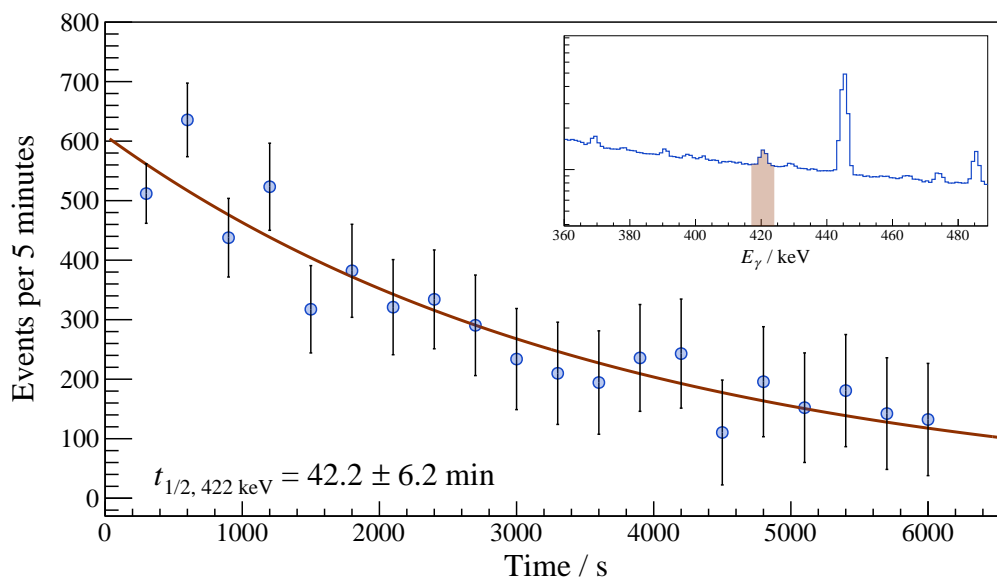


Figure 4.14: Time evolution of the 421.55 keV peak for the 9 MeV proton activation of ruthenium.

4.1.3 Sample characterization

The samples for the ruthenium activations were produced at the target laboratory at GSI Helmholtzzentrum für Schwerionenforschung GmbH by sputtering naturally composed ruthenium on aluminum plates. Figure 4.15 shows one of the four samples. The aluminum backing plates had a thickness of 1 mm. In aluminum, the

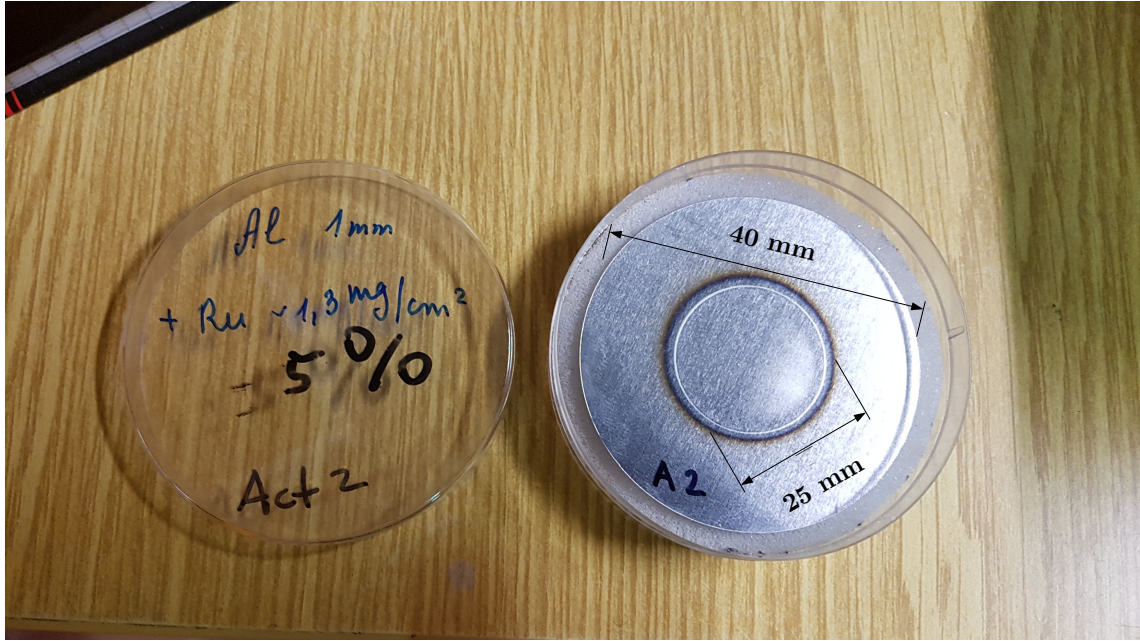


Figure 4.15: Picture of a ruthenium sample used for the activation with protons.

Act.	E_p / MeV	$\frac{m}{A}$ / mg cm^{-2}	M / u ^[28]	Iso. fraction ^[20]	μ_{areal} / 10^{17} cm^{-2}
	3.2	1.30(7)	101.07(2)	0.055 420(1)	4.3(2)
	9	1.30(7)	101.07(2)	0.055 420(1)	4.3(2)
	10	1.30(7)	101.07(2)	0.055 420(1)	4.3(2)
	11	1.20(6)	101.07(2)	0.055 420(1)	3.9(2)

Table 4.3: Characteristics of the samples used for proton induced activation of ruthenium.

projected range of protons with an incident energy of 11 MeV is 735.35 μm (calculated with SRIM [92]). Therefore, the protons are stopped inside the aluminum backing plate. Aluminum was chosen not only because of its high heat conduction coefficient, but also because induced proton capture reactions do only produce stable and short-lived nuclei compared to the decays of interest. There is no significant background produced by reactions in the aluminum backing. The area mass densities of the ruthenium layers were determined by the target laboratory of GSI with an estimated uncertainty of 5%. Areal particle densities of ^{96}Ru and the input parameters used for their calculations together with the corresponding uncertainties are listed in Table 4.3.

4.1.4 Beam energy

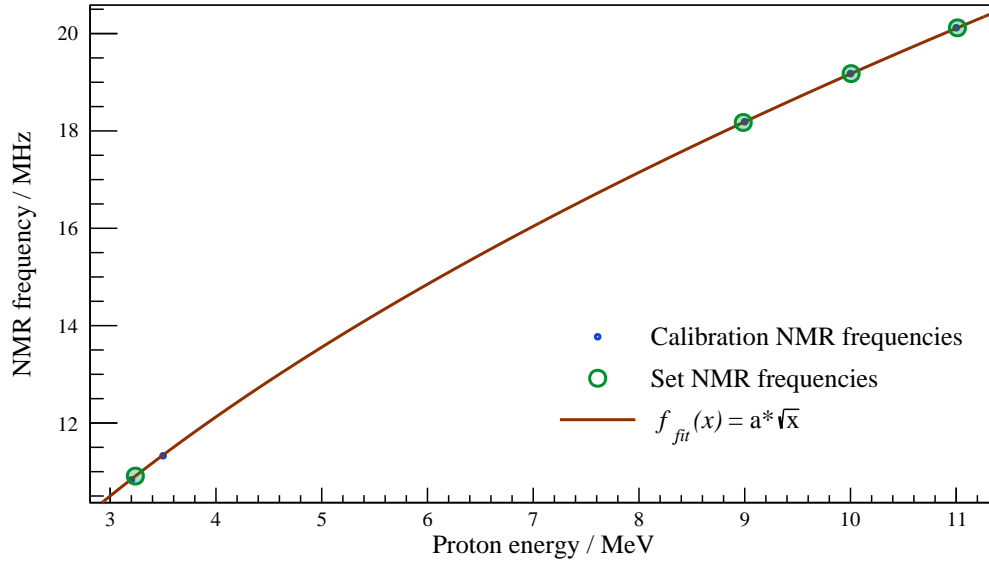


Figure 4.16: Determination of the set proton energy using NMR frequencies. The blue dots are calibration points fitted by the fit function f (red curve). The green dots indicate the NMR frequencies and the corresponding proton energies set for the different activations.

$f_{\text{NMR}} / \text{MHz}$	E_p / MeV	E_{CM} / MeV	$E_{\text{loss}} / \text{keV}$	$E_{\text{eff}} / \text{keV}$	$E_{\text{eff},CM} / \text{keV}$
10.909	3.238	3.205	63.91	3165	3.132
18.174	8.98607	8.894	33	8983	8.889
19.178	10.0063	9.904	30.5	9984	9.880
20.118	11.0113	10.899	26.3	10985	10.870

Table 4.4: NMR frequencies, their corresponding proton energies in the laboratory and the center of mass frame, and the mean energy loss of the protons inside the ruthenium layer simulated with Geant4.

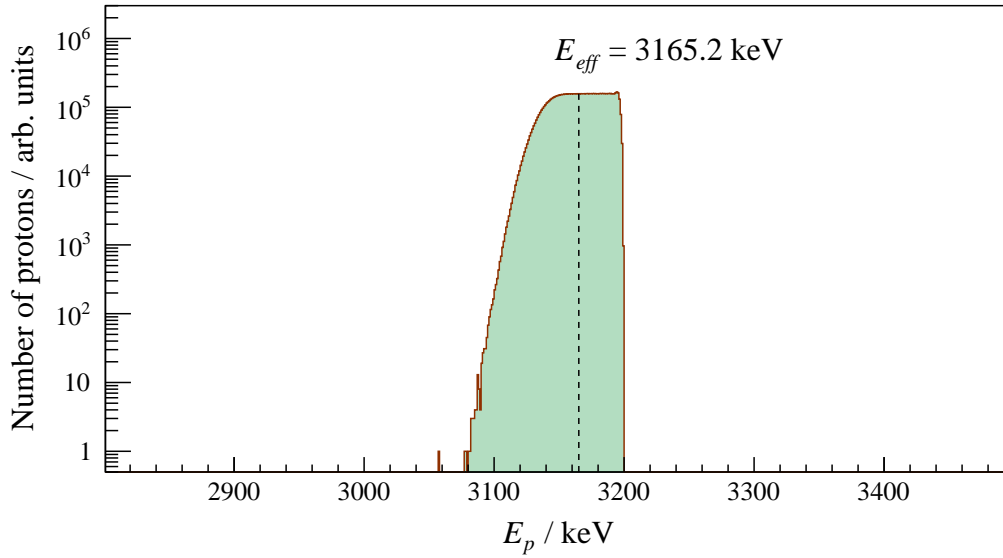


Figure 4.17: Simulated effective proton energy distribution considering energy loss in the ruthenium layer for an incident proton energy of 3.238 MeV.

4.1.5 Beam intensity

The cross section is normalized to the number of incident particles. For the activation of ruthenium, the incident particles are protons, which carry a charge of $+1e$, where e is the so-called elementary charge with a value of $1.602\,177 \times 10^{-19}$ C. The charge induced by the proton beam on the target was measured with a current integrator, which generates a pulse for every 1×10^{-8} C collected. For time dependent correction during the irradiation the number of protons are determined for time intervals of one second (see equation 4.1), where $I_{\Delta t}$ is the integrated current and $n_{pulse,\Delta t}$ the number of pulses recorded during a time interval Δt . Figure 4.18 shows the time dependent current for the four irradiations.

$$N_{p,\Delta t} = \frac{I_{\Delta t} \cdot \Delta t}{e} = \frac{n_{pulse,\Delta t} \cdot 1 \times 10^8 \text{ C} \cdot \Delta t}{e} \quad (4.1)$$

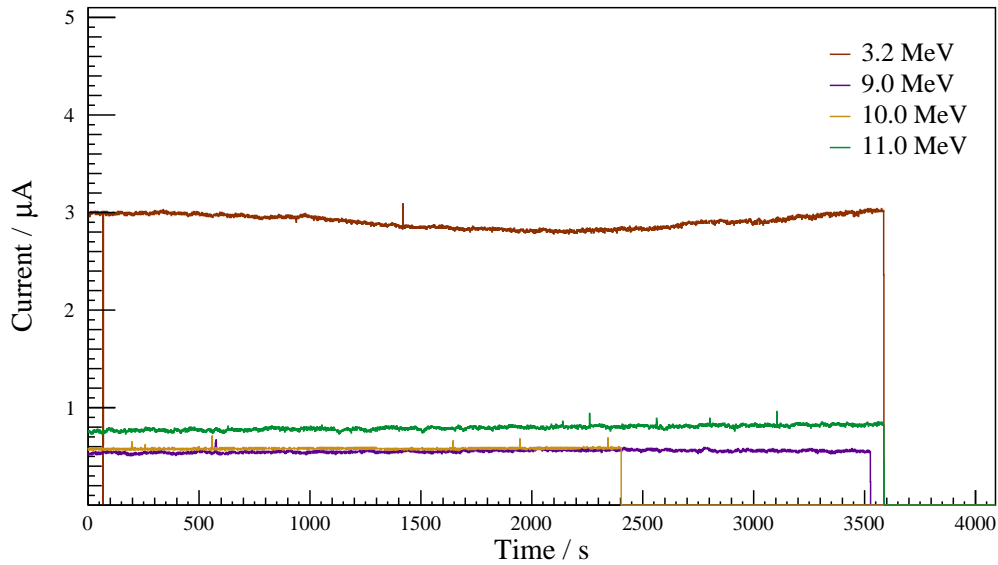


Figure 4.18: Time dependent current induced by protons on the target measured with a current integrator (one pulse corresponds to 10^{-8} C).

4.1.6 Detection efficiency

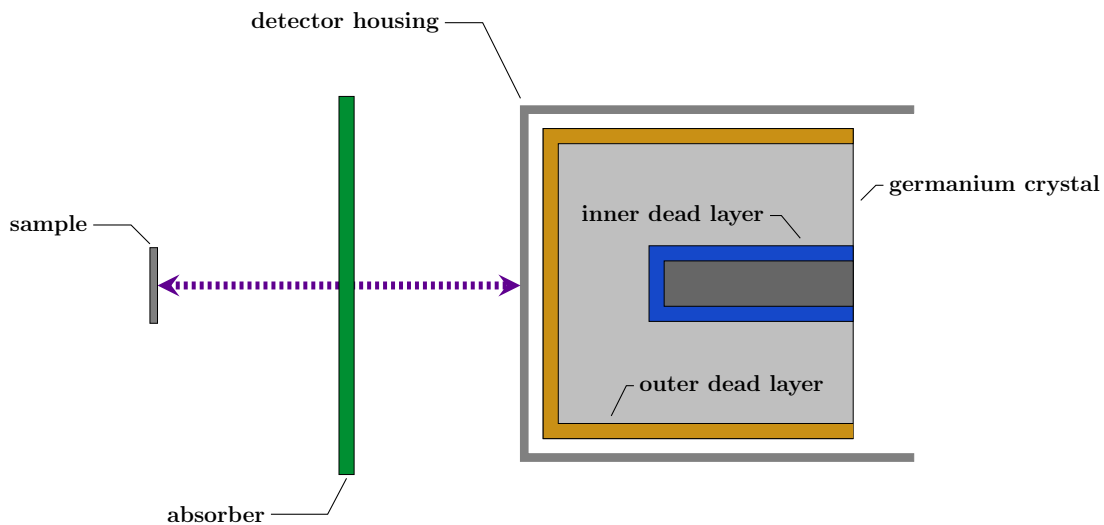


Figure 4.19: Visualization of the different geometry parameters in the efficiency simulations.

The detection efficiency is a crucial parameter for the cross section calculation. In the present thesis, Monte-Carlo-based simulations with *GEANT4* [2] were built to determine the efficiency. The efficiency is sensitive to the geometry and the material between the sample, where the photons start their path, and the active detection volume, where they possibly deposit all their energy to contribute to a full energy peak. A schematic drawing of the geometry can be found in Figure 4.1.6. The informations about the geometries of the detector were taken from its manual. Changes in different parameters that define the geometry have a unique impact on

the energy-dependent efficiency. In Appendix D some important parameters and their influence on the single gamma full energy peak efficiency are shown. Coaxial high purity germanium HPGe detectors exist in two different types, the n-type and the p-type. As a p-type detector the detector used for the proton activation of ruthenium, the germanium crystal is dotted with impurities of one chemical group lower than germanium (group 4) such as boron or gallium (group 3). The impurities got one valence electron less than their neighbouring germanium atoms and therefore contribute one excess hole in the lattice. The hole can be treated as a carrier of positive charge. In a p-type HPGe detector, the holes make the majority of charge carriers and the p in p-type stands for *positive*.

Coaxial HPGe detector do have two different electrodes, a p⁺ contact to which the produced holes drift and a n⁺ contact to which the produced electrons drift. The n⁺ contact typically consists of a boron layer with a thickness of $\sim 0.3 \mu\text{m}$. The p⁺ contact consists of a lithium layer with a thickness of several hundreds of μm diffused into the germanium crystal. For a p-type HPGe detector, this lithium layer covers the outside of the crystal. The germanium crystal with the diffused lithium in it does not contribute to the charge production of the crystal and has to be taken as inactive (*dead*) material for the detection efficiency simulations. The manufacturer of the HPGe detector used for the experiment gave a value for the thickness of the dead layer of about 0.5 mm at the time of delivery. However, many investigations of HPGe's detectors have shown that the dead layer thickness is not stable over time, but increases as the detector ages([47], [51], [60]).

The information of the dead layer thickness can be extracted from ratios of low and high energy peaks of calibration sources. Due to the energy dependency of absorption, low energy peaks are more sensitive to the thickness of none-active material between the detector and the radiation source than high energy peaks are. By varying the dead layer thickness in simulations and comparing the resulting peak ratios with measured results, the dead layer thickness can be estimated. For the p-type HPGe detector, the two calibration sources ^{152}Eu and ^{133}Ba were used for dead layer analysis. Figure 4.20 shows the results of the peak ratio $C_{122\text{keV}}/C_{344\text{keV}}$ for ^{152}Eu and $C_{81\text{keV}}/C_{356\text{keV}}$ for ^{133}Ba and the corresponding obtained dead layer thicknesses. The weighted mean value of the two results was used as the dead layer thickness for all simulations.

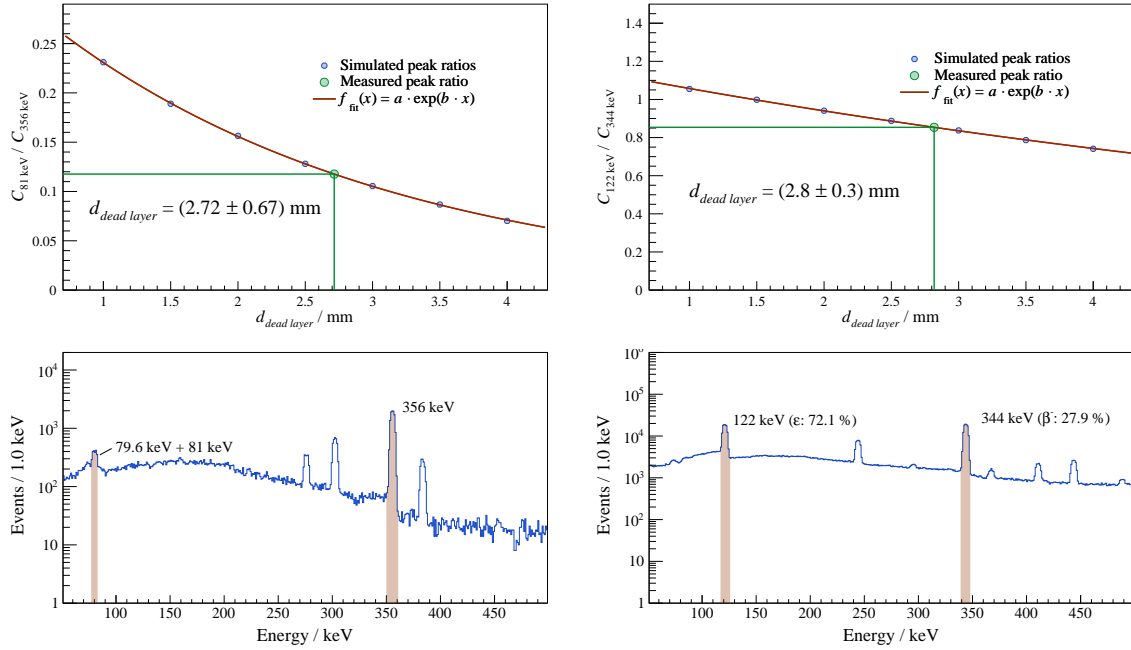


Figure 4.20: Dead layer analysis of the HPGe detector used for the gamma spectroscopy for the proton activation of ruthenium. The upper graphs show the simulated and fitted peak ratios in the two calibration sources ^{133}Ba (left) and ^{152}Eu (right). In the lower graphs the corresponding measured spectra with the peaks marked that were used for the analysis are shown.

In a last step, simulated calibration sources were fitted to experimental results by varying the distance between the sample and the detector. This was achieved by applying a least χ^2 fit. Figure 4.21 shows the corresponding plots and the results for the two different detection positions at 2 cm and 20 cm. The full energy peak efficiencies for the two setups together with the measured calibration source efficiencies are shown in Figure 4.22. Finally, the simulation correction factors f_{sim} determined with the simulations of the decays of $^{97g,m}\text{Rh}$ and ^{97}Ru are listed in Table 4.1.6.

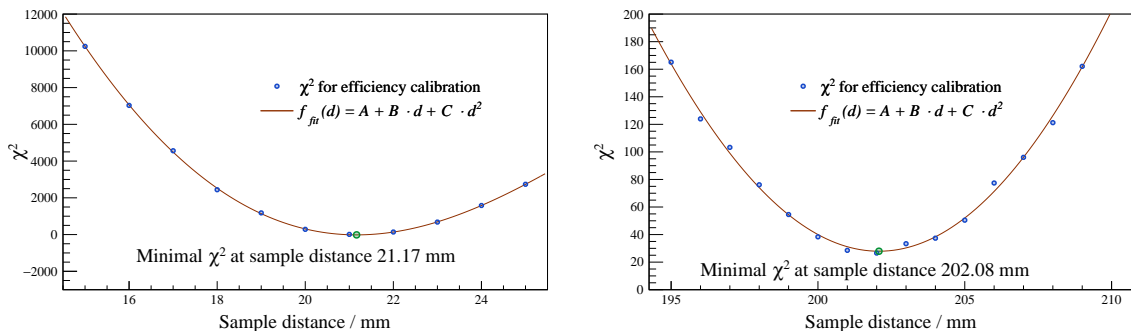


Figure 4.21: Determination of the distances used for the final efficiency simulations for a distance between the sample and the detector end cap of 2 cm (left) and 20 cm (right).

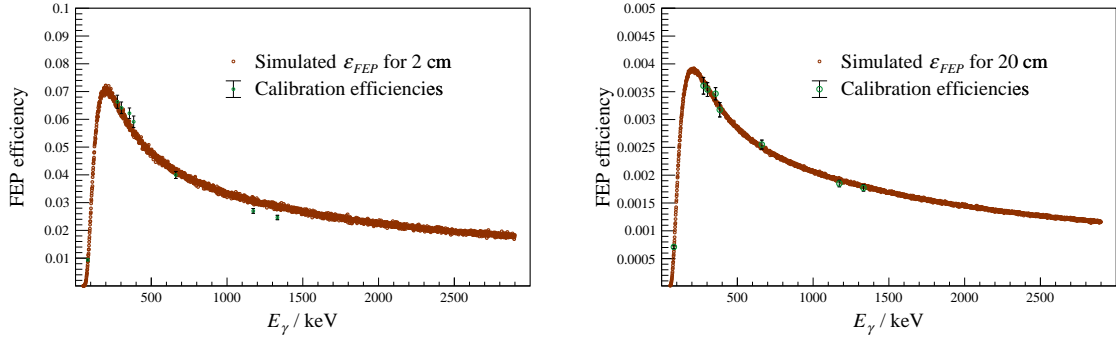


Figure 4.22: Single gamma full energy peak efficiency for the two different setups with a sample distance of 2 cm with a 2 mm copper plate absorber at 1 cm (left) and a sample distance of 20 cm with a 2 mm copper plate at 16 cm. Measured efficiencies of the calibration sources ^{133}Ba , ^{137}Cs and ^{60}Co peaks are drawn as markers.

Isotope	Energy	f_{sim}	$\Delta f_{sim}/f_{sim}$
2 cm			
^{97}Rh :	189.21 keV	0.0011565	0.3041
	421.55 keV	0.0361284	0.05
	840.13 keV	0.0038987	0.0768
	878.80 keV	0.0029578	0.0747
^{97m}Rh :	189.21 keV	0.0288032	0.05
	421.55 keV	0.0055894	0.143
	1586.66 keV	0.0017053	0.0768
	2245.6 keV	0.0027742	0.05
^{97}Ru :	215.70 keV	0.0598782	0.05
20 cm			
^{97}Rh :	189.21 keV	0.0000745	0.3041
	421.55 keV	0.0022942	0.05
^{97m}Rh :	189.21 keV	0.0019243	0.05
	421.55 keV	0.000416	0.143

Table 4.5: Simulation correction factors for all peaks used for the ruthenium activation cross section calculations.

4.1.7 Direct measurement of the $^{97g,m}\text{Rh}$ decay

For the activation at a proton energy of 3.2 MeV peaks coming from ground and from isomeric state uniquely could be used for the analysis. These peaks at gamma energies of 840.13 keV, 878.8 keV, 1586.66 keV and 2245.6 keV were not accessible for the activations at 9, 10 and 11 MeV. The only peak that was used for the analyses at these proton energies was the 421.55 keV peak with contributions from ground state and isomeric state decay.

To extract the production yields into the isomeric and the ground state of ^{97}Rh , two different methods were applied. Both methods are described in Chapter 2.2. For the analysis of the evolution of the peak over time, the counting time was splitted into intervals of equal lengths. In Table 4.6 the characteristic time periods for all activations are listed together with dead time correction factors f_{DT} and the used counting setups described in the previous chapter. For the analyses of the peak evolution over time a dead time correction was applied for each time interval individually.

In Figures 4.23, 4.24, 4.25 and 4.26 the results of the FX analyses of the 421.55 keV peak are shown for all proton energies. The received values for the production yields Y_g and Y_m allow to calculate the cross sections with the following equation:

$$\sigma_i = \frac{Y_i \cdot t_b}{I_T \cdot \mu_{areal}}. \quad (4.2)$$

In Equation 4.2, t_b is the activation time, I_T the integrated number of protons and μ_{areal} the areal particle density. This equation together with the FX formalism for the determination of the yields is only true for a constant proton current. To justify the assumption of a sufficiently constant current the f_b correction factors for all activations were determined iteratively and compared to the f_b factors for a constant flux. The deviation between these factors is lower than 0.1% for all measurements and therefore the assumption of a constant proton current is reasonably justified.

The second approach used for the determination of the cross section was the iterative approach described in Chapter 2.2. Just like for the FX approach, the 421.55 keV peak content evolution over time was used for the analysis. For the time steps a length of 1 s was chosen. The goal of the method was to determine the production yields into the ground state and the isomeric state of ^{97}Rh . This was achieved by finding a minimal χ^2 that estimates the deviation between the calculated and the measured peak contents during the different counting intervals (Eq. 2.21). The same time periods as for the FX approach were chosen (see Tab. 4.6). Results of the analyses for proton energies of 3.2 MeV and 9 MeV are shown in Figure 4.27. The MC method was used to estimate the propagation of uncertainties into the resulting values for the cross sections.

Activation energy $E_{CM,eff}$	t_b / s	t_w / s	t_m / s	$t_{interval} / s$	f_{DT}	Setup
3.132 MeV	3588	1080	3600	900	0.994	2 cm
8.889 MeV	3540	1260	3600	900	0.944	20 cm
9.880 MeV	2412	1260	3600	900	0.941	20 cm
10.870 MeV	3600	2100	3600	1800	0.90	20 cm

Table 4.6: Characteristic time periods together with dead time correction factors f_{DT} of the full counting periods and the distance between sample and detector during the counting period.

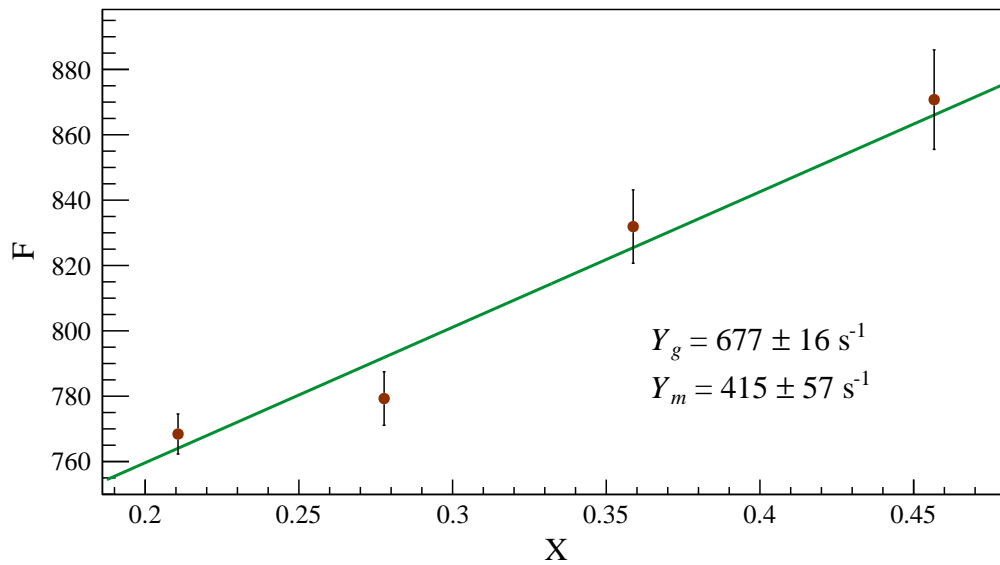


Figure 4.23: FX plot for a proton energy of 3.2 MeV. The respective peak at 421.55 keV has contributions from ground and isomeric state decays of ^{97}Rh .

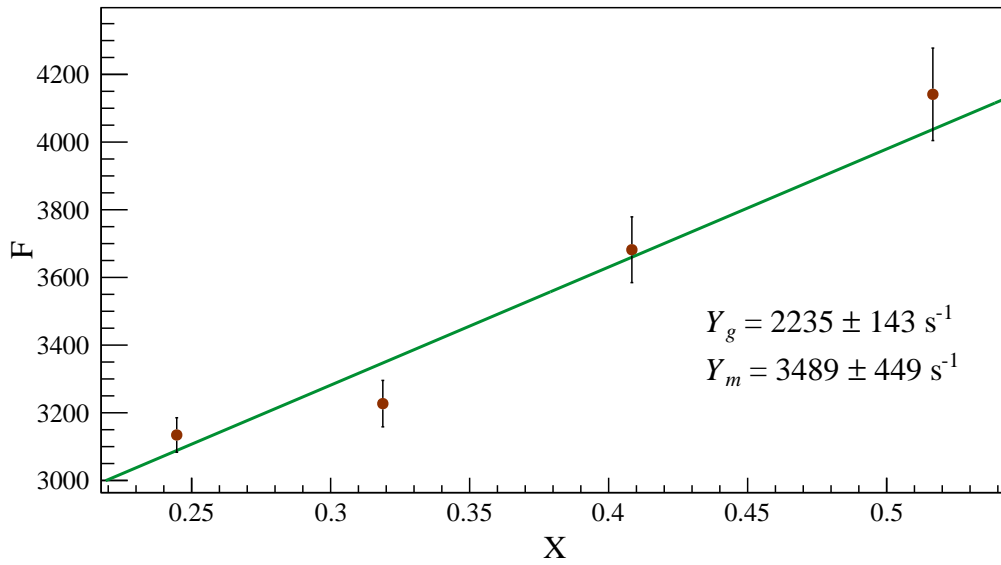


Figure 4.24: FX plot for a proton energy of 9 MeV. The respective peak at 421.55 keV has contributions from ground and isomeric state decays of ^{97}Rh .

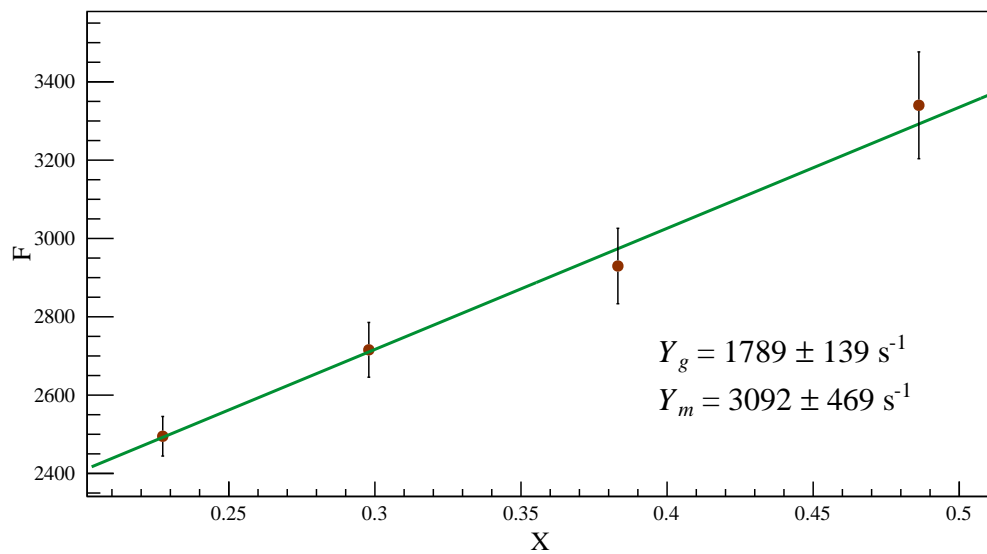


Figure 4.25: FX plot for a proton energy of 10 MeV. The respective peak at 421.55 keV has contributions from ground and isomeric state decays of ^{97}Rh .

Activation energy $E_{CM,eff}$	t_b / s	t_w / s	t_m / s	f_{DT}	Setup
8.889 MeV	3540	345960	36000	0.974	2 cm
9.880 MeV	2412	335160	17999	0.973	2 cm
10.870 MeV	3600	433740	36002	0.954	2 cm

Table 4.7: Characteristic time periods for the analysis of the ^{97}Ru decay together with dead time correction factors f_{DT} and the distance between sample and detector during the counting period.

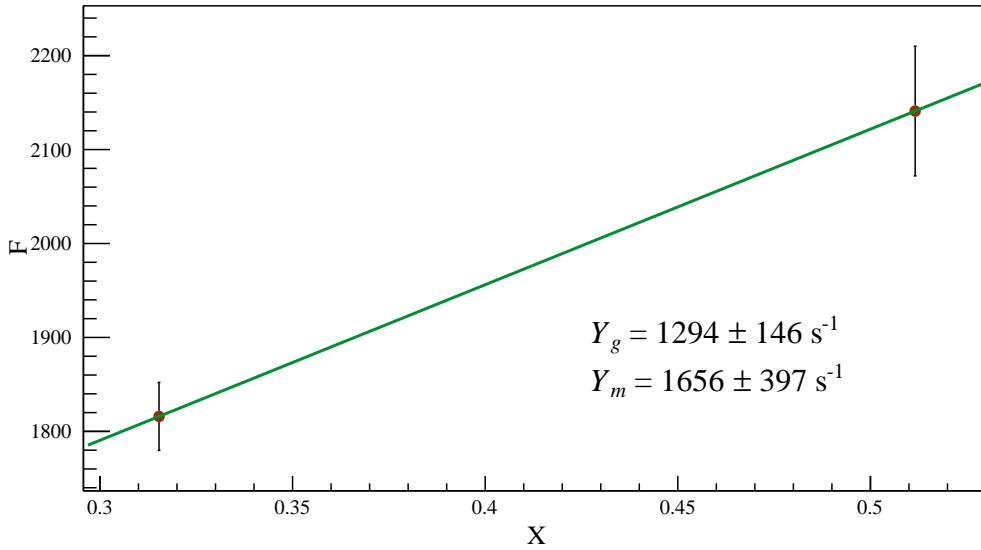


Figure 4.26: FX plot for a proton energy of 11 MeV. The respective peak at 421.55 keV has contributions from ground and isomeric state decays of ^{97}Rh .

4.1.8 Measurement of the daughter nucleus ^{97}Ru decay

Another access to the production cross section of the reaction $^{96}\text{Ru}(p,\gamma)^{97}\text{Rh}$ offers the decay of the daughter nucleus ^{97}Ru . There are three possible production paths that lead to ^{97}Ru (see Fig. 4.1). The analytical solutions for the production and decay of ^{97}Ru during the irradiation of ^{96}Ru with protons are described in Chapter 2.2 and Appendix C. In Figure 4.28, the evolution of ^{97g}Rh , ^{97m}Rh and ^{97}Ru over time is plotted during and after the irradiation phase. Due to the longer half-life of 2.83 days ^{97}Ru compared with ground state and isomeric decay of ^{97}Rh (30.7 mins and 46.2 mins) the number of decays of ^{97}Ru during the counting phases has a low sensitivity on the production ratio Y_m/Y_{tot} . However, for the calculation of the cross sections via ^{97}Ru decay the production ratios determined with the FX approach described in the previous chapter was used.

Because the same irradiated samples were used for the direct measurements, the durations of the activations as well as the number of incident protons were the same for the ^{97}Ru decay analysis. The durations of the waiting and the counting phases for all activations are listed in Table 4.7.

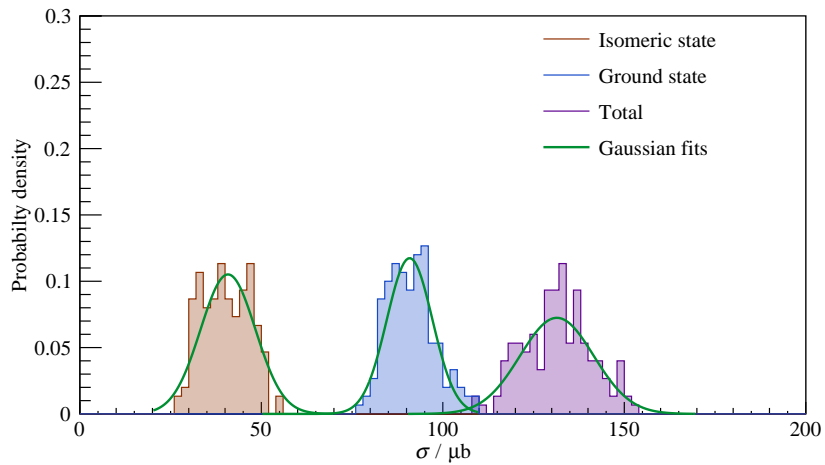
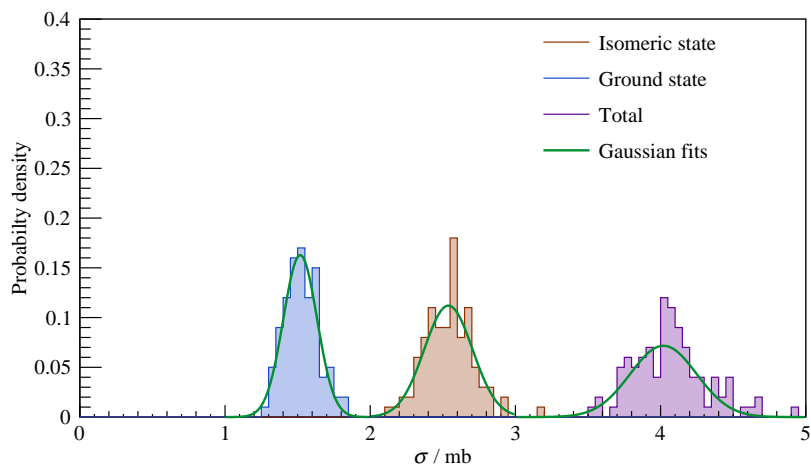
(a) $E_p = 3.2 \text{ MeV}$ (b) $E_p = 9 \text{ MeV}$

Figure 4.27: Monte Carlo simulated probability densities of the cross sections for proton energies of 3.2 MeV (top) and 9 MeV (bottom).

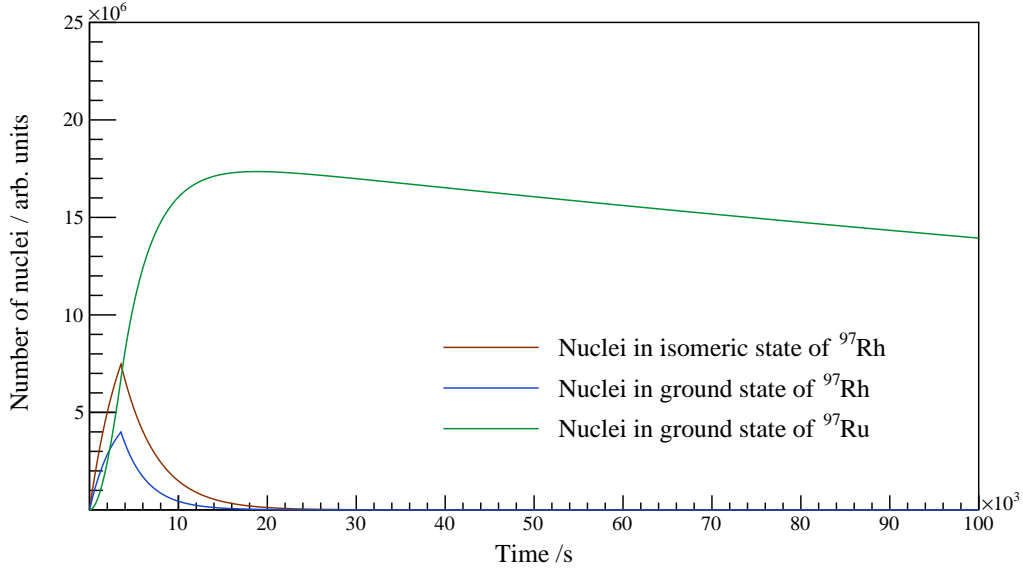


Figure 4.28: Time dependent evolution of ^{97}Rh , ^{97m}Rh and ^{97}Ru during and after the irradiation with protons at $E_p = 8.99$ MeV.

4.1.9 Estimation of uncertainties

The direct measurements of the cross sections into the ground and the isomeric state of ^{97}Rh at a proton energy of 3.2 MeV were calculated analytically. Therefore, the standard equation for the propagation of uncertainties (Eq. 2.30) was used for the determination of the uncertainties in the cross sections.

For the FX approach, the uncertainties in the production yields Y_g and Y_m were extracted from the respective fit results (see Fig. 4.23, 4.24, 4.25 and 4.26). Together with the uncertainties of the total number of protons I_T and the areal particle density μ_{areal} and again Equation 2.30, the uncertainties of the cross sections were calculated with:

$$\frac{\Delta\sigma_i}{\sigma_i} = \sqrt{\left(\frac{\Delta Y_i}{Y_i}\right)^2 + \left(\frac{\Delta I_T}{I_T}\right)^2 + \left(\frac{\Delta\mu}{\mu}\right)^2} \quad (4.3)$$

For the iterative approach, the MC method was used to estimate the uncertainties in the production yields Y_g and Y_m . Therefore, all input parameters were rolled randomly with gaussian distributions, taken their uncertainties as the width of one sigma. The obtained solutions for the probability densities of σ_g and σ_m were fitted with gaussian function and the resulting sigma widths were taken as the uncertainties of the cross sections.

Because of the lengthy equations of the time evolution of the daughter nucleus ^{97}Ru (see Chap. 2.2 and App. C) and their even more lengthy derivatives, the MC method was also used for the estimation of the uncertainties for the total cross section determined by the analysis of the ^{97}Ru decay.

4.2 Cyclic neutron activation analysis

4.2.1 Measured reactions

The following sections will give an overview of the isotopes produced during the CNA and the different decay modes that occur.

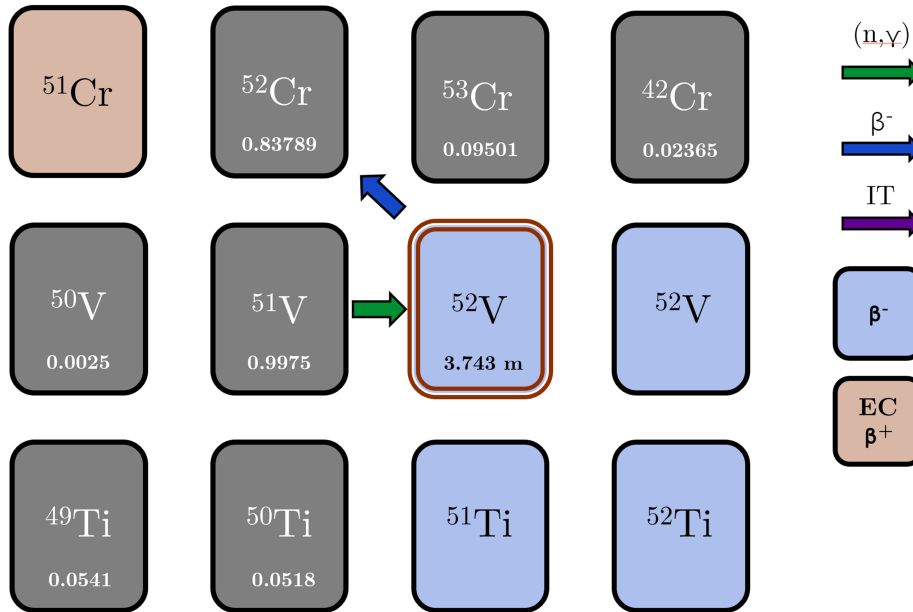
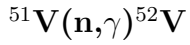


Figure 4.29: Section of the chart of nuclides around ^{51}V .

For the neutron capture cross section of $^{51}\text{V}(\text{n},\gamma)^{52}\text{V}$ the dominant γ -ray at an energy of 1434 keV ($I_g = 100\%$) of the β^- -decay ($b_{\beta^-} = 100\%$) of ^{52}V was used for the analysis. The half-life of ^{52}V is 3.743 m. In Figure 4.29 the path of the production and decay of ^{52}V is shown in a section of the chart of nuclides.

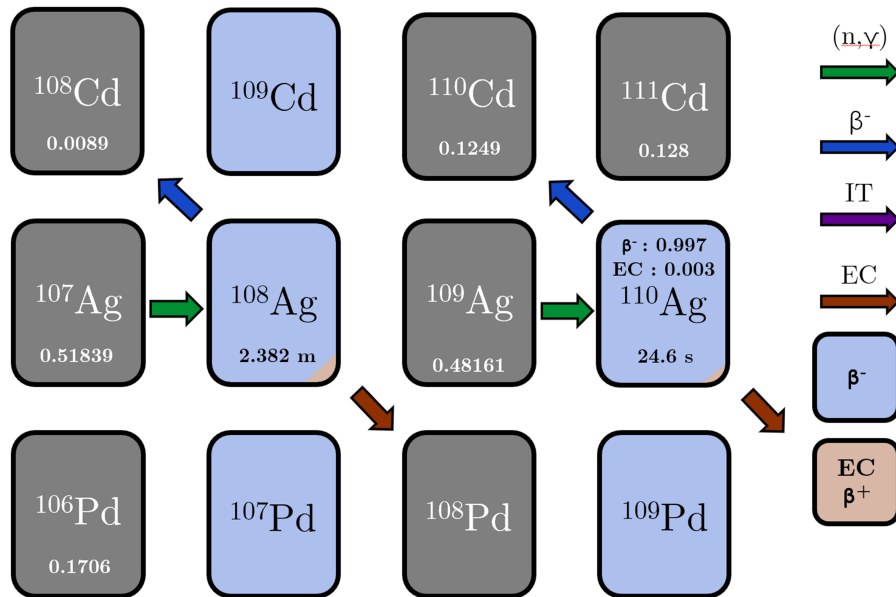
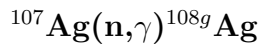
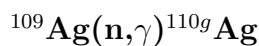


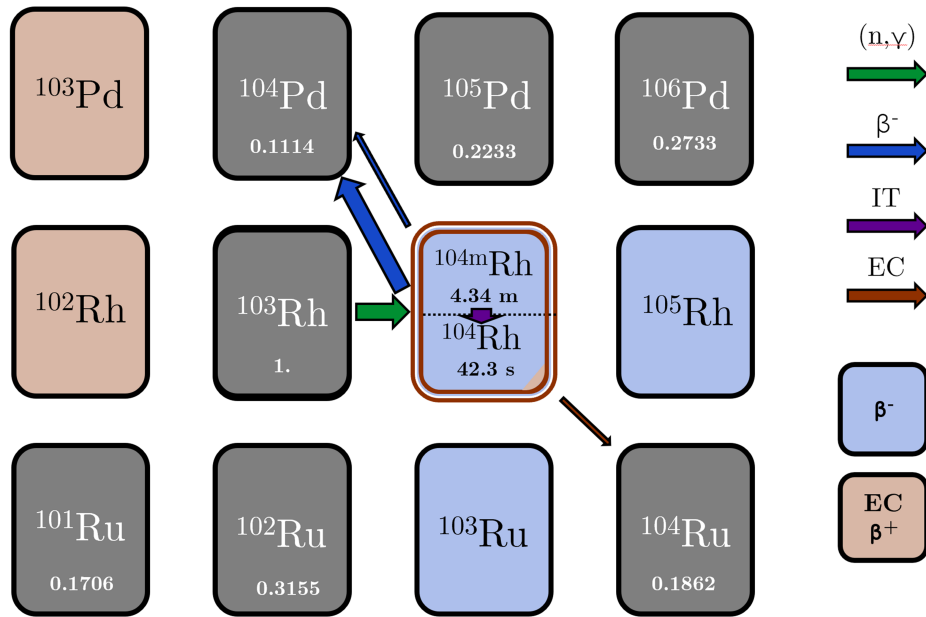
Figure 4.30: Section of the chart of nuclides around ^{107}Ag and ^{109}Ag .

The ^{108}Ag produced by neutron capture on ^{107}Ag has an isomeric state with an excitation energy of 109 keV. Because of its half-life of 438 y which is much longer than the full duration of the CNAAs measurement (≈ 140 m) the feeding through IT from isomeric to ground state and peak content contributions were negligible.

The half-life of the ground state of ^{107}Ag is 2.382 m and the γ -ray coming from β^- -decay ($b_{\beta^-} = 97.15\%$) at an energy of 632.98 keV ($I_g = 1.76\%$) was used for the analysis.



The γ -ray at an energy of 657.5 keV coming from β^- -decay of ^{110g}Ag ($b_{\beta^-} = 99.7\%$) decaying with a half-life of 24.56 s was used for the analysis of the neutron capture cross section of the reaction $^{109}\text{Ag}(n,\gamma)^{110g}\text{Ag}$. Again, the half-life of the isomeric state (249.83 d) is long enough to ignore the feeding into the ground state by IT.

$^{103}\text{Rh}(n,\gamma)^{104}\text{Rh}$

 Figure 4.31: Section of the chart of nuclides around ^{103}Rh .

With ^{103}Rh only, rhodium is a monoisotopic element. The neutron capture leads to ^{104}Rh , which has an isomeric state with an excitation energy of 129 keV and a half-life of 4.34 m and a ground state with a half-life of 42 s. Both, the isomeric and the ground state of ^{104}Rh can be populated through the deexcitation of the nuclei produced through neutron capture. There are two possible decay channels of the isomeric state, internal transition IT with a probability of 99.87% and β^- -decay with a probability of 0.13%, which is too low for a meaningful analysis with the present setup. The IT of ^{104m}Rh produces gamma radiation at energies of 51, 78, and 97 keV. Due to the low detection efficiency at low energies, these gamma rays were not accessible with the CNA setup (see Chapter 4.2.3).

The ground state of ^{104}Rh decays through a β^- -decay with a probability of 99.55% and electron capture decay with a probability of 0.45%. For the analysis, the most dominant peak of the β^- -decay at an energy of 555.8 keV ($I_g = 2\%$) was used. Because of the delayed feeding of the ground state by the isomeric state, both decays has to be considered for the analysis.

4.2.2 Gamma spectra and peak content

The gamma spectra for the peak content analysis were extracted from the measured spectra by applying a time cut. To determine the counting windows, a threshold in the detector rate signal was set. This was possible, because the event rate in the clover detector was always orders of magnitudes higher during the irradiation phases than during the counting phases. The rising flank in the detector rate that was induced by the the high radiation during the activation phase was used as a starting signal for the cycles. The counting windows were defined by adding a constant offset to these starting times. This constant offset is the sum of the irradiation time t_b and the waiting time t_w . The irradiation time itself was controlled by the TCS. The

waiting time consists of the travel time of the rail system from the activation to the counting site plus a short safety time interval. Due to significant vibrations induced in the sample holder by the rail system, this safety time ensured that the samples are in the counting position without moving. The time structure of the cyclic activations by means of the rate in the clover detector together with the characteristic times is shown in Figure 4.32.

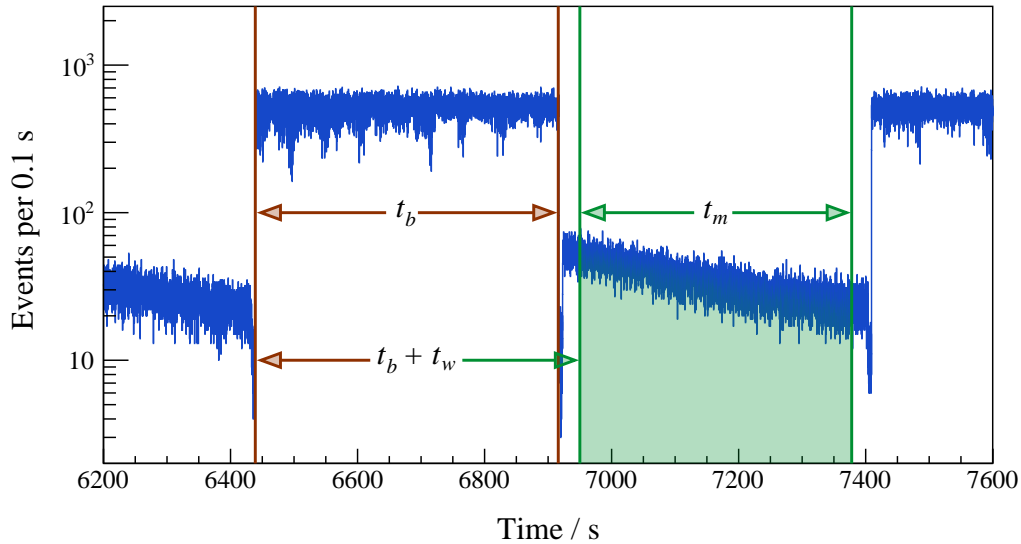


Figure 4.32: Detector rate in the clover detector during an activation. The characteristic time intervals used for the analyses are shown.

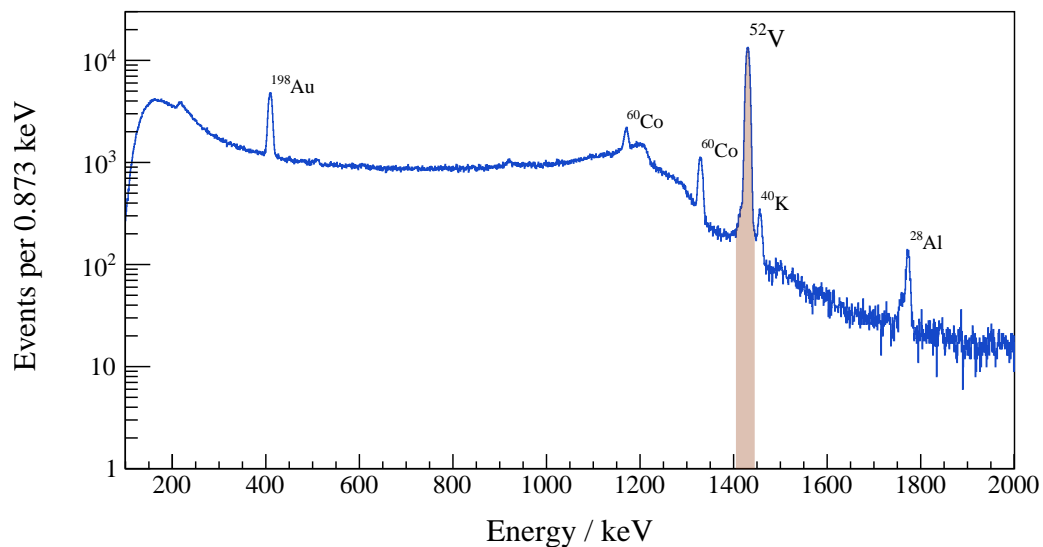


Figure 4.33: Accumulated clover detector energy spectrum of $^{51}\text{V}(n,\gamma)$. The 1434.06 keV gamma line of ^{52}V β^- - decay used for the analysis is marked.

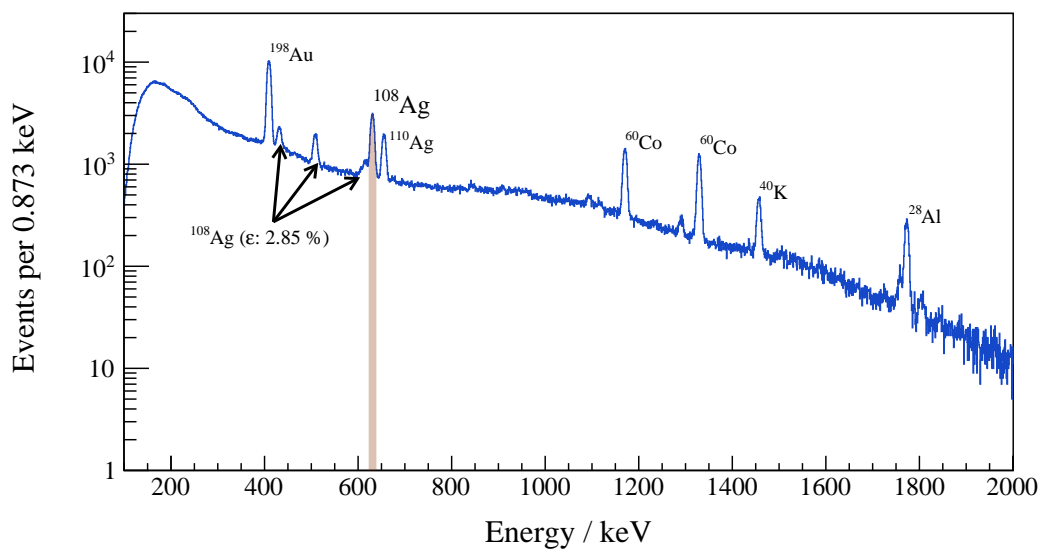


Figure 4.34: Accumulated clover detector energy spectrum of $^{107}\text{Ag}(n,\gamma)$. The 632.98 keV gamma line of ^{108}Ag β^- - decay used for the analysis is marked.

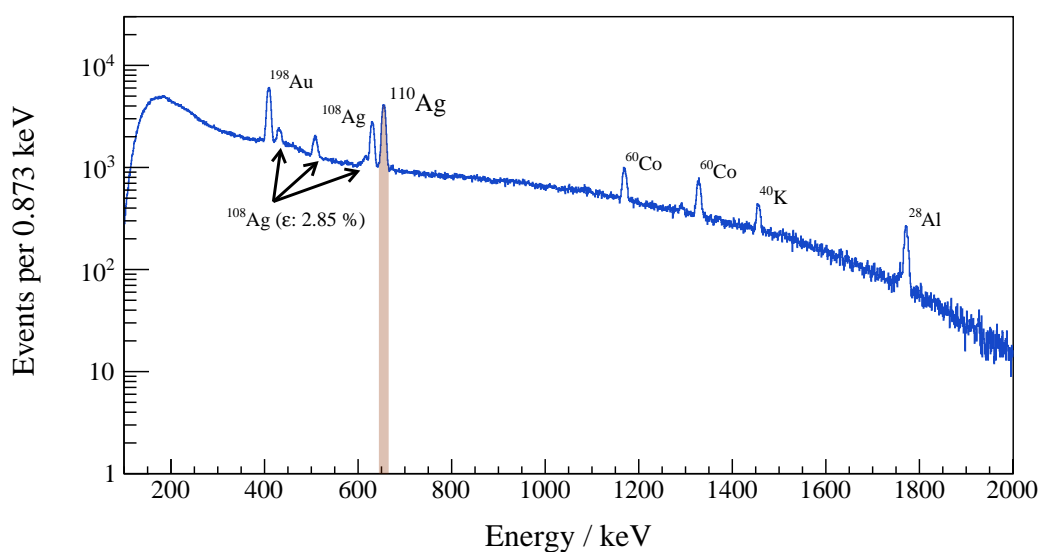
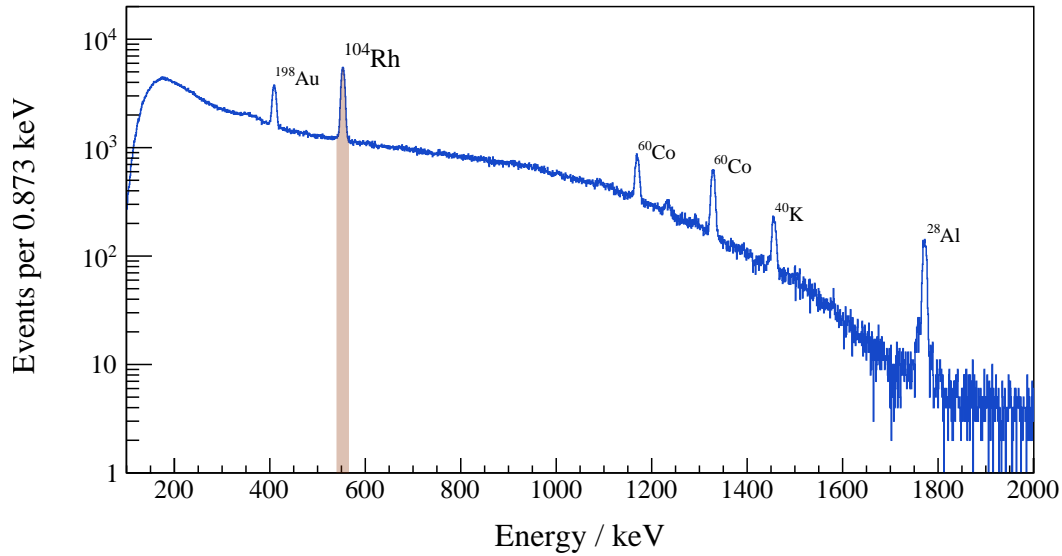


Figure 4.35: Accumulated clover detector energy spectrum of $^{109}\text{Ag}(n,\gamma)$. The 657.5 keV gamma line of ^{110}Ag β^- - decay used for the analysis is marked.

Reaction	t_b / s	t_w / s	t_m / s	t_c / s	Number of cycles
$^{51}\text{V}(n,\gamma)^{52}\text{V}$	478	8	475	970.2	13
$^{107}\text{Ag}(n,\gamma)^{108}\text{Ag}$	298	8	296	610.196	28
$^{109}\text{Ag}(n,\gamma)^{110}\text{Ag}$	48	11	46	110.192	105
$^{103}\text{Rh}(n,\gamma)^{103g,m}\text{Rh}$	98	8	96	210.195	39

Table 4.8: Overview of the cyclic neutron activation measurements.


 Figure 4.36: Accumulated clover detector energy spectrum of $^{103}\text{Rh}(n,\gamma)$. The 555.81 keV gamma line of ^{104}Rh ground state β^- - decay used for the analysis is marked.

4.2.3 Sample characterization

All samples for CNAAs were prepared at Institut für Angewandte Physik - Goethe Universität Frankfurt. The samples were all produced in cylindrical shapes with diameters of 2 cm to fulfill the requirements of the neutron energy distributions inside the samples (see Chapter 2.4). The masses of the samples were measured by weighing them with a precision balance. Plastic rings together with adhesive Kapton[®] foil kept the samples in a centered position inside the sample transport system during the activation measurements (see Fig. 4.37). The values used for the calculations of the related areal particle densities together with their uncertainties can be found in Table 4.9.

Sample	m / mg	M / u *	Iso. fraction *	μ_{areal} / 10^{20} cm $^{-2}$
^{103}Rh	197.9(1)	102.90549(2)	1	3.69(7)
^{51}V	544.9(1)	50.9415(1)	99.750(2)	20.4(4)
^{107}Ag	165.4(1)	107.8682(2)	0.51839(8)	1.52(3)
^{109}Ag	163.4(1)	107.8682(2)	0.48161(8)	1.42(3)

* Data retrieved from [31]

Table 4.9: Characteristics of the samples used for the cyclic neutron activations with the samples mass m , the molar mass M , the isotopic fraction and the areal particle density μ_{areal} .



Figure 4.37: Sample preparation and fixation to the transport system. On the left side the ^{51}V sample is shown. The sample is kept in a central position by a polyimide foil glued to a ring of polymere. The picture on the right shows the sample transport system with an empty ring clipped to the sample holder in front of the clover detector.

4.2.4 Integrated neutron flux

For the determination of the integrated neutron flux, gold monitors in the shape of cylindrical foils with a thickness of about $150\ \mu\text{m}$ were placed in the front and in the back of each sample (see Fig. 2.4). Gold as an established standard for neutron capture cross section measurements has the advantage of a well-known cross section for a huge range of neutron energies [27]. However, for typical astrophysical neutron energies of about 5 - 90 keV, there are still some discrepancies between different measured cross sections of ^{197}Au and more reliable data would be desirable.

The activity of the gold monitors were measured with two *Broad Energy Germanium Detectors* (BEGe). The integrated neutron flux was determined by averaging

Reaction	R_{Mon1}	R_{Mon2}	Φ_T
$^{51}\text{V}(n,\gamma)$	$9.4213 \cdot 10^{-14}$	$8.51792 \cdot 10^{-14}$	$4.551 \cdot 10^{11}$
$^{107}\text{Ag}(n,\gamma)$	$1.70913 \cdot 10^{-13}$	$1.62734 \cdot 10^{-13}$	$8.464 \cdot 10^{11}$
$^{109}\text{Ag}(n,\gamma)$	$1.39209 \cdot 10^{-13}$	$1.37132 \cdot 10^{-13}$	$7.010 \cdot 10^{11}$
$^{103}\text{Rh}(n,\gamma)$	$8.45839 \cdot 10^{-14}$	$8.85893 \cdot 10^{-14}$	$4.526 \cdot 10^{11}$

Table 4.10: Induced activity of the gold monitors R_1 (upstream) and R_2 (downstream) and the related integrated neutron fluxes Φ_T for all cyclic activations.

the integrated neutron flux of the upstream (index 1) and the downstream (index 2) monitor arithmetically:

$$\Phi_T = \frac{1}{2} \cdot \left(\frac{C_1}{\mu_1 \sigma_1 \epsilon_{411 \text{ keV}} f_b f_w f_m I_{411 \text{ keV}}} + \frac{C_2}{\mu_2 \sigma_2 \epsilon_{411 \text{ keV}} f_b f_w f_m I_{411 \text{ keV}}} \right) \quad (4.4)$$

The f_b factor is taking into account the time variable neutron flux and is calculated with:

$$f_b = \frac{\sum_{i=0}^T r(i) \cdot e^{-\lambda(T-i)}}{\sum_{i=0}^T r(i)}. \quad (4.5)$$

Here, T is the full time period from the start of the activation of the first cycle to the end of the activation of the last cycle, i indicates the number of a time bin and $r(i)$ the rate in the lithium glass scintillation detector of a respective time bin. The neutron distribution inside the samples and therefore the cross sections σ_i for the gold monitors depend on the relative position of the samples to the lithium layer as the origin of the produced neutrons. These cross sections for the neutron capture in gold were simulated with PINO. Using the degrees of activation of the gold monitors R_i and the radius r of the samples and monitors, Equation 4.4 can be written as follows:

$$\Phi_T = \frac{\pi r^2}{2} \cdot \left(\frac{R_1}{\sigma_1} + \frac{R_2}{\sigma_2} \right) \quad (4.6)$$

In Table 4.10 the degrees of activation of the monitors together with the integrated neutron fluxes are listed for all activations.

4.2.5 Detection efficiency

One crucial factor for the calculations of the cross section is the detection efficiency ϵ_γ (see Eq. 2.26). The strategy used for the determination of the detection efficiency is similar to the one used for the proton activation of ruthenium described in Chapter 4.1.6. The major differences resulting from the geometry and the type of the clover detector. The geometry of the clover detector used in the *Geant4* simulations

is shown in Figure 4.38.

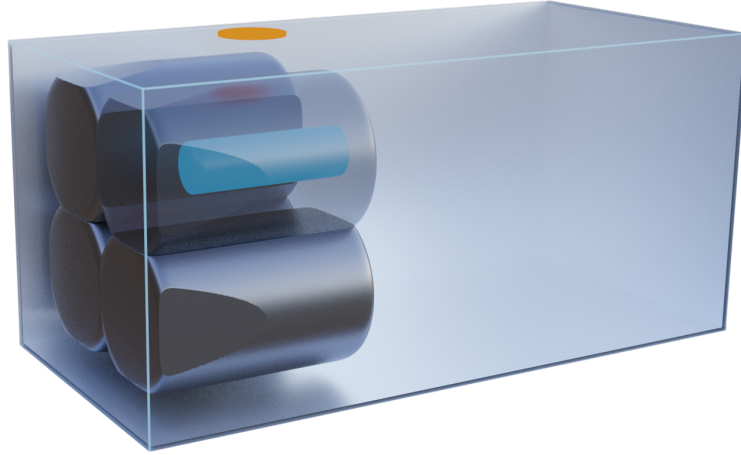


Figure 4.38: Visualization of the Clover geometry used in the detection efficiency simulations. The activated sample is shown in orange, the inner electrode of the active (transparent) crystal in blue.

For the purpose of visualization, the active germanium crystal used for the CNAAs is drawn transparent. The main difference of the clover detector as a n-type detector compared to the p-type detector used for the proton activation is that the lithium diffused electrode is placed on the inside cylindrical surface of the crystal. N-type detectors are doped with group 5 atoms, typically arsenic (As) or phosphorus (P). The impurities acting like donors and deliver one quasi-free electron and therefore, the negatively charged electrons contribute to the charge transport as a majority. The efficiency simulations were fitted to calibration source data by varying unknown geometry parameters. The inner dead layer thickness as well as the exact geometry of the inner electrode could not be determined directly. The second parameter used for the optimization was the distance between the sample and the clover detector. In Figure 4.39 the deviation between simulated and measured values for the peak contents of the calibration sources is shown by means of the χ^2 estimator. The χ^2 was calculated for pairs of samples distance and inner dead layer thicknesses by:

$$\chi^2 = \sum_{i=1}^n \frac{(C_{sim}^i - C_{meas}^i)^2}{C_{meas}^i}. \quad (4.7)$$

In Equation 4.7 the i 's indicate the different peaks of the calibration sources, the C_{sim} and C_{meas} are the simulated and measured peak contents of the respective peaks. The lower the χ^2 value for a given pair of distance and inner dead layer thickness is, the higher is the agreement between the simulated and the measured calibration data.

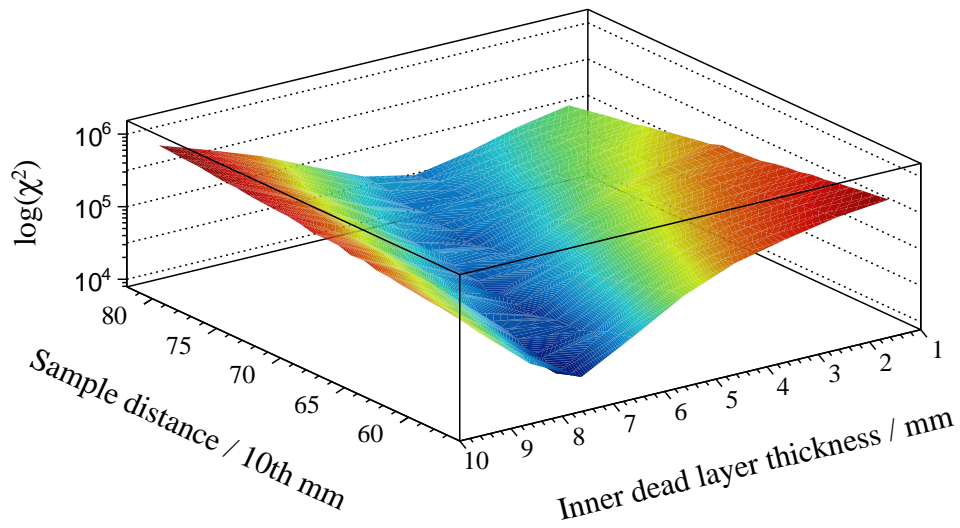


Figure 4.39: Comparison of the simulated and measured efficiencies for different pairs of values for the sample distance and the inner dead layer thickness. The χ^2 is used as an estimator for the deviation between simulated and measured peak contents of the calibration sources ^{137}Cs , ^{133}Ba , ^{54}Mn and ^{22}Na .

The peak ratio in the decay spectrum of the calibration source ^{133}Ba of the peaks at 276 keV and 467 keV shows a high sensitivity on the sample distance. The reason for this effect is that 467 keV is not a full energy peak of a single gamma, but a summing peak result from simultaneous energy deposition of x-rays together with gammas of the energies of 81 keV and 356 keV. By simulating different distances and applying a linear fit to the simulated peak ratios, the final distance was determined by entering the measured value for the peak ratio into the linear equation. The analysis is shown in Figure 4.40. The value found with this method for the distance between the sample and the detector is 6.83 mm.

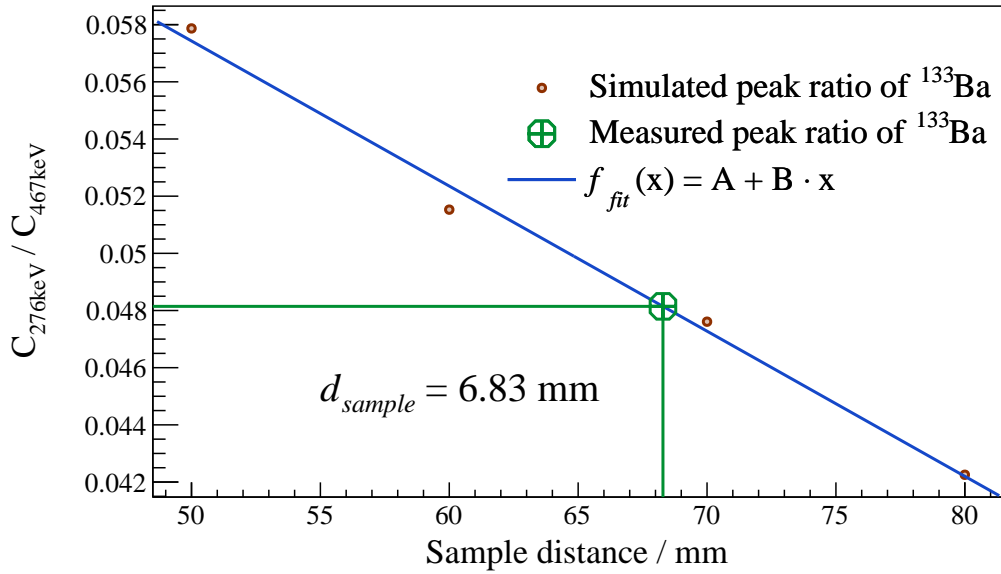


Figure 4.40: Determination of the distance between the sample and the detector for the CNA efficiency simulations.

The inner dead layer thickness was determined by fitting the thickness to the measured calibration data. The dead layer geometry was approximated by the simplified assumption of a cylindrical volume that grows upon the inner electrode into the germanium crystal. It has to be mentioned that the exact geometry of the inner electrode was unknown. Both, the inner electrode and the inner dead layer were treated as inactive material in which deposited energy does not contribute to the detector signal. The results of the analysis are shown in Figure 4.41. The minimal χ^2 value was found by fitting a third degree polynomial and finding the minimum of the curve. With this method, the radius of the cylinder of inactive material in the crystal was found to be 7.35 mm.

Finally, together with the values for the inner dead layer and the distance between the sample and the detector, the simulated full energy peak efficiency ϵ_{FEP} is shown in Figure 4.42.

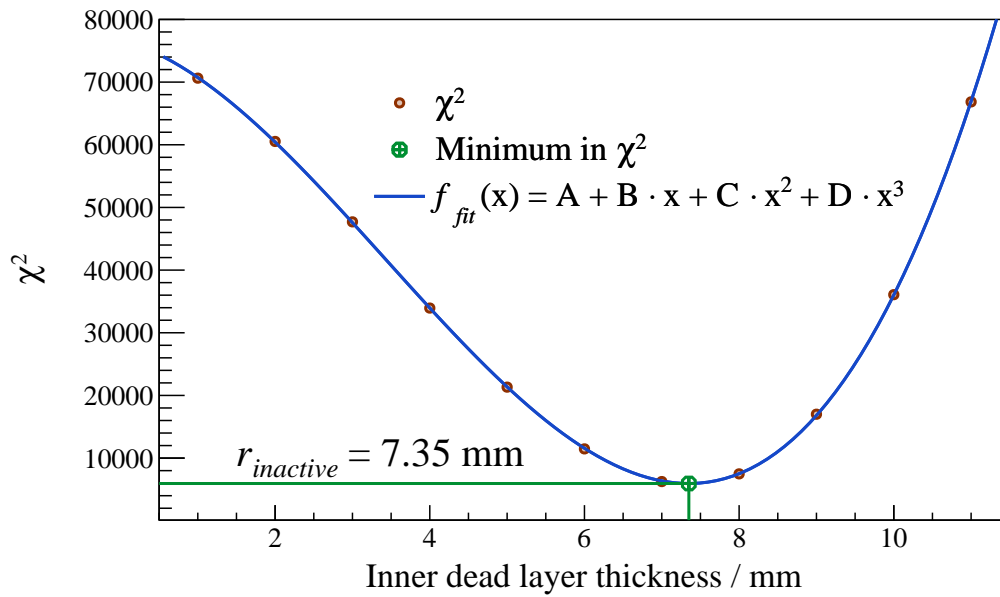


Figure 4.41: Determination of the radius of the inactive cylindrical volume by finding the minimum χ^2 value of the measured and simulated calibration peaks.

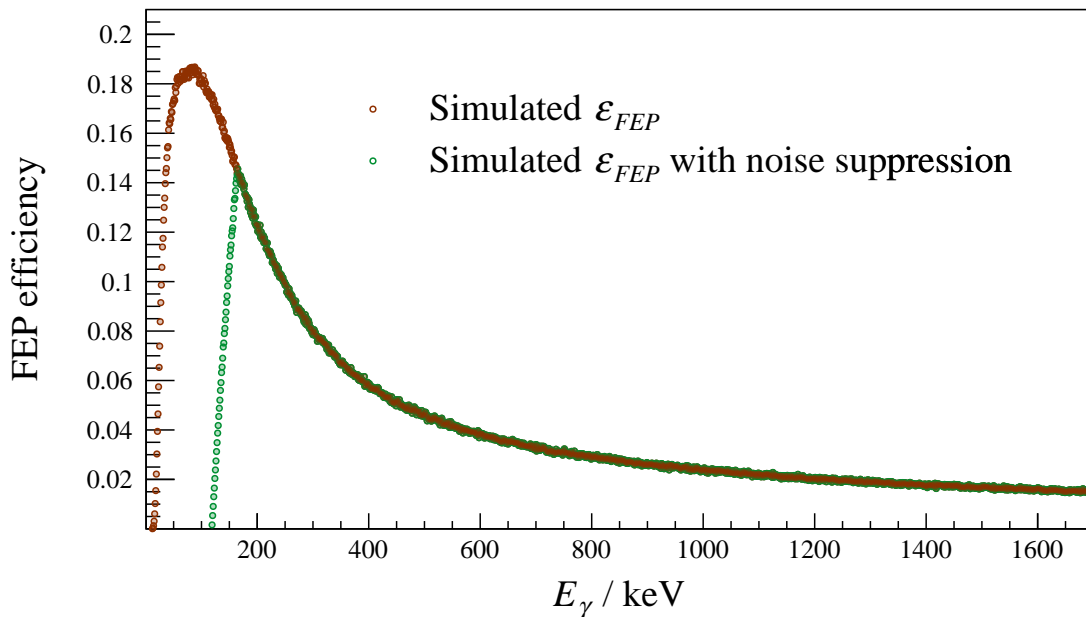


Figure 4.42: Simulated full energy peak efficiency for the CNAA. The green dots show the ϵ_{FEP} corrected for the noise suppression applied at low energies.

4.2.6 Time dependent correction factors

Equation 2.26 includes five correction factors f_i with dependencies on times and the decay constant of the measured isotopes. Assuming a sufficiently constant neutron flux by means of the half-lives of the respective nuclei, the analytical equation

$$f_b = \frac{1 - e^{-\lambda t_b}}{\lambda t_b} \quad (4.8)$$

together with the irradiation times t_b and the decay constants λ were used to calculate the f_b factors. The factors f_c that correct the number of decays during a cycle by taking into account the produced and left nuclei from previous cycles was calculated with Equation 2.27. The two factors f_w and f_m correcting the number of decays during the waiting phase and the counting phase were calculate with:

$$f_w = e^{-\lambda t_w} \quad (4.9)$$

$$f_m = 1 - e^{-\lambda t_m}. \quad (4.10)$$

The last time dependent correction factor for the cross section calculation is the dead time correction factor f_{DT} . The reason for this correction is the dead time of the detection system that occurs after an event was registrated. It is defined as the shortest time the detection system is able to record two consecutive events separately. A consequence of the dead time is that the time the detection system is able to register events (usually called *live* time) is always smaller than the *real* time of the measurement. Therefore, the number of measured events is also smaller than the real number of events that occur during the counting phase:

$$C_{meas} = C_{real} \cdot f_{DT}. \quad (4.11)$$

For the CNAA a ^{60}Co calibration source was mounted close to the clover detector during all measurements. The radiation of the source was taken as a constant rate dead time monitor. As an approximation for small dead times of the detection system, a linear dependency between the detection rate and the dead time correction factor can be assumed:

$$f_{DT}(r) = 1 - const. \cdot r. \quad (4.12)$$

The constant factor in 4.12 was determined by measuring the rate in the 1173 keV peak of ^{60}Co during the measurements of calibration sources with different constant rates. In Figure 4.43 the results of the analysis is shown. The constant factor that defines the rate dependency of the dead time correction factor was determined as $(5 \pm 0.25)^{-5}$.

During one cycle, the detection rate cannot be treated as constant. For all measurements, the rate in the detector is dominated by the radiation coming from the respective isotope of interest. Therefore, the time dependent rate in the detector follows the exponential decay with the decay constant of the measured isotope during the counting phase (see Fig. 4.32). The following iterative calculations were applied to consider this circumstance:

$$f_{DT}^c(r) = \frac{\sum_{t=0}^{t_m} (e^{-\lambda t} \cdot f_{DT}(r))}{\sum_{t=0}^{t_m} e^{\lambda t}}. \quad (4.13)$$

To calculate the final dead time correction factor f_{DT} , the dead time correction factors for each cycle f_{DT}^c were weighted by the number of counts in the respective peak of the measured decay in each cycle:

$$f_{DT} = \frac{\sum_{c=0}^n (f_{DT}^c \cdot C_{cyc})}{\sum_{c=0}^n C_{cyc}}. \quad (4.14)$$

All values for the correction factors for the different measurements together with their uncertainties are listed in Tables B.1, B.2, B.3 and B.4.

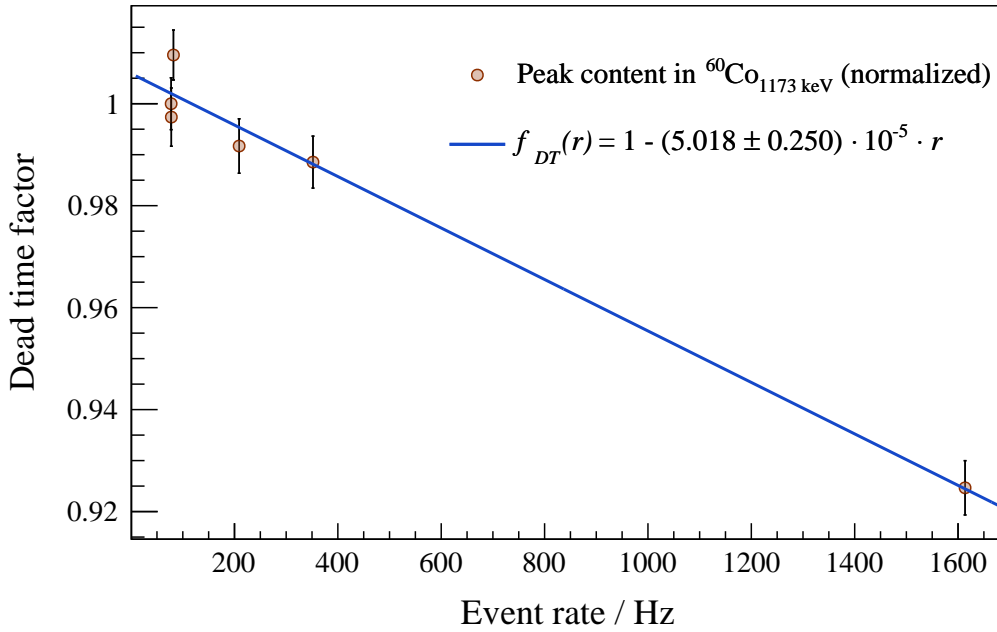


Figure 4.43: Analysis of the dead time correction for constant rates. The points are measured values of the normalized peak content in 1173 keV of the dead time monitor ^{60}Co for different event rates in the detector.

4.2.7 Iterative approach for $^{103}\text{Rh}(n,\gamma)$

As stated in Chapter 4.2.1, the feeding of the ground state in ^{104}Rh by IT of the isomeric state can not be ignored for the analysis of the neutron capture cross section into the ground state. Therefore, the iterative approach introduced in Chapter 2.2 was used to determine the evolution of the produced ^{104}Rh nuclei in the ground and the isomeric state over time. In Figure 4.44 this evolution of the number of nuclei in the ground and the isomeric state during a cyclic activation is shown for a constant production rate (constant neutron flux) and two different cross section ratios. In addition, the time dependent number of nuclei without the feeding by isomeric state decays is drawn. Figure 4.45 shows the corresponding decays per cycle for both cross section ratios. Even if only a peak coming from the ground state decay of ^{104}Rh was accessible for the analysis, there is information about the production cross section of the isomeric state in the evolution of the decays measured per cycle.

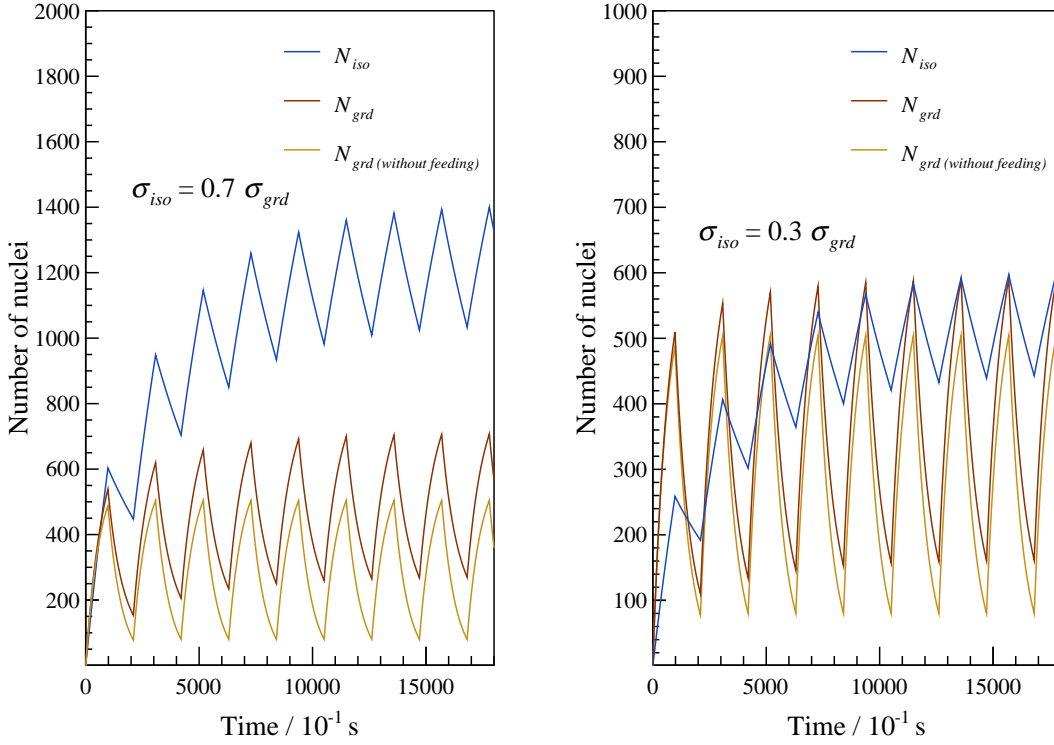


Figure 4.44: Simulated evolution of produced nuclei in isomeric and ground state for the reaction $^{103}\text{Rh}(n,\gamma)$. The number of nuclei in isomeric state (blue), ground state (red) and ground state without the feeding by the isomeric state (orange) are drawn for two different cross section ratios.

The strategy to determine the production cross sections into the ground and the isomeric state was to simulate the number of decays per cycle for pairs of ground state and isomeric state production yields and find a minimal χ^2 value. Because the uncertainties of the decays per cycle are approximately the same for each cycle, the simple form

$$\chi^2 = \sum_{i=1}^n \frac{(D_{meas}^i - D_{sim}^i)^2}{D_{meas}^i} \quad (4.15)$$

was used as an estimator. The time step size was chosen to be 0.1 s. The time dependent neutron flux was taken into account by using the detection rate of the Li-Glass detector. In Figure 4.46 the time dependent neutron flux together with the corresponding number of nuclei is shown. The results of the analysis are visualized in Figure 4.47 and 4.48. In Figure 4.47 the decays per cycle of the measurement and the simulated best fit are plotted. The two dimensional plot in 4.48 shows χ^2 values for different values of ground state and isomeric state production cross sections.

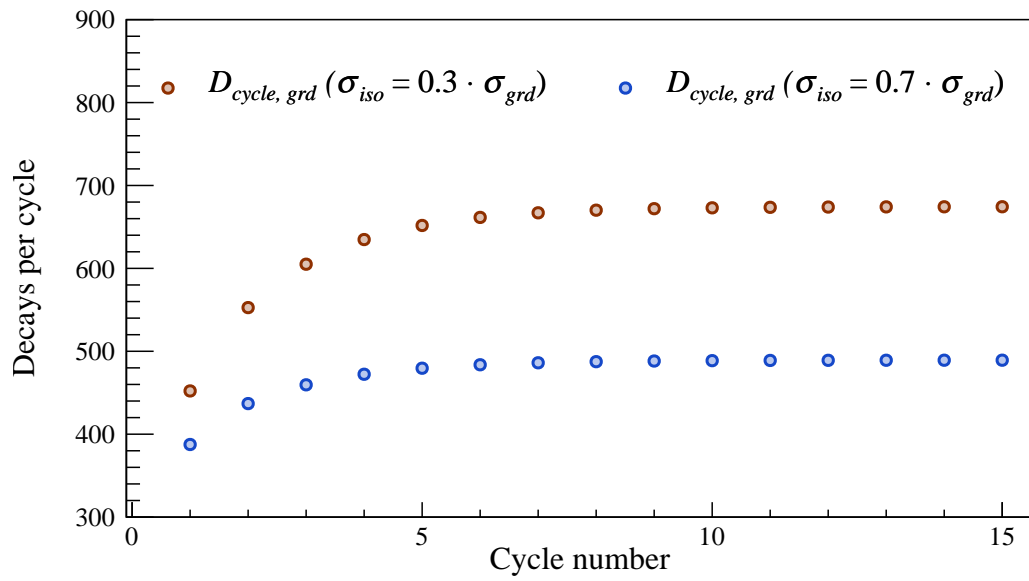
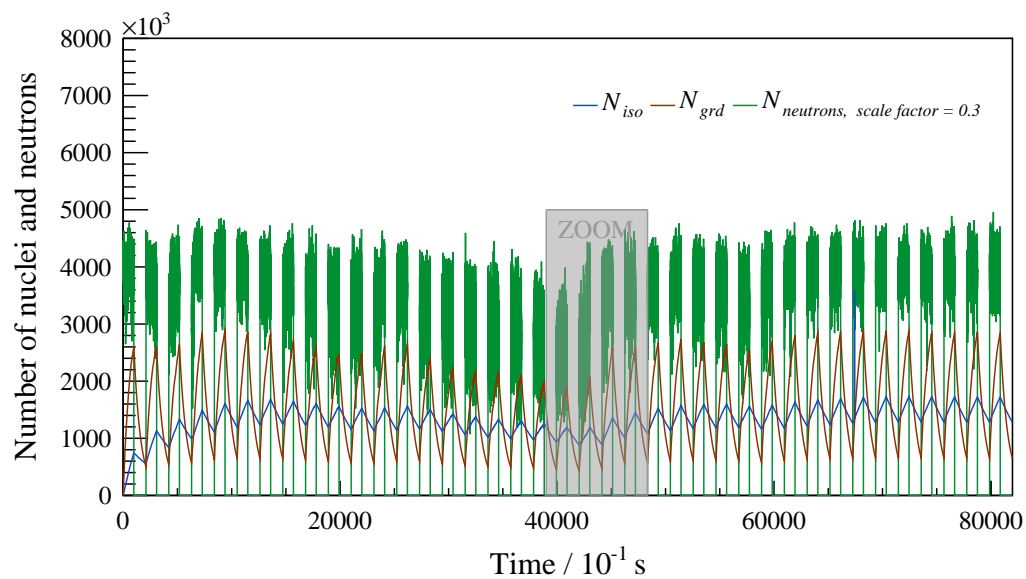
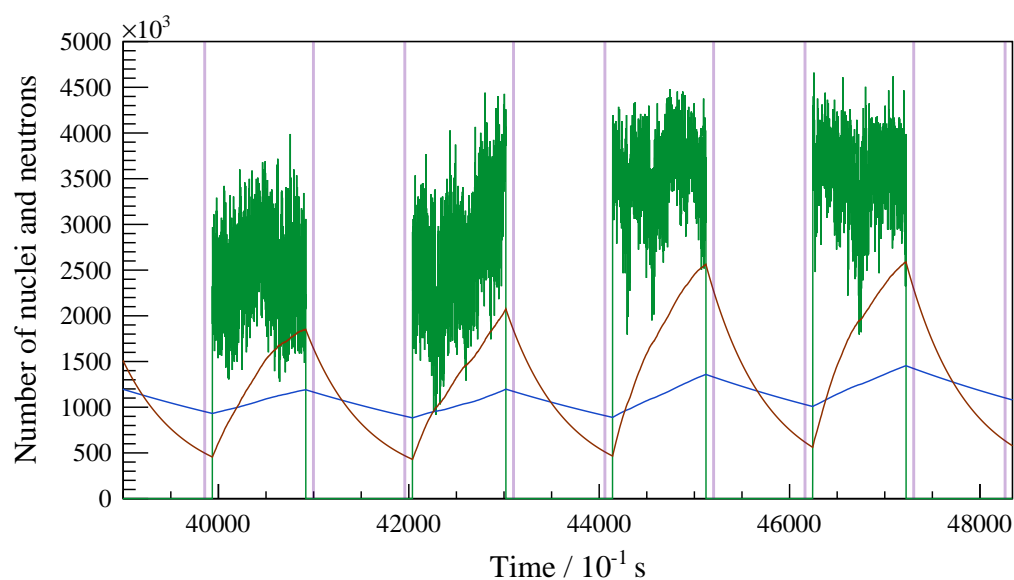


Figure 4.45: Calculated decays per cycle for two different cross section ratios.



(a)



(b)

Figure 4.46: Simulated time evolution of number of nuclei and incident neutrons for the best fit for all 39 measured cycles (a) and a zoomed in view for cycles 20 to 23 (b). The green curve shows the measured neutron flux over time scaled with a factor of 0.3. The light violet lines in (b) indicate the counting windows.

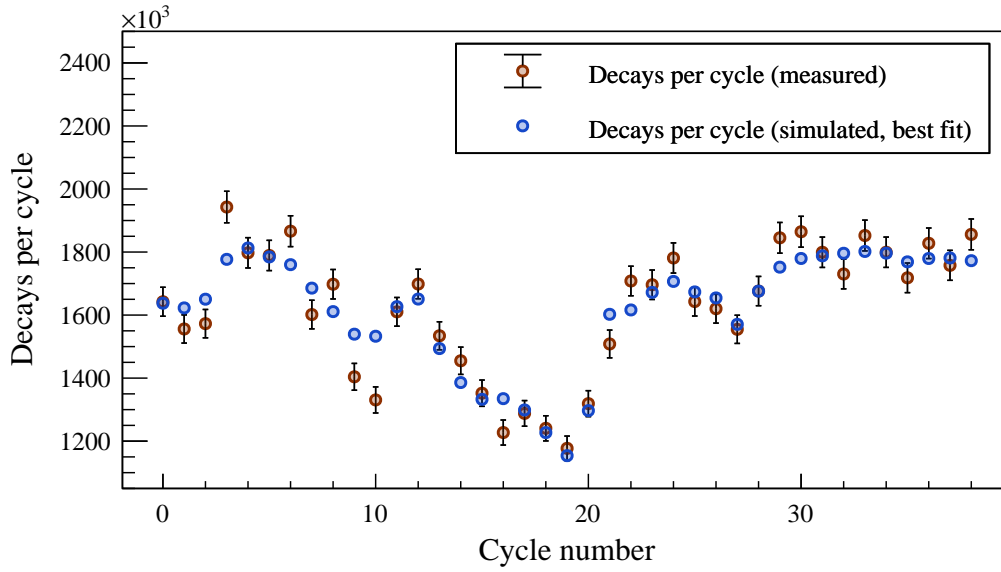


Figure 4.47: Measured (red) and simulated (blue) decays per cycle for best fit. The error bars indicate the $1\text{-}\sigma$ range resulting from the statistical uncertainties of the measured counts per cycle.

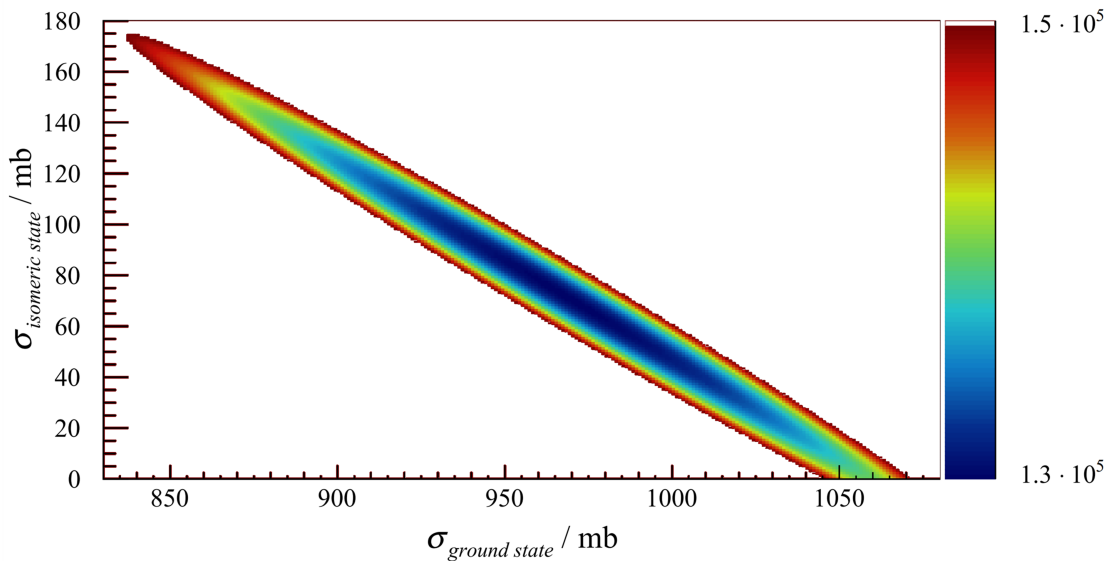


Figure 4.48: χ^2 values for pairs of σ_g and σ_m . For the sake of visualization, the maximum χ^2 value on the z-axis is set to $1.5 \cdot 10^5$.

4.2.8 Estimation of uncertainties

Uncertainties for $^{51}\text{V}(n,\gamma)$ and $^{107,109}\text{Ag}(n,\gamma)$

For the calculations of the neutron capture cross sections in vanadium and silver the formalism described in Chapter 2.3 was used. The form of Equation 2.26 as a product of factors together with the general equation for the propagation of the uncertainty

of independent variables (Equation 2.30) allows to calculate the uncertainty in the cross section as follows:

$$\frac{\Delta\sigma}{\sigma} = \sqrt{\left(\frac{\Delta\mu}{\mu}\right)^2 + \left(\frac{\Delta C_{sum}}{C_{sum}}\right)^2 + \left(\frac{\Delta\Phi_T}{\Phi_T}\right)^2 + \sum_i \left(\frac{\Delta f_i}{f_i}\right)^2}. \quad (4.16)$$

The time dependent factors f_i in Equation 4.16 are described in Chapter 2.3. Hereinafter, the estimation of the uncertainties of all variables are explained.

Cumulative peak content

The peak content was determined by integrating the peak area and subtracting the underlying background. Following poisson statistics, the standard deviation of the peak content is given by the square root of the integrated peak area. The uncertainty in the underlying background was estimated by determining the variance in the background on both sides of the respective peak. The absolute uncertainty in the cumulative peak content is given by:

$$\Delta C_{sum} = \sqrt{\Delta C_{int}^2 + \Delta B_{noise}^2}. \quad (4.17)$$

Areal particle density

For the estimation of uncertainties in the areal particle density, only the uncertainties in the measurement of the radius and the mass of the samples were taken into account:

$$\Delta\mu = \sqrt{\left(\frac{N_A\alpha}{M\pi r^2} \cdot \Delta m\right)^2 + \left(\frac{2mN_A\alpha}{M\pi r^3} \cdot \Delta r\right)^2}. \quad (4.18)$$

Integrated neutron flux

The integrated neutron flux was determined by analysing the induced activity in the gold monitors. Sources of uncertainty are the areal particle density of the gold foils, the peak content in the 411 keV peak, the cross section for the respective neutron spectrum and the detection efficiency. The relative uncertainty in the integrated neutron flux is given by:

$$\frac{\Delta\Phi_T}{\Phi_T} = \sqrt{\left(\frac{\Delta\mu_{Au}}{\mu_{Au}}\right)^2 + \left(\frac{\Delta C_{411keV}}{C_{411keV}}\right)^2 + \left(\frac{\Delta\sigma_{SACS,Au}}{\sigma_{SACS,Au}}\right)^2 + \left(\frac{\Delta\epsilon}{\epsilon}\right)^2}. \quad (4.19)$$

Waiting time correction factor

The uncertainty of the correction factor for the waiting phase f_w depends on the uncertainty of the waiting time t_w and the uncertainty of the decay constant λ of the respective isotope. Because the timing precision of the DAQ is assumed to be in the order of nano seconds, the uncertainty is dominated by the bin length which

was chosen to be 100 ms for all measurements. For the absolute uncertainty, half of the bin width was applied. The absolute uncertainty of f_w is calculated by:

$$\Delta f_w = \sqrt{(t_w \cdot e^{-\lambda t_w} \cdot \Delta\lambda)^2 + (\lambda \cdot e^{-\lambda t_w} \cdot \Delta t_w)^2}. \quad (4.20)$$

Irradiation time correction factor

The irradiation time was controlled by the TCU described in Chapter 3.2.2. Due to the precision of the system, for all measurements the uncertainty in t_b is negligible and the only source of uncertainty taken into account for the irradiation time correction factor f_b is the decay constant λ :

$$\Delta f_b = \left(\frac{e^{-\lambda t_b}}{\lambda} - \frac{1 - e^{-\lambda t_b}}{t_b \lambda^2} \right) \cdot \Delta\lambda. \quad (4.21)$$

Counting time correction factor

The counting window was set in the DAQ with a precision of nano seconds. Again, the only relevant source of uncertainty is assumed to be the decay constant λ :

$$\Delta f_m = t_m \cdot e^{-\lambda t_m} \cdot \Delta\lambda. \quad (4.22)$$

Dead time correction factor

The determination of the dead time correction factor f_{DT} was described in Chapter 4.2.4. Three sources of uncertainty occur, the dead time correction $f_{DT}(r)$ depending on the rate in the detector r , the uncertainty of the number of counts per cycle $C_{sum,cyc}$ and again the uncertainty of the decay constant λ :

$$\frac{\Delta f_{DT}}{f_{DT}} = \sqrt{\left(\frac{\Delta f_{DT}(r)}{f_{DT}(r)} \right)^2 + \left(\frac{\Delta(e^{-\lambda t_m})}{e^{-\lambda t_m}} \right)^2 + \left(\frac{\Delta C_{sum,cyc}}{C_{sum,cyc}} \right)^2}. \quad (4.23)$$

Previous cycles correction factor

Again, as for t_m and for t_b , the uncertainty in t_c is negligible. The only source of uncertainty in f_c is the decay constant and the uncertainty is calculated as follows:

$$\Delta f_c = \left[- \frac{\sum_i^n t_c(i-n-1) \cdot \Phi_T^i \cdot e^{-\lambda(n-i)t_c}}{\sum_i^n \Phi_T^i} \cdot e^{-\lambda t_c} \cdot \frac{1}{1 - e^{-\lambda t_c}} - \left(1 - \frac{\sum_i^n e^{-\lambda(n-i)t_c}}{\sum_i^n \Phi_T^i} \cdot e^{-\lambda t_c} \right) \cdot \frac{t_c \cdot e^{-\lambda t_c}}{(1 - e^{-\lambda t_c})^2} \right] \cdot \Delta\lambda. \quad (4.24)$$

Simulation factor

An uncertainty of 5% was estimated for the efficiency correction factor for all gamma energies. In addition to that, the uncertainties of the used gamma intensities I_γ were considered from published data.

$$\frac{\Delta f_{sim}}{f_{sim}} = \sqrt{\left(\frac{\Delta f_\epsilon}{f_\epsilon}\right)^2 + \left(\frac{\Delta I_\gamma}{I_\gamma}\right)^2} \quad (4.25)$$

Uncertainties for $^{103}\text{Rh}(n,\gamma)^{104g,m}\text{Rh}$

The Monte Carlo method was used to determine the propagation of the uncertainties of the time dependent quantities neutron flux, decays per cycle and the decay constants of the isomeric and the ground state of ^{97}Rh into the resulting values for the partial cross sections and the total cross section of the reaction $^{103}\text{Rh}(n,\gamma)^{104g,m}\text{Rh}$. Both, the decays per cycle and the neutron flux per time bin (0.1 seconds) were treated as statistical uncertainties. The simulated two dimensional PDF for all parameters rolled simultaneously is shown in Figure 4.49 for 5000 samples. For the estimation of the uncertainties in the partial cross sections, projections on the respective axes were fitted with normal distributions and the 1- σ width of the result was taken as the value for the particular uncertainty. Figure 4.50 shows the PDF of the total reaction cross section. In Appendix A the PDF's for single input parameter variations can be found.

In addition to the uncertainties just discussed, the uncertainties of the gamma intensity I_γ , the areal particle density μ_{areal} , the simulation factor f_{sim} , the dead time factor f_{DT} and the integrated neutron flux Φ_T has to be considered. All these quantities just represent factors in the calculation of the cross section. For this reason, the final uncertainty in the cross sections was determined by:

$$\frac{\Delta \sigma_i}{\sigma_i} = \sqrt{\left(\frac{\Delta I_\gamma}{I_\gamma}\right)^2 + \left(\frac{\Delta \mu}{\mu}\right)^2 + \left(\frac{\Delta f_{sim}}{f_{sim}}\right)^2 + \left(\frac{\Delta f_{DT}}{f_{DT}}\right)^2 + \left(\frac{\Delta \Phi_T}{\Phi_T}\right)^2}. \quad (4.26)$$

All values for the relative uncertainties of the input parameters are listed in Table B.4 in Appendix B.

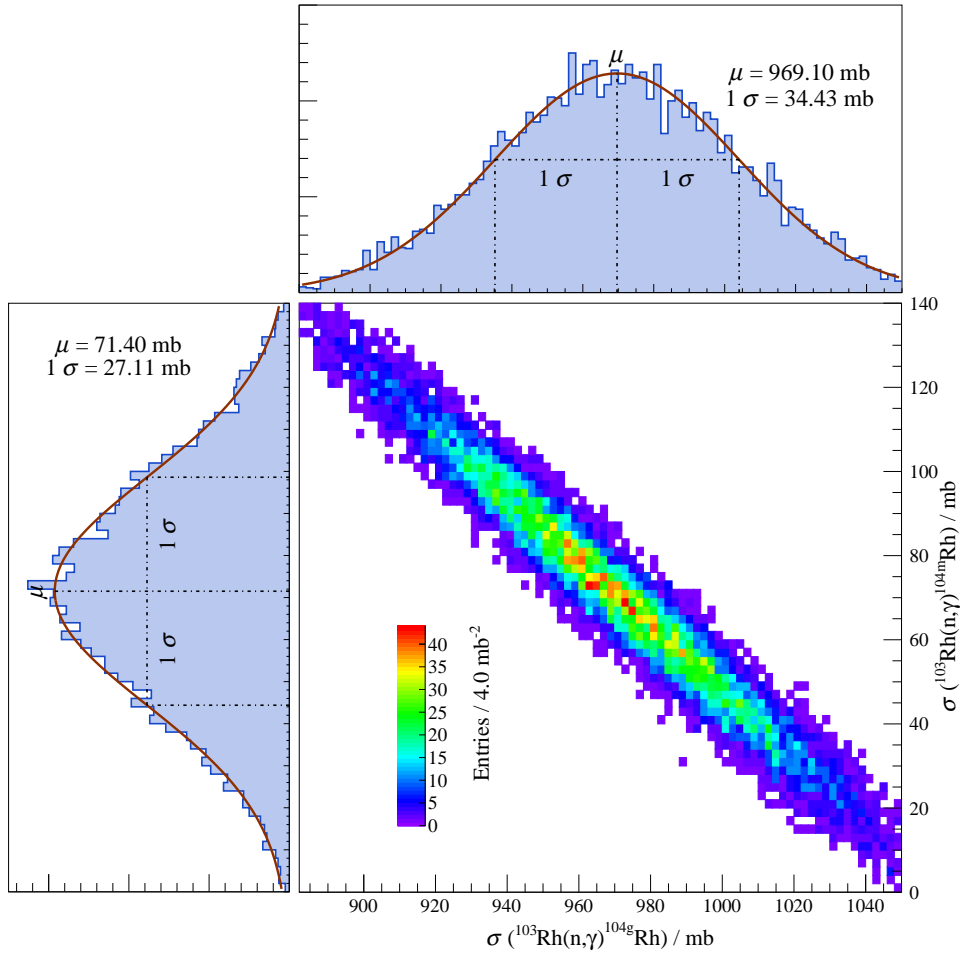


Figure 4.49: Simulated best fit results for the neutron capture cross sections on ^{103}Rh to ground and isomeric state of ^{104}Rh . The input parameter values for λ_g , λ_m , $\phi(t_n)$ and D_{cycle} are rolled randomly with a gaussian probability distribution with a width of $1\text{-}\sigma$ around their mean values.

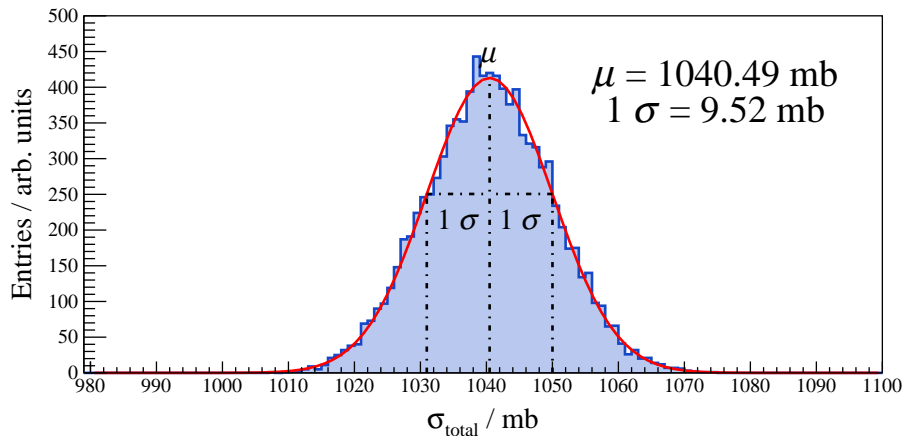


Figure 4.50: Total reaction cross section of $^{103}\text{Rh}(n,\gamma)$. The plot shows only the uncertainties contributions from parameters with an influence on the time dependent evolution of the produced nuclei, namely the decay constants λ_g and λ_m , the neutron flux per time interval $\phi(t_n)$ and the decays per cycle D_{cycle} .

Chapter 5

Results and discussion

5.1 Proton induced ruthenium activation

5.1.1 Cross section of $^{96}\text{Ru}(\text{p}, \gamma)$

$\sigma_i(E_{CM,eff}/\text{MeV})$	IT ($\sigma / \mu\text{b}$)	FX ($\sigma / \mu\text{b}$)	Direct / μb
$\sigma_g(3.132)$	90.0 ± 6.6	86.9 ± 6.5	92.4 ± 5.7
$\sigma_m(3.132)$	39.5 ± 5.3	53.3 ± 8.2	65.5 ± 6.1
$\sigma_{tot}(3.132)$	130 ± 10	140 ± 11	157.9 ± 7.4

Table 5.1: Results of the cross sections of $^{96}\text{Ru}(\text{p}, \gamma)^{97g,m}\text{Rh}$ for an effective proton energy of 3.165 MeV. The cross sections are listed separately for the iterative (IT), the FX approach and the direct analysis of peaks coming from isomeric and ground state decays only.

In Table 5.2 and 5.1 the results of the cross section measurements of $^{96}\text{Ru}(\text{p}, \gamma)$ by analysing the decay of $^{97g,m}\text{Rh}$ are shown. The uncertainties of the FX method are greater than those determined with the iterative method. The results of the methods agree within the uncertainties. For the production cross section of the isomer of ^{97}Rh at a proton energy of 3.2 MeV, the analysis of peaks coming exclusively from the isomeric decay, a large deviation between the results of different peaks was observed. The evaluation of the peaks at energies of 1587 keV and 2246 keV leads to isomer production cross sections of $\sigma_{m, E_\gamma=1587 \text{ keV}} = 109.7 \pm 9.9 \mu\text{b}$ and $\sigma_{m, E_\gamma=2245 \text{ keV}} = 110.24 \pm 8.7 \mu\text{b}$. These results are about a factor two greater than those determined by the analysis of the peaks at energies of 189 keV and 422 keV and the deviation could not be explained by the uncertainties. By varying geometry parameters in realistic ranges in the efficiency simulations, the measured peak ratios could not be reproduced by the simulations. This leads to the assumption, that the source of unknown uncertainty lies in the gamma intensity data used for the analyses. For this reason, the results of the peaks at energies of 1587 keV and 2246 keV were not considered for the final cross sections.

$\sigma_i(E_{CM,eff}/\text{MeV})$	IT (σ / mb)	FX (σ / mb)
$\sigma_g(8.889)$	1.52 ± 0.12	1.52 ± 0.14
$\sigma_m(8.889)$	2.52 ± 0.16	2.37 ± 0.35
$\sigma_{tot}(8.889)$	4.06 ± 0.24	3.88 ± 0.38
$\sigma_g(9.880)$	1.17 ± 0.08	1.15 ± 0.12
$\sigma_m(9.880)$	1.99 ± 0.13	1.99 ± 0.33
$\sigma_{tot}(9.880)$	3.14 ± 0.19	3.15 ± 0.36
$\sigma_g(10.870)$	0.62 ± 0.05	0.66 ± 0.09
$\sigma_m(10.870)$	0.74 ± 0.08	0.85 ± 0.21
$\sigma_{tot}(10.870)$	1.35 ± 0.09	1.51 ± 0.23

Table 5.2: Results of the cross sections of $^{96}\text{Ru}(p,\gamma)^{97g,m}\text{Rh}$. The cross sections are listed separately for the iterative and the FX approach.

The results for the total cross sections σ_{tot} determined by the analysis of the decay of the daughter nucleus ^{97}Ru are listed in Table 5.3. The results of this analysis led to systematically lower total cross sections (8 - 22%). Any uncertainty that would explain this deviation could not be identified. Beside the method itself, possible sources of unknown uncertainties are the decay constants of ^{97}Rh and ^{97}Ru , the simulation factors and the gamma intensities.

$E_{CM,eff} / \text{MeV}$	σ_{tot} / mb
8.889	3.49 ± 0.14
9.880	2.48 ± 0.16
10.870	1.25 ± 0.05

Table 5.3: Results for the total cross sections for $^{96}\text{Ru}(p,\gamma)^{97}\text{Rh}$ determined by measuring the electron capture decay of the daughter nucleus ^{97}Ru .

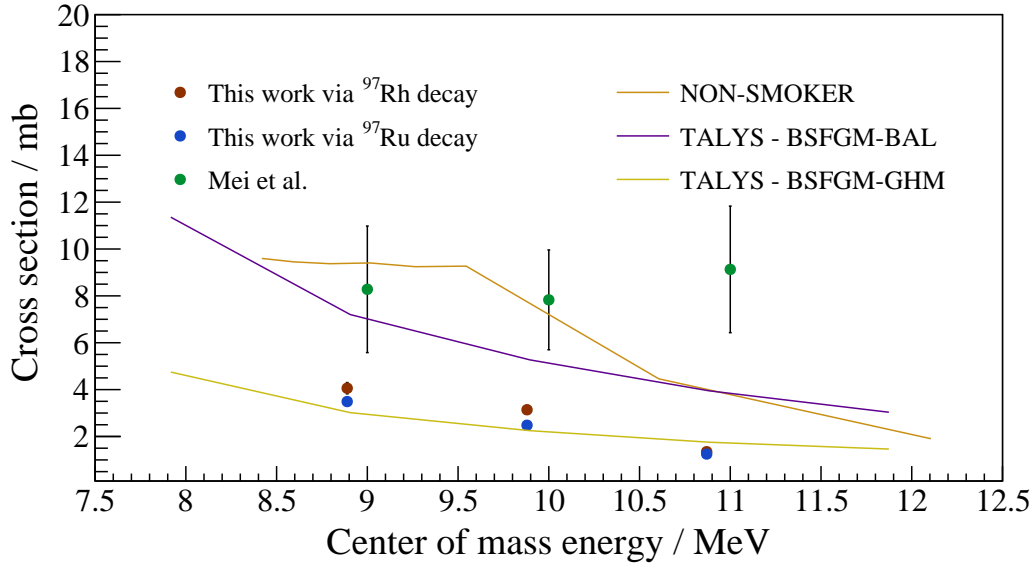


Figure 5.1: Total reaction cross section of $^{96}\text{Ru}(p,\gamma)$ at proton energies in the 10 MeV region of the present work compared with the experimental results of Mei et al. [64] and Hauser-Feshbach model predictions of the NON-SMOKER [75] and the TALYS [56] (Version 1.95) codes. Two different γ -ray strength functions suggested by Brink and Axel (Brink-Axel Lorentzian BAL) [24, 10] and Goriely [39] were used as input parameters. For the level density the back-shifted Fermi gas model was chosen.

In Figure 5.1 the results for the total reaction cross section of $^{96}\text{Ru}(p,\gamma)$ at proton energies around 10 MeV are plotted together with the results of the measurement performed in inverse kinematics at the storage ring ESR, GSI by Mei et al. [64] and theoretical predictions of the NON-SMOKER [75] and the TALYS [56] code. The values for the total cross section determined in this thesis are systematically lower than those of Mei et al.. The greatest difference between both measurements occurs at a center of mass energy of about 11 MeV, where the value for the total cross section measured by Mei et al. is about a factor of 7 times greater than the value obtained in the present work. The predictions of the NON-SMOKER code with default settings shows a good agreement with the results of Mei et al. for energies of 9 and 10 MeV. The decreasing trend of the cross section to higher energies in the predictions of NON-SMOKER is reflected in the results of the present work.

E_{CM} / MeV	σ_{tot} / mb (Mei et al.)	E_{CM} / MeV	σ_{tot} / mb (this work)
8.976	$8.28^{+2.58}_{-2.76}$	8.889	3.86 ± 0.38
9.973	$7.83^{+2.13}_{-2.59}$	9.880	2.99 ± 0.36
10.971	$9.13^{+2.59}_{-2.94}$	10.870	1.44 ± 0.23

Table 5.4: Results for the total cross sections for $^{96}\text{Ru}(p,\gamma)^{97}\text{Rh}$ of the present work calculated as the weighted mean of the FX, the IT and the ^{97}Ru decay results compared to the results of Mei et al.[64].

In addition to the activations at proton energies around 10 MeV, a measurement

at 3.2 MeV was performed to compare the results with those obtained by Bork et al. [23]. As in the present work Bork et al. an activation setup to measure proton capture cross sections on natural composed ruthenium in a proton energy range of 1.6 - 3.4 MeV. The results for the total reaction cross section as well as the partial cross sections into the ground state and the isomeric state of ^{97}Rh together with the results of Bork et al. and theoretical predictions of the Hauser-Feshbach codes TALYS and NON-SMOKER are shown in Figure 5.2. The values obtained for the total reaction cross section in the present thesis at $E_{CM} = 3.132$ are about 30% greater than those obtained by Bork et al. in this energy region. Both predictions of the theoretical calculations are overestimating the values of the cross sections. For the TALYS code, the same level density model and the same γ -ray strength function were chosen as for the energies around 10 MeV.

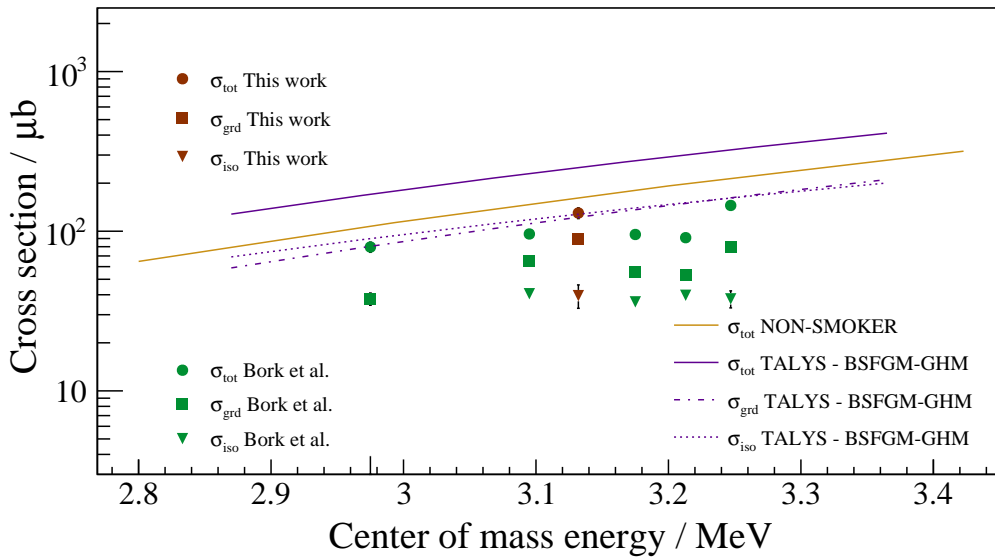


Figure 5.2: Reaction cross sections of $^{96}\text{Ru}(p,\gamma)$ at proton energies in the 3 MeV region of the present work compared with the experimental results of Bork et al. [23] and Hauser-Feshbach model predictions of the NON-SMOKER [75] and the TALYS [56] (Version 1.95) codes.

5.2 Cyclic neutron activation

5.2.1 Neutron distribution and SACS

The neutron energies and thus the energy distribution of the neutrons getting captured in the samples are important to understand the resulting values for the cross sections of the CNA. Due to vibrations on the sample holder during the movement of the sample transport slide, a safety distance between the neutron production target and the samples had to be kept. This larger distance of the samples leads to a shift of the neutron energy spectrum inside the samples towards higher neutron energies. In Figure 5.3, the simulated neutron spectra for the final setup of the CNA are shown for a sample distance of 7 mm and a lithium layer thickness of 20 μm together with MB distributions for $k_{\text{B}}T = 25 \text{ keV}$ and $k_{\text{B}}T = 30 \text{ keV}$. The

estimated neutron energy distribution shows a better agreement with a MB of $k_B T = 30$ keV. For this reason, the SACS obtained in the present work are compared with published results of MACS at 30 keV.

There was a shift in the dipole magnet voltage for the two activation measurements of silver resulting in a proton energy of $E_p = 1909$ keV. Figure 5.3 shows the slightly different neutron energy distribution simulated with a 3 keV lower proton energy (orange). Because of the small deviation between both distributions no differences were made between the results of the activations at both proton energies.

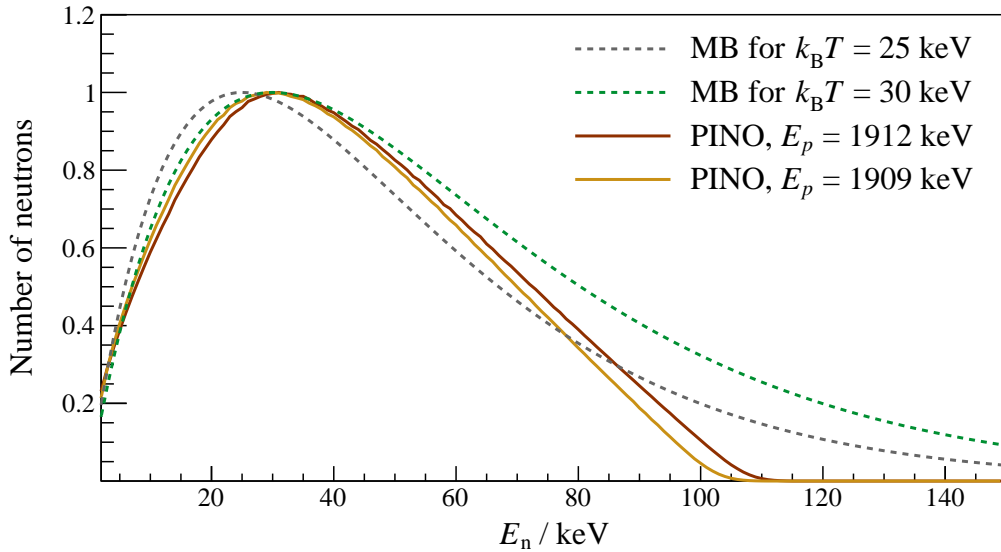


Figure 5.3: Maxwell distributions of $k_B T = 25$ keV (grey) and $k_B T = 30$ keV (green) compared with the neutron spectra in the samples for the CNA setup for proton energies of $E_p = 1912$ keV (red) and $E_p = 1909$ keV (orange) simulated with PINO [81].

5.2.2 Cross section of $^{51}\text{V}(n,\gamma)$

The *Karlsruhe Astrophysical Database of Nucleosynthesis in Stars* KADoNiS V0.3 is a database for neutron capture cross sections relevant for the s-process. The suggested value for the neutron capture reaction cross section of $^{51}\text{V}(n,\gamma)$ is 32 ± 3.4 mb. Based on evaluated values of the continuous-energy neutron library *Evaluated Nuclear Data File* (ENDFB71) [52] and the *Japanese Evaluated Nuclear Data Library* (JENDL40) [82] the preliminary KADoNiS V1.0 database suggests a MACS at 30 keV of 32.0 ± 3.4 mb. This value for the cross section is 22% greater than the one measured in the present work. A *Time of Flight* (TOF) measurement of the reaction performed by Winters et al. [90] obtained a cross section of 38 ± 4 mb. KADoNiS also lists the result of an activation experiment performed by Anand et al. (1979)[5]. They obtained a value of 16.4 ± 4 mb for the cross section, which was renormalized with a new cross section for the used monitor cross section of ^{127}I to a value of 13.7 mb for the MACS at 25 keV. Due to the $1/v$ -dependency of the cross section in the keV energy region, the derived cross section for 30 keV of this

measurement is even smaller.

Reaction	$\sigma_{\text{SACS}} / \text{mb}$	$\sigma_{^{197}\text{Au, SACS}} / \text{mb}$	$\sigma_{\text{SACS}} / \sigma_{^{197}\text{Au, SACS}}$
$^{51}\text{V}(\text{n},\gamma)^{52}\text{V}$	25.0 ± 2.2	619 ± 7 (*)	0.040 ± 0.0035

(*) Data retrived from [80]

Table 5.5: Results of the cyclic neutron activation of vanadium.

5.2.3 Cross section of $^{107}\text{Ag}(\text{n},\gamma)$

In KADoNiS V0.3, the suggested value for the total cross section of the reaction $^{107}\text{Ag}(\text{n},\gamma)^{108}\text{Ag}$ is 792 ± 30 mb. The preliminary Version 1.0 of KADoNiS suggests a total cross section of 795 ± 24 mb and a partial cross section into the isomer of ^{108}Ag of 36.5 ± 4.4 mb. These values are calculated as a weighted average of the results of four measurements ([14],[22],[62],[19]). In the present work, only the cross section into the ground state of ^{108}Ag was measured. The subtraction of the partial cross section into the isomeric state from the total cross section leads to a partial cross section into the ground state of 758.5 ± 24.4 mb, which is in a good agreement with the value obtained in the present work.

Reaction	$\sigma_{\text{SACS}} / \text{mb}$	$\sigma_{^{197}\text{Au, SACS}} / \text{mb}$	$\sigma_{\text{SACS}} / \sigma_{^{197}\text{Au, SACS}}$
$^{107}\text{Ag}(\text{n},\gamma)^{108}\text{Ag}$	742 ± 75	619 ± 7 (*)	1.200 ± 0.123

(*) Data retrived from [80]

Table 5.6: Results of the cyclic neutron activation of ^{107}Ag .

5.2.4 Cross section of $^{109}\text{Ag}(\text{n},\gamma)$

The result of the partial cross section of the reaction $^{109}\text{Ag}(\text{n},\gamma)$ into the ground state of ^{110}Ag of 730 ± 72 mb is in a good agreement with the weighted average MACS at 30 keV of the results of three TOF measurements ([22][62][19]) of 740 ± 23 mb.

Reaction	$\sigma_{\text{SACS}} / \text{mb}$	$\sigma_{^{197}\text{Au, SACS}} / \text{mb}$	$\sigma_{\text{SACS}} / \sigma_{^{197}\text{Au, SACS}}$
$^{109}\text{Ag}(\text{n},\gamma)^{110g}\text{Ag}$	730 ± 72	619 ± 7 (*)	1.179 ± 0.116

(*) Data retrived from [80]

Table 5.7: Results of the cyclic neutron activation of ^{109}Ag .

5.2.5 Cross section of $^{103}\text{Rh}(n,\gamma)$

The value for the total cross section of the reaction $^{103}\text{Rh}(n,\gamma)$ suggested by KADoNiS0.3 is 811 ± 14 mb. In KADoNiS V1.0 the suggested value for the total cross section of 866 ± 12 mb is calculated as the weighted average of the evaluated values published by ENDFB71 [52] and JENDL40 [82]. The value obtained in the present work of 1040 ± 225 mb is in agreement with the values suggested by both versions of KADoNiS within the range of uncertainty. For the partial cross section into the isomer of ^{104}Rh , no published data was found. The main source of uncertainty of the measured total and partial cross sections is the uncertainty of the value for the gamma intensity I_γ of 20%. Because summing effects are negligible, the results for the cross section can be renormalized if new data for the gamma intensity is available.

Reaction	$\sigma_{\text{SACS}} / \text{mb}$	$\sigma_{^{197}\text{Au}, \text{SACS}} / \text{mb}$	$\sigma_{\text{SACS}} / \sigma_{^{197}\text{Au}, \text{SACS}}$
$^{103}\text{Rh}(n,\gamma)^{104g}\text{Rh}$	969 ± 212	619 ± 7 (*)	1.565 ± 0.342
$^{103}\text{Rh}(n,\gamma)^{104m}\text{Rh}$	71 ± 44	619 ± 7 (*)	0.115 ± 0.025
$^{103}\text{Rh}(n,\gamma)^{104}\text{Rh}$ (total)	1040 ± 225	619 ± 7 (*)	1.680 ± 0.363

(*) Data retrieved from [80]

Table 5.8: Results of the cyclic neutron activation of ^{103}Rh .

Chapter 6

Conclusion and Outlook

In the present thesis, radiative proton and neutron capture reaction cross sections were measured by means of the activation method. The goal of the proton activation of ruthenium was to verify both the experimentally determined results of Mei et al. [64] at proton energies around 10 MeV and the results of Bork et al. at a proton energy around 3 MeV [23].

The cross section obtained at 3.2 MeV is slightly higher than those measured by Bork et al., who also used the activation method (see Tab. 5.1 and Fig. 5.2). One difference between both measurements is the thickness of the ruthenium samples used for the activations, which was about three times greater in the present work than in the measurement of Bork et al.. This leads to a greater energy loss inside the ruthenium layer and a different effective energy distribution of the protons when they get captured (see Chap. 4.1.5).

The result obtained for the total proton capture cross sections on ^{96}Ru at proton energies around 10 MeV of the present work are a factor of about two for $E_p = 9$ MeV and a factor of about 7 for $E_p = 11$ MeV lower than those measured by Mei et al. (see Fig. 5.1 and Tab. 5.4). Uncertainties that could explain this deviation could not be identified within this work. This unknown uncertainty should have only an impact on the values for the cross sections at proton energies around 10 MeV and keep the fairly good agreement with the measurement of Bork et al. at a proton energy of 3.2 MeV.

The method of proton and alpha capture reaction studies in inverse kinematics is a powerful tool to measure reaction cross sections on isotopes, that are inaccessible for other methods and thus contribute new data for nuclear astrophysics. However, in order to be able to rely on the data obtained with the method, cross checks with results obtained by well-established experimental methods are necessary. Due to the deviations between the results obtained in the present work and the results obtained by Mei et al., further investigations that do not only include the comparison with theoretical model predictions, but also with experimental data obtained with different methods is highly recommended.

The results of the CNA are all in a good agreement with published results. Only the cross section of $^{51}\text{V}(n,\gamma)$ is about 22% smaller than the value suggested by KADoNiS V1.0, that is based on evaluated values extracted from ENDFB71 and JENDL40. For the cross sections of $^{107}\text{Ag}(n,\gamma)$, $^{109}\text{Ag}(n,\gamma)$ and $^{103}\text{Rh}(n,\gamma)$, the obtained values for the SACS are in a good agreement with the MACS at 30 keV suggested by KADoNiS V1.0. To determine the partial reaction cross sections into

the isomer of ^{104}Rh , the evolution of the decays per cycle with gammas coming from the ground state of ^{104}Rh only was simulated and optimized with an iterative approach. With this method, the partial cross section into the isomer of ^{97}Rh could be extracted indirectly from the evolution of ground state decays with time. Because the sensitivity on the production yield of the isomer is small, the uncertainty in the final result for the partial isomeric cross section coming from time dependent parameters amounts to about 38%. Another dominant source of uncertainty, not only for the partial cross section into the isomer, but also for the partial cross section into the ground state and the total cross section, is the uncertainty of the gamma intensity which is stated to be 20%.

Another method to measure the partial cross section into the isomeric state of ^{104}Rh is detecting the gamma radiation coming from the IT decay directly. Due to a noise suppression at low energies applied for the clover detector, the dominant gamma emission at a energy of 51.4 keV with a gamma intensity of 48.3% was not accessible with the setup. However, this could be easily achieved by using detectors with a high efficiency at low energies, just like the head-to-head setup with two BEGe detectors at IAP/GUF. Because of the half-life of 4.34 m, sufficient statistic should already be reached in a single activation and no cyclic setup is needed.

The analyses of the isotopes within the CNAA presented in this work were part of a measurement campaign established and carried out together with Meiko Volkandt, who set his focus on the neutron capture cross sections of the isotopes ^{19}F , ^{45}Sc , ^{115}In , ^{177}Hf and ^{178}Hf [88]. The agreement of the results of all the cross sections with available data is a good benchmark for the new setup for cyclic neutron activation upgrade for the neutron activation site at the IKF at GUF. Without any further upgrades, the setup allows to measure neutron capture cross sections on isotopes with half-lives of the product isotopes down to the order of 1 s. In the thesis of Volkandt [88], a list of accessible reactions is given.

Another upgrade of the neutron activation setup at IKF/GUF done recently regards the energy distribution of the neutrons. By performing activations with different geometric parameters like the distance between the neutron production layer and the sample, the neutron distribution inside the sample can be modified. By superimposing these neutron distributions with different weighing factors it is possible to mimic quasi-stellar distributions for different temperatures like the $k_{\text{B}}T = 90 \text{ keV}$ that is assumed during the carbon shell burning of the weak s-process [71]. An optimizer method invented by Philipp Erbacher (to be published) allows to obtain scaling factors for the cross sections of the different measurements to determine the final SACS. Typically, about six measurements with different geometries are sufficient for a meaningful analysis [25]. This method can be combined with the CNAA setup to investigate neutron capture cross sections with short half-lives relevant for the weak s-process.

Chapter 7

Zusammenfassung

Die vorliegende Arbeit beschreibt zwei Experimente zur Bestimmung von Wirkungsquerschnitten von Neutronen- und Protoneneinfangreaktionen, welche relevant für Nukleosyntheseprozesse in astrophysikalischen Szenarien sind. In beiden Versuchen wurde die Methode der Aktivierung verwendet, bei welcher Proben mit den jeweiligen Teilchen bestrahlt werden und anschließend durch den Zerfall der Produkte auf die Häufigkeit der stattgefundenen Reaktionen zurückgeschlossen wird. Dadurch, dass es sich in dem einen Fall um Protonen und in dem anderen um Neutronen als eingehende Teilchen handelt, unterscheiden sich die experimentellen Anforderungen und damit die Versuchsaufbauten wesentlich voneinander. Im Folgenden wird ein kurzer Überblick über die Details der Versuche sowie deren Ergebnisse und deren Einordnung in den wissenschaftlichen Kontext gegeben.

In einem Aktivierungsexperiment wurde der Wirkungsquerschnitt der Protoneneinfangsreaktion $^{96}\text{Ru}(p,\gamma)$ bestimmt. Die Motivation für die Messung lag darin, die Ergebnisse mit denen von Mei et al. [64] bestimmten zu vergleichen. Diese verwendeten die Methode der *inversen Kinematik* am Schwerionen-Speicherring ESR am GSI Helmholtzzentrum für Schwerionenforschung GmbH - Darmstadt, Deutschland. Bisher konnten Ergebnisse für Wirkungsquerschnitte, welche mit dieser Methode bestimmt wurden, ausschließlich mit theoretischen Vorhersagen verglichen werden. Die Ergebnisse des Experimentes der vorliegenden Arbeit ermöglichen erstmals einen Vergleich mit experimentell bestimmten Wirkungsquerschnitten bei gleichen Protonenenergien von 9 MeV, 10 MeV und 11 MeV. Eine weitere Messung wurde bei einer Protonenenergie von 3,2 MeV durchgeführt, um das Ergebnis mit denen von Bork et al. [23] zu vergleichen, welche ebenfalls die Aktivierungsmethode verwendeten.

Die Aktivierungsmessungen wurden am Institute of Structure and Nuclear Astrophysics ISNAP - Notre Dame, USA durchgeführt. Dazu wurden natürliche Rutheniumproben mit Protonenströmen zwischen 600 nA und 3 μA bestrahlt. Zur Bestimmung der Anzahl der stattgefundenen Reaktionen wurden die aktivierten Proben nach den Aktivierungen vor einen *high purity germanium* (HPGe) Detektor positioniert und durch Gammaspektroskopie die Anzahl der Zerfälle der produzierten Kerne bestimmt. Dabei musste berücksichtigt werden, dass der Protoneneinfang sowohl in den Grundzustand von ^{97}Rh als auch in den Isomierzustand ^{97m}Rh führen kann. Bei den Aktivierungen mit hohen Protonenenergien von 9 MeV bis 11 MeV konnten Peaks, welche ausschließlich aus dem Zerfall des Grundzustandes oder des Isomierzustandes stammen, aufgrund eines zu niedrigen Signal-zu-Untergrund-Verhältnisses nicht ausgewertet werden. Der einzige Peak, welcher für die Bestim-

mung der Anzahl der Zerfälle zur Verfügung stand, liegt bei einer Gammaenergie von 422 keV. Dieser hat Anteile sowohl aus den Zerfällen des Grundzustandes von ^{97}Rh als auch des Isomierzustandes ^{97m}Rh . Das Verhältnis der Wirkungsquerschnitte in den Grundzustand und in Isomierzustand wurde über den zeitlichen Verlauf des Peakinhaltes bestimmt. Damit konnten sowohl die partiellen Wirkungsquerschnitte als auch der totale Wirkungsquerschnitt bestimmt werden. Zusätzlich wurde der totale Wirkungsquerschnitt durch die Messung des Zerfalls des Tochterkerns ^{97}Ru bestimmt. Die Ergebnisse der Messungen bei den Protonenenergien von 9 MeV, 10 MeV und 11 MeV liegen systematisch unter denen, welche von Mei et al. bestimmt wurden. Bei einer Protonenenergie von 9 MeV liegt der gemessene Wert für den totalen Wirkungsquerschnitt σ_{tot} mit 3.86 ± 0.38 mb etwa um einen Faktor 2, bei einer Protonenenergie von 11 MeV mit $\sigma_{tot}(11 \text{ MeV}) = 1.44 \pm 0.23$ mb etwa um einen Faktor 7 niedriger. Unsicherheiten, welche diese Abweichungen der Ergebnisse der beiden Methoden erklären können, konnten nicht abschließend identifiziert werden. Die Ergebnisse für die partiellen Wirkungsquerschnitte sowie für den totalen Wirkungsquerschnitt bei einer Protonenenergie von 3,2 MeV stimmen im Rahmen der Unsicherheiten gut mit denen von Bork et al. gemessenen überein. Ein Vergleich der Ergebnisse der Messungen zusammen mit Vorhersagen theoretischer Modelle sind in den Abbildungen 7.1 und 7.2 gezeigt.

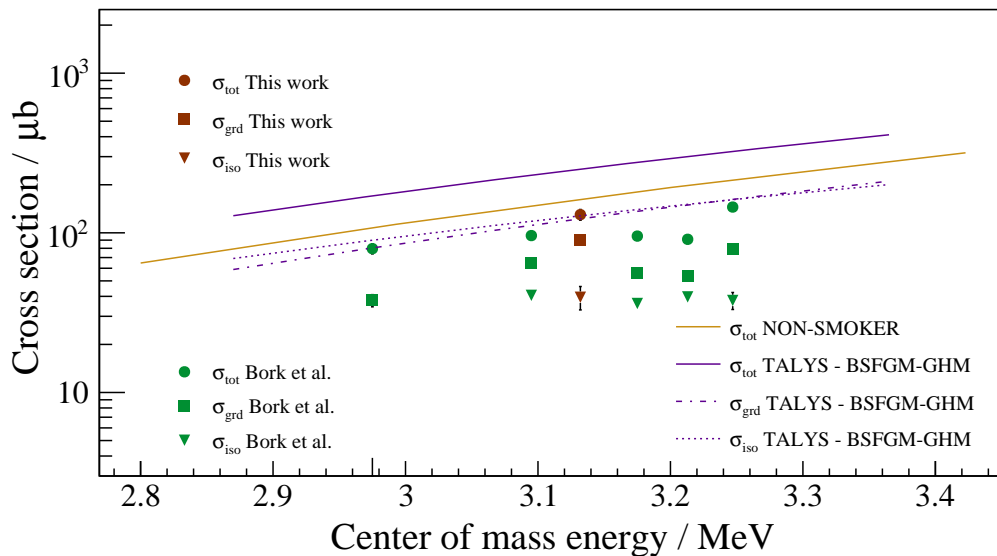


Figure 7.1: Partielle und totaler Wirkungsquerschnitt der Reaktion $^{96}\text{Ru}(p,\gamma)$ bei Protonenenergien um 3 MeV der vorliegenden Arbeit verglichen mit den Ergebnissen von Bork et al. [23] and Hauser-Feshbach Rechnungen von NON-SMOKER [75] TALYS [56] (Version 1.95).

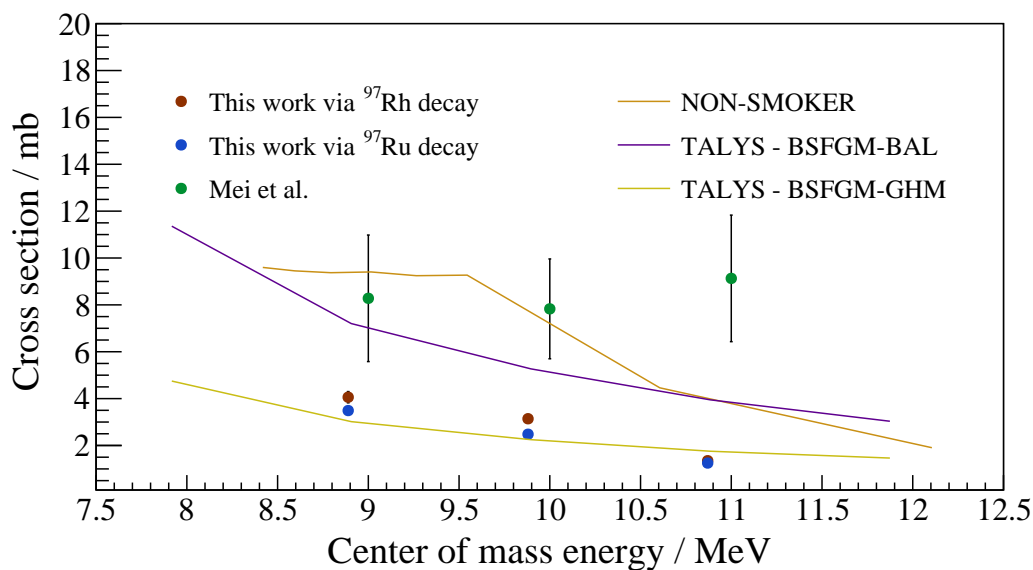


Figure 7.2: Totaler Wirkungsquerschnitt der Reaktion $^{96}\text{Ru}(p,\gamma)$ bei Protonenenergien um 10 MeV der vorliegenden Arbeit verglichen mit den Ergebnissen von Mei et al. [64] und Hauser-Feshbach-Berechnungen von NON-SMOKER [75] und TALYS [56] (Version 1.95).

Der zweite Teil der vorliegenden Arbeit befasst sich mit einem Experiment zur Bestimmung von Neutroneneinfangwirkungsquerschnitten mittels zyklischer Aktivierung. Hierzu wurde der am Institut für Kernphysik bereits bestehende Aufbau um eine elektrisch getriebene Linearführung erweitert, welche die Proben von der Aktivierungsposition vor dem Lithiumtarget zur Auszählungposition vor einen HPGe-Detektor und wieder zurück transportiert. Der Aufbau ist in Abbildung 7.4 gezeigt. Zur Erzeugung der Neutronen wurde die Reaktion $^7\text{Li}(p,n)$ verwendet, welche bei einer Protonenenergie von $E_p = 1912$ keV knapp oberhalb der Reaktionsschwelle von 1880.57 keV ein quasi-maxwellverteiltes Neutronenenergiespektrum innerhalb der bestrahlten Proben ermöglicht.

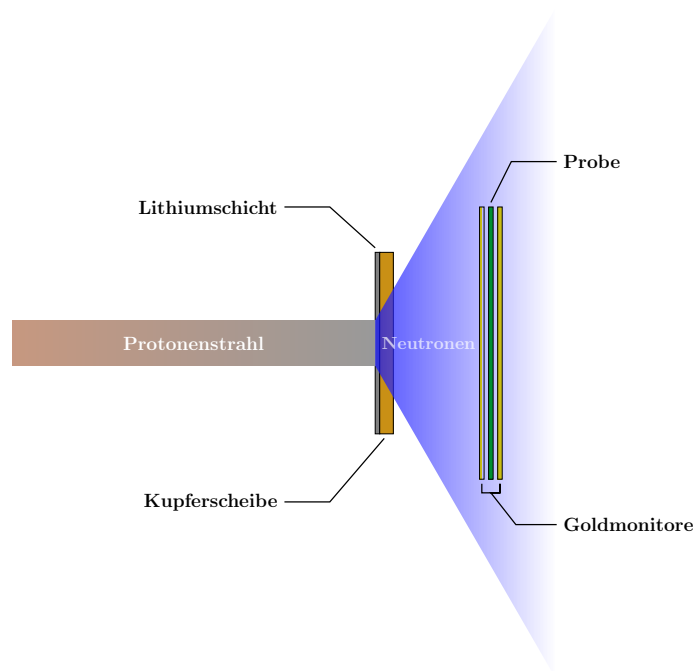


Figure 7.3: Aufbau des Lithiumtargets zur Produktion von quasi-maxwellverteilten Neutronenenergien. Goldfolien vor und hinter den Proben wurden als Monitore zur Bestimmung des integrierten Neutronenflusses verwendet.

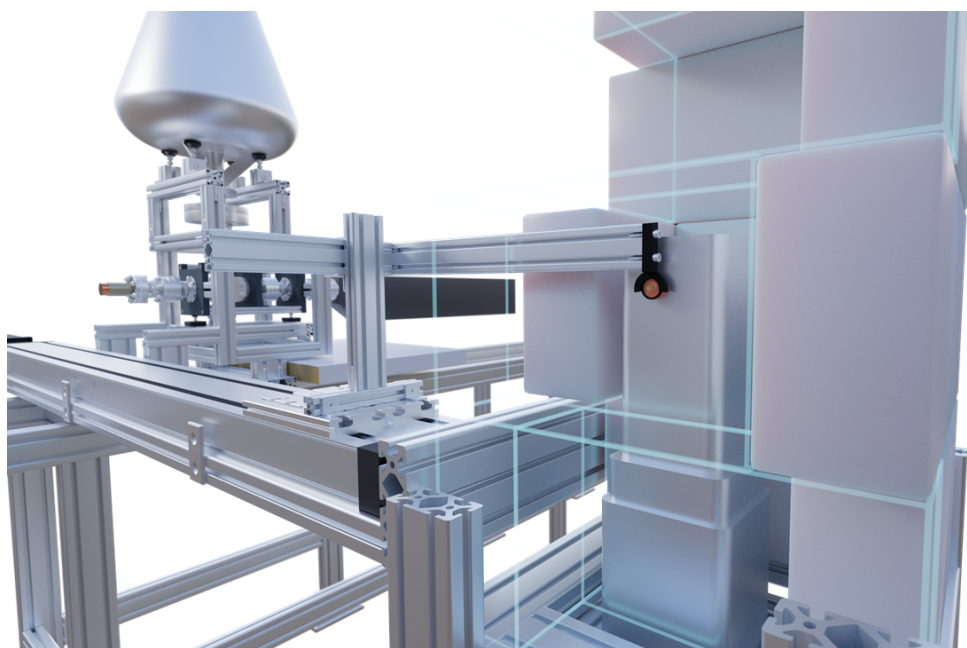


Figure 7.4: Visualisierung des Aufbaus zur zyklischen Aktivierung von Proben mit Neutronen am Institut für Kernphysik IKF - Goethe Universität Frankfurt. Links hinten ist das Lithiumtarget zur Produktion von Neutronen zu sehen, welches den Abschluss des Strahlrohres bildet. Auf der rechten Seite im Vordergrund ist der Detektor innerhalb der Abschirmung aus Paraffinblöcken dargestellt. Die Probe befindet sich in der Auszählungsposition vor dem Detektor.

Der neue Aufbau zur zyklischen Aktivierung ermöglicht die Messung von Wirkungsquerschnitten von Proben, deren produzierte Kerne kurze Halbwertszeiten von bis zu einer Sekunde besitzen. In einer ersten Messkampagne wurden die Wirkungsquerschnitte der Reaktionen $^{51}\text{V}(n,\gamma)^{52}\text{V}$, $^{107}\text{Ag}(n,\gamma)^{108}\text{Ag}$, $^{109}\text{Ag}(n,\gamma)^{110}\text{Ag}$ und $^{103}\text{Rh}(n,\gamma)^{104g,m}\text{Rh}$ gemessen. Zur Analyse der partiellen Wirkungsquerschnitte in den Grundzustand mit einer Halbwertszeit von 42,3s und in den Isomierzustand mit einer Halbwertszeit von 4.34 m von ^{104}Rh , welcher mit einer Wahrscheinlichkeit von 99.87% über internen Übergang in den Grundzustand zerfällt, wurde der zeitliche Verlauf der Zerfälle pro Zyklus betrachtet. Hierfür wurden die Zerfälle pro Zyklus simuliert und mit den Produktionsraten in den Grundzustand und das Isomer als freie Parameter an die gemessenen Daten angepasst. In Abbildung 7.5 ist das Ergebnis der Anpassung für die Zerfälle pro Zyklus unter Berücksichtigung des zeitabhängigen Neutronenflusses dargestellt. Die Ergebnisse der Messungen zeigen innerhalb der Fehlergrenzen gute Übereinstimmung mit bereits existierenden Daten. Die Ergebnisse sind in Tabelle 7.1 zusammengefasst.

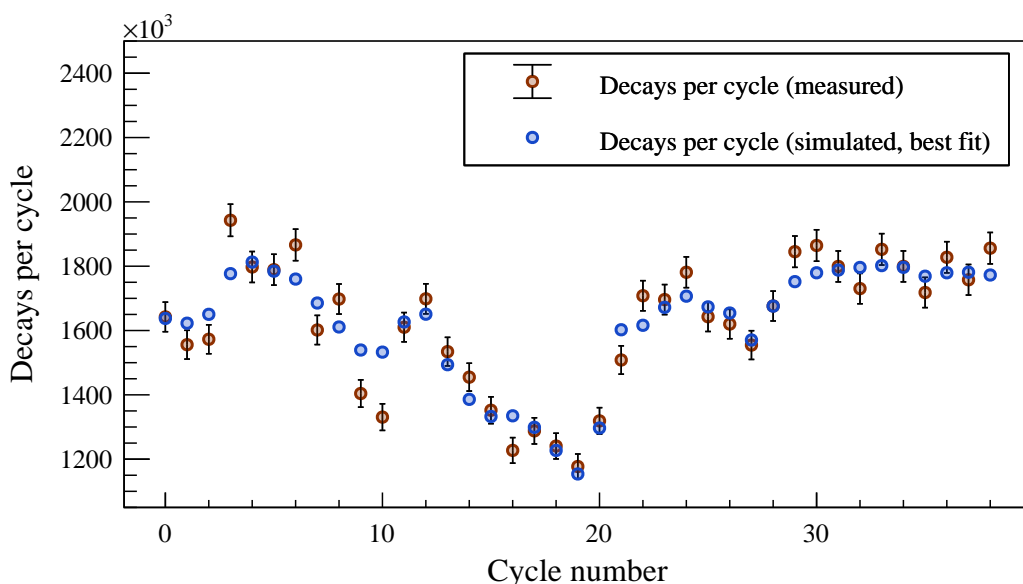


Figure 7.5: Gemessene (rot) und simulierte (blau) Zerfälle pro Zyklus unter Berücksichtigung des zeitabhängigen Neutronenflusses.

Reaction	$\sigma_{\text{SACS}} / \text{mb}$	$\sigma_{^{197}\text{Au, SACS}} / \text{mb}$	$\sigma_{\text{SACS}} / \sigma_{^{197}\text{Au, SACS}}$
$^{51}\text{V}(n,\gamma)^{52}\text{V}$	25.0 ± 2.2	619 ± 7 (*)	0.040 ± 0.0035
$^{107}\text{Ag}(n,\gamma)^{108}\text{Ag}$	742 ± 75	619 ± 7 (*)	1.200 ± 0.123
$^{109}\text{Ag}(n,\gamma)^{110g}\text{Ag}$	730 ± 72	619 ± 7 (*)	1.179 ± 0.116
$^{103}\text{Rh}(n,\gamma)^{104g}\text{Rh}$	969 ± 212	619 ± 7 (*)	1.565 ± 0.342
$^{103}\text{Rh}(n,\gamma)^{104m}\text{Rh}$	71 ± 44	619 ± 7 (*)	0.115 ± 0.025
$^{103}\text{Rh}(n,\gamma)^{104}\text{Rh}$ (total)	1040 ± 225	619 ± 7 (*)	1.680 ± 0.363

(*) Data retrieved from [80]

Table 7.1: Results for the cross sections of the cyclic neutron activation.

Appendix A

Disentangled uncertainties of the $^{103}\text{Rh}(n, \gamma)$ cross section

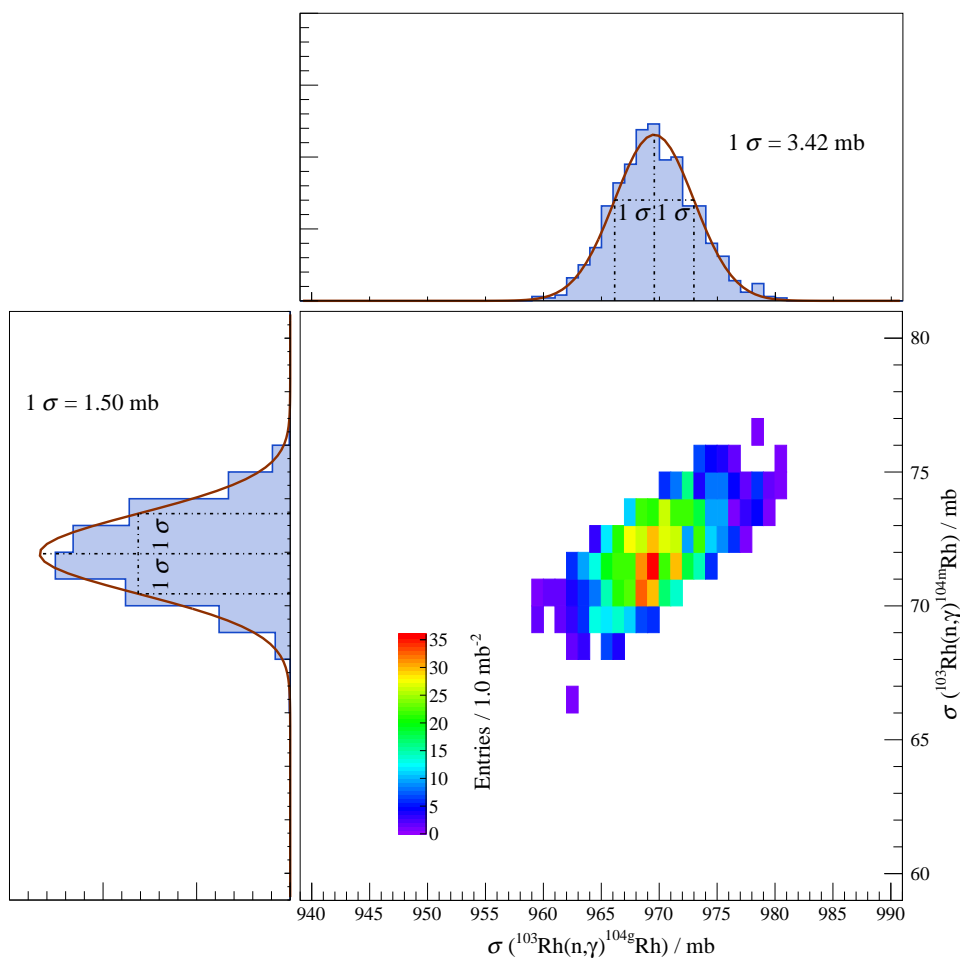


Figure A.1: Simulated uncertainty in σ_{grd} and σ_{iso} for λ_{grd} rolled with a gaussian probability distribution with a $1\text{-}\sigma$ width.

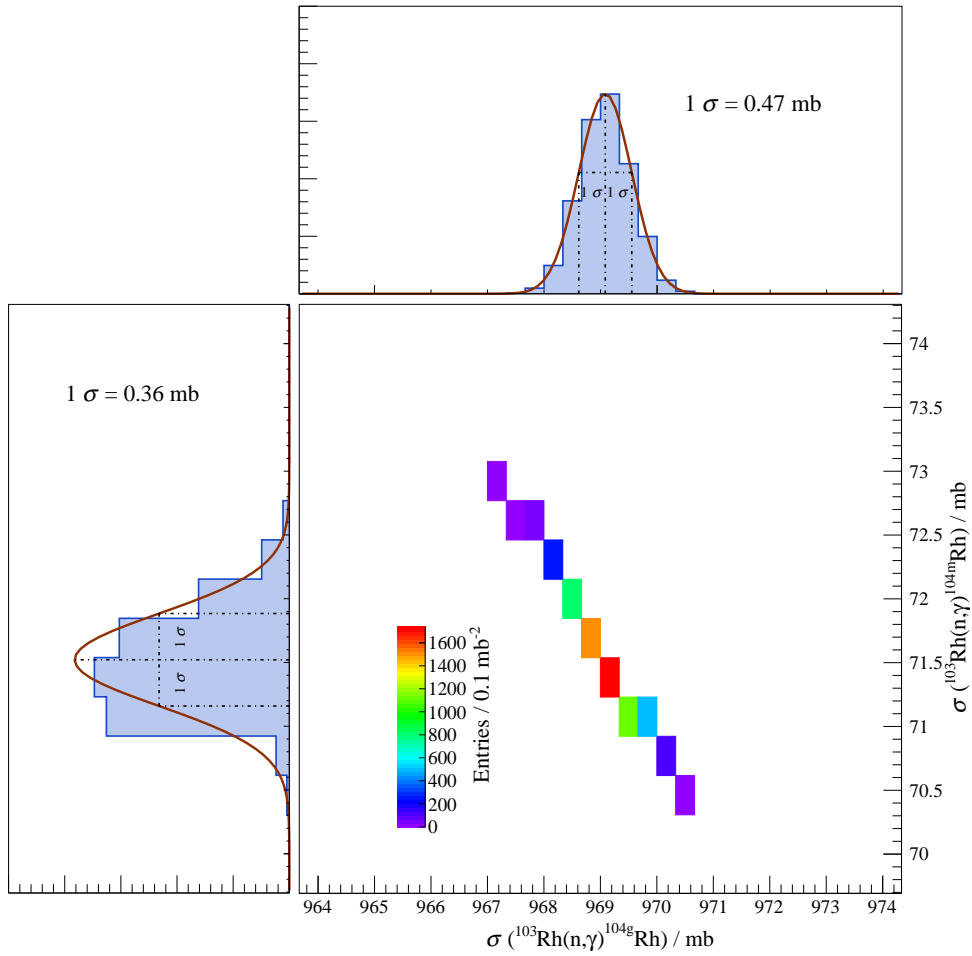


Figure A.2: Simulated uncertainty in σ_{grd} and σ_{iso} for λ_{iso} rolled with a Gaussian probability distribution with a $1\text{-}\sigma$ width.

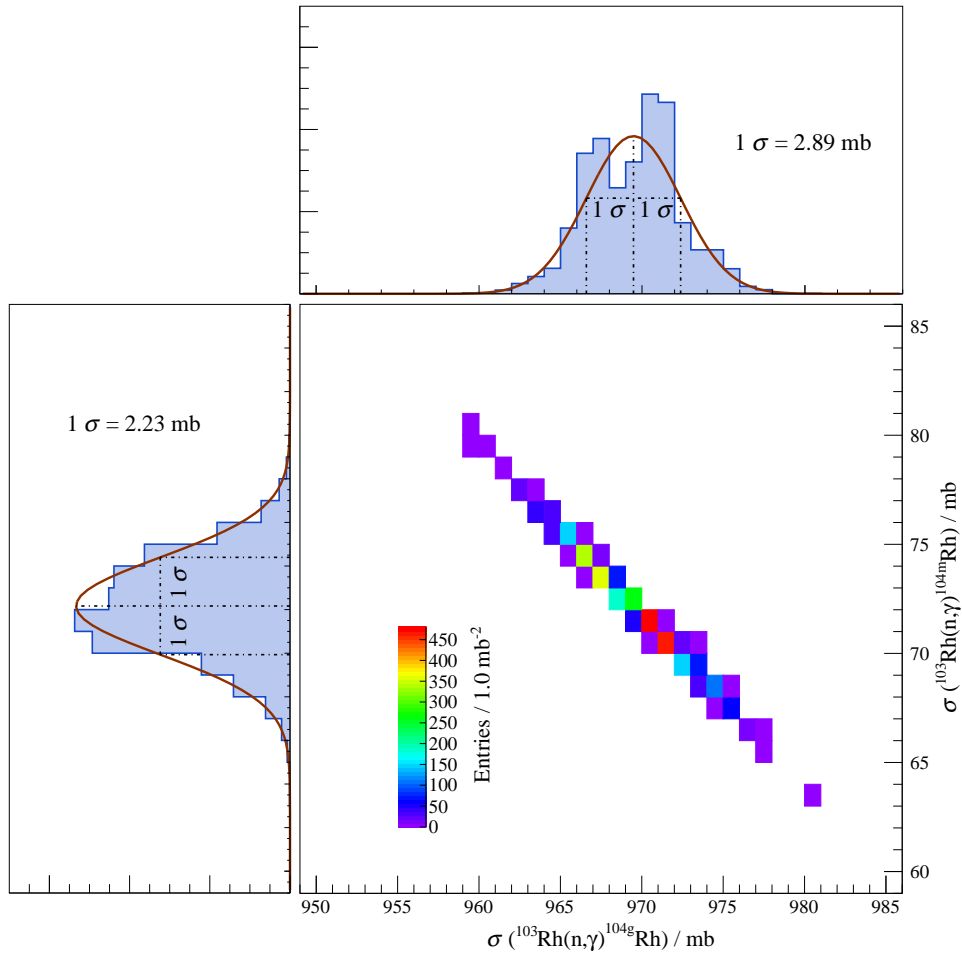


Figure A.3: Simulated uncertainty in σ_{grd} and σ_{iso} for $\phi(t_n)$ rolled with a gaussian probability distribution with a $1\text{-}\sigma$ width for each time bin.

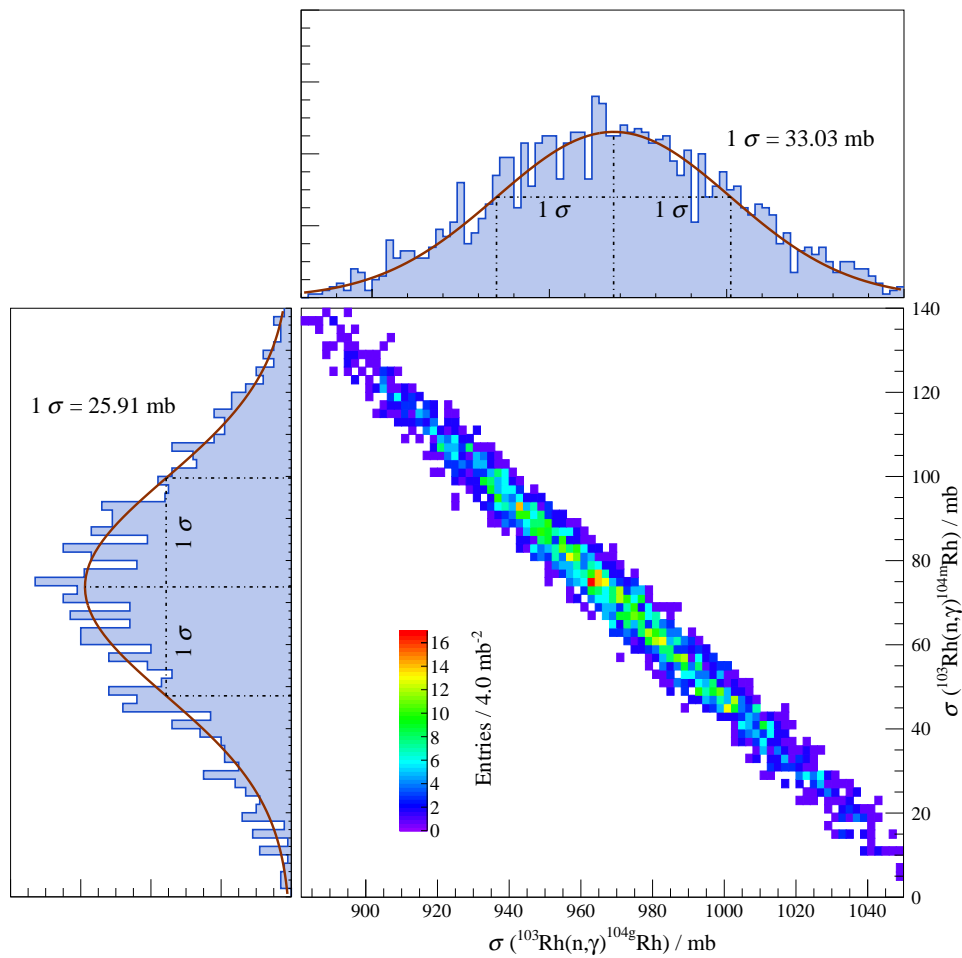


Figure A.4: Simulated uncertainty in σ_{grd} and σ_{iso} for decays per cycle rolled with a gaussian probability distribution with a $1\text{-}\sigma$ width (statistical error of accumulated counts per cycle).

Appendix B

Parameters of the CNA analysis

Parameter name	Value X	$\frac{\Delta X}{X}$ / %
$C_{1434\text{ keV}}$	154274	0.25
$I_{\gamma,1434\text{ keV}}(E_{\gamma})$ (*)	1	1.4
$t_{1/2}$ (*)	3.743 m	1.3
μ	$2.0453 \cdot 10^{21} \text{ cm}^{-2}$	2.4
Φ_T	$4.551 \cdot 10^{11}$	3.7
f_{sim}	0.0165	5
f_w	0.9756	0.004
f_m	0.7692	0.06
f_b	0.9822	0.1
f_c	1.0486	0.02
f_{DT}	0.9766	4.98

(*) Data retrieved from [33]

Table B.1: Parameters of the cyclic neutron activation of ^{51}V with their corresponding relative uncertainties in percent.

Parameter name	Value X	$\frac{\Delta X}{X}$ / %
$C_{633 \text{ keV}}$	23421	0.65
$I_{\gamma, 633 \text{ keV}}$ (*)	0.0176	5.7
b_{β^-} (*)	0.9715	0.21
$t_{1/2}$ (*)	2.382 m	0.46
μ	$1.5241 \cdot 10^{20} \text{ cm}^{-2}$	2.02
Φ_T	$8.464 \cdot 10^{11}$	3.55
f_{sim}	0.0006305	5
f_w	0.96194	0.017
f_m	0.76202	0.21
f_b	0.528841	0.34
f_c	1.05271	0.07
f_{DT}	0.9782	5.2

(*) Data retrieved from [16]

Table B.2: Parameters of the cyclic neutron activation of ^{107}Ag with their corresponding relative uncertainties in percent.

Parameter name	Value X	$\frac{\Delta X}{X}$ / %
$C_{658 \text{ keV}}$	31965	0.56
$I_{\gamma, 658 \text{ keV}}$ (*)	0.045	5.4
b_{β^-} (*)	0.9970	0.06
$t_{1/2}$ (*)	24.56 s	0.45
μ	$1.41594 \cdot 10^{20} \text{ cm}^{-2}$	2.0
Φ_T	$7.010 \cdot 10^{11}$	3.5
f_{sim}	0.0015167	5
f_w	0.733	0.14
f_m	0.727	0.22
f_b	0.5477	0.19
f_c	1.04616	0.064
f_{DT}	0.967	5.1

(*) Data retrieved from [43]

Table B.3: Parameters of the cyclic neutron activation of ^{109}Ag with their corresponding relative uncertainties in percent.

Parameter name	Value X	$\frac{\Delta X}{X}$ / %
$I_{\gamma,556 \text{ keV}}(E_{\gamma})$ (*)	0.02	20
b_{IT} (*)	99.87	0.01
$t_{1/2}^g$ (*)	42.3 s	0.95
$t_{1/2}^m$ (*)	4.34 m	0.7
μ	$3.686 \cdot 10^{20} \text{ cm}^{-2}$	2
Φ_T	$4.526 \cdot 10^{11}$	3.5
f_{sim}	0.0392	5
f_{DT}	0.967	5
$\Delta f_{iter.,g}$		3.56
$\Delta f_{iter.,m}$		38
$\Delta f_{iter.,tot}$		3.56

(*) Data retrived from [17]

Table B.4: Parameters of the cyclic neutron activation of ^{103}Rh with their corresponding relative uncertainties in percent. The factors $f_{iter.,i}$ contain the uncertainties of the decay constants λ_i , the uncertainty of the neutron flux in every time bin $\phi(t_n)$ and the statistical uncertainty of the peak content per cycle propagated into the ground state, the isomeric and the total cross section.

Appendix C

Equations for the production and decay of ^{97}Ru

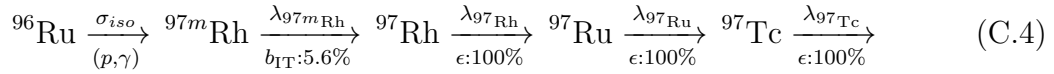
The following equations describe the production and decay of ^{97}Ru during the irradiation of ^{96}Ru with protons. To find the solutions of the respective system of differential equations the formalism invented by Bateman[12] described in Chapter 2.2 was used.

$$N_n(t_b) = \Lambda_1^* \Lambda_2^* \Lambda_{n-1}^* N_1^0 \sum_{i=1}^n C_i \exp(-\Lambda_i t_b) \quad (\text{C.1})$$

$$C_i = \prod_{j=i}^{n-1} \frac{1}{\Lambda_j - \Lambda_i} (j \neq i) \quad (\text{C.2})$$

$$\Lambda = \lambda + \varphi\sigma \quad (\text{C.3})$$

Calculation of $N'(t_b)$ for one production and decay branch:



$$\Lambda_1 = \varphi(\sigma_{\text{grd}} + \sigma_{\text{iso}}) \quad (\text{C.5})$$

$$\Lambda_1^* = \varphi\sigma_{\text{iso}} \quad (\text{C.6})$$

$$\Lambda_2 = \lambda_{97m}\text{Rh} \quad (\text{C.7})$$

$$\Lambda_2^* = b_{IT}\lambda_{97m}\text{Rh} \quad (\text{C.8})$$

$$\Lambda_3 = \lambda_{97}\text{Rh} \quad (\text{C.9})$$

$$\Lambda_3^* = \lambda_{97}\text{Rh} \quad (\text{C.10})$$

$$\Lambda_4 = \lambda_{97}\text{Ru} \quad (\text{C.11})$$

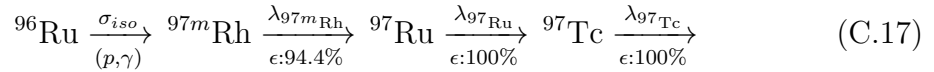
$$\begin{aligned} C_1 &= \frac{1}{(\Lambda_2 - \Lambda_1)(\Lambda_3 - \Lambda_1)(\Lambda_4 - \Lambda_1)} \\ &= \frac{1}{(\lambda_{97m}\text{Rh} - \varphi(\sigma_{\text{grd}} + \sigma_{\text{iso}}))(\lambda_{97}\text{Rh} - \varphi(\sigma_{\text{grd}} + \sigma_{\text{iso}})) - (\lambda_{97}\text{Ru} - \varphi(\sigma_{\text{grd}} + \sigma_{\text{iso}}))} \quad (\text{C.12}) \end{aligned}$$

$$\begin{aligned}
 C_2 &= \frac{1}{(\Lambda_1 - \Lambda_2)(\Lambda_3 - \Lambda_2)(\Lambda_4 - \Lambda_2)} \\
 &= \frac{1}{(\varphi(\sigma_{\text{grd}} + \sigma_{\text{iso}}) - \lambda_{97m\text{Rh}})(\lambda_{97m\text{Rh}} - \lambda_{97\text{Rh}})(\lambda_{97\text{Ru}} - \lambda_{97\text{Rh}})}
 \end{aligned} \tag{C.13}$$

$$\begin{aligned}
 C_3 &= \frac{1}{(\Lambda_1 - \Lambda_3)(\Lambda_2 - \Lambda_3)(\Lambda_4 - \Lambda_3)} \\
 &= \frac{1}{(\varphi(\sigma_{\text{grd}} + \sigma_{\text{iso}}) - \lambda_{97\text{Rh}})(\lambda_{97m\text{Rh}} - \lambda_{97\text{Rh}})(\lambda_{97\text{Ru}} - \lambda_{97\text{Rh}})}
 \end{aligned} \tag{C.14}$$

$$\begin{aligned}
 C_4 &= \frac{1}{(\Lambda_1 - \Lambda_4)(\Lambda_2 - \Lambda_4)(\Lambda_3 - \Lambda_4)} \\
 &= \frac{1}{(\varphi(\sigma_{\text{grd}} + \sigma_{\text{iso}}) - \lambda_{97\text{Ru}})(\lambda_{97m\text{Rh}} - \lambda_{97\text{Ru}})(\lambda_{97\text{Rh}} - \lambda_{97\text{Ru}})}
 \end{aligned} \tag{C.15}$$

$$\begin{aligned}
 N^1(t_b) &= N_1^0 \varphi \sigma_{\text{iso}} b_{\text{IT}} \lambda_{97m\text{Rh}} \lambda_{97\text{Rh}} \times \\
 &\left\{ \frac{\exp(-\varphi(\sigma_{\text{grd}} + \sigma_{\text{iso}})t_b)}{(\lambda_{97m\text{Rh}} - \varphi(\sigma_{\text{grd}} + \sigma_{\text{iso}}))(\lambda_{97\text{Rh}} - \varphi(\sigma_{\text{grd}} + \sigma_{\text{iso}}))(\lambda_{97\text{Ru}} - \varphi(\sigma_{\text{grd}} + \sigma_{\text{iso}}))} \right. \\
 &+ \frac{\exp(-\lambda_{97m\text{Rh}}t_b)}{(\varphi(\sigma_{\text{grd}} + \sigma_{\text{iso}}) - \lambda_{97m\text{Rh}})(\lambda_{97m\text{Rh}} - \lambda_{97\text{Rh}})(\lambda_{97\text{Ru}} - \lambda_{97\text{Rh}})} \\
 &+ \frac{\exp(-\lambda_{97\text{Rh}}t_b)}{(\varphi(\sigma_{\text{grd}} + \sigma_{\text{iso}}) - \lambda_{97\text{Rh}})(\lambda_{97m\text{Rh}} - \lambda_{97\text{Rh}})(\lambda_{97\text{Ru}} - \lambda_{97\text{Rh}})} \\
 &\left. + \frac{\exp(-\lambda_{97\text{Ru}}t_b)}{(\varphi(\sigma_{\text{grd}} + \sigma_{\text{iso}}) - \lambda_{97\text{Ru}})(\lambda_{97m\text{Rh}} - \lambda_{97\text{Ru}})(\lambda_{97\text{Rh}} - \lambda_{97\text{Ru}})} \right\}
 \end{aligned} \tag{C.16}$$



$$\Lambda_1 = \varphi(\sigma_{\text{grd}} + \sigma_{\text{iso}}) \tag{C.18}$$

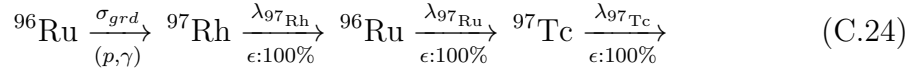
$$\Lambda_1^* = \varphi \sigma_{\text{iso}} \tag{C.19}$$

$$\Lambda_2 = \lambda_{97m\text{Rh}} \tag{C.20}$$

$$\Lambda_2^* = b_\epsilon \lambda_{97m\text{Rh}} \tag{C.21}$$

$$\Lambda_3 = \lambda_{97\text{Ru}} \tag{C.22}$$

$$\begin{aligned}
 N^2(t_b) = & N_1^0 \varphi \sigma_{\text{iso}} b_\epsilon \lambda_{97m\text{Rh}} \times \\
 & \left\{ \frac{\exp(-\varphi(\sigma_{\text{grd}} + \sigma_{\text{iso}})t_b)}{(\lambda_{97m\text{Rh}} - \varphi(\sigma_{\text{grd}} + \sigma_{\text{iso}}))(\lambda_{97\text{Ru}} - \varphi(\sigma_{\text{grd}} + \sigma_{\text{iso}}))} \right. \\
 & + \frac{\exp(-\lambda_{97m\text{Rh}}t_b)}{(\varphi(\sigma_{\text{grd}} + \sigma_{\text{iso}}) - \lambda_{97m\text{Rh}})(\lambda_{97\text{Ru}} - \lambda_{97\text{Rh}})} \\
 & + \frac{\exp(-\lambda_{97\text{Rh}}t_b)}{(\varphi(\sigma_{\text{grd}} + \sigma_{\text{iso}}) - \lambda_{97\text{Rh}})(\lambda_{97\text{Ru}} - \lambda_{97\text{Rh}})} \\
 & \left. + \frac{\exp(-\lambda_{97\text{Ru}}t_b)}{(\varphi(\sigma_{\text{grd}} + \sigma_{\text{iso}}) - \lambda_{97\text{Ru}})(\lambda_{97m\text{Rh}} - \lambda_{97\text{Ru}})} \right\} \quad (\text{C.23})
 \end{aligned}$$



$$\Lambda_1 = \varphi(\sigma_{\text{grd}} + \sigma_{\text{iso}}) \quad (\text{C.25})$$

$$\Lambda_1^* = \varphi \sigma_{\text{grd}} \quad (\text{C.26})$$

$$\Lambda_2 = \lambda_{97\text{Rh}} \quad (\text{C.27})$$

$$\Lambda_2^* = \lambda_{97\text{Rh}} \quad (\text{C.28})$$

$$\Lambda_3 = \lambda_{97\text{Ru}} \quad (\text{C.29})$$

$$\begin{aligned}
 N^3(t_b) = & N_1^0 \varphi \sigma_{\text{grd}} \lambda_{97\text{Rh}} \times \\
 & \left\{ \frac{\exp(-\varphi(\sigma_{\text{grd}} + \sigma_{\text{iso}})t_b)}{(\lambda_{97\text{Rh}} - \varphi(\sigma_{\text{grd}} + \sigma_{\text{iso}}))(\lambda_{97\text{Ru}} - \varphi(\sigma_{\text{grd}} + \sigma_{\text{iso}}))} \right. \\
 & + \frac{\exp(-\lambda_{97\text{Rh}}t_b)}{(\varphi(\sigma_{\text{grd}} + \sigma_{\text{iso}}) - \lambda_{97\text{Rh}})(\lambda_{97\text{Ru}} - \lambda_{97\text{Rh}})} \\
 & + \frac{\exp(-\lambda_{97\text{Rh}}t_b)}{(\varphi(\sigma_{\text{grd}} + \sigma_{\text{iso}}) - \lambda_{97\text{Rh}})(\lambda_{97\text{Ru}} - \lambda_{97\text{Rh}})} \\
 & \left. + \frac{\exp(-\lambda_{97\text{Ru}}t_b)}{(\varphi(\sigma_{\text{grd}} + \sigma_{\text{iso}}) - \lambda_{97\text{Ru}})(\lambda_{97\text{Rh}} - \lambda_{97\text{Ru}})} \right\} \quad (\text{C.30})
 \end{aligned}$$

$$N_{97\text{Ru}}(t_b) = N^1(t_b) + N^2(t_b) + N^3(t_b) \quad (\text{C.31})$$

Appendix D

Impact of different geometry parameters on the simulated efficiency

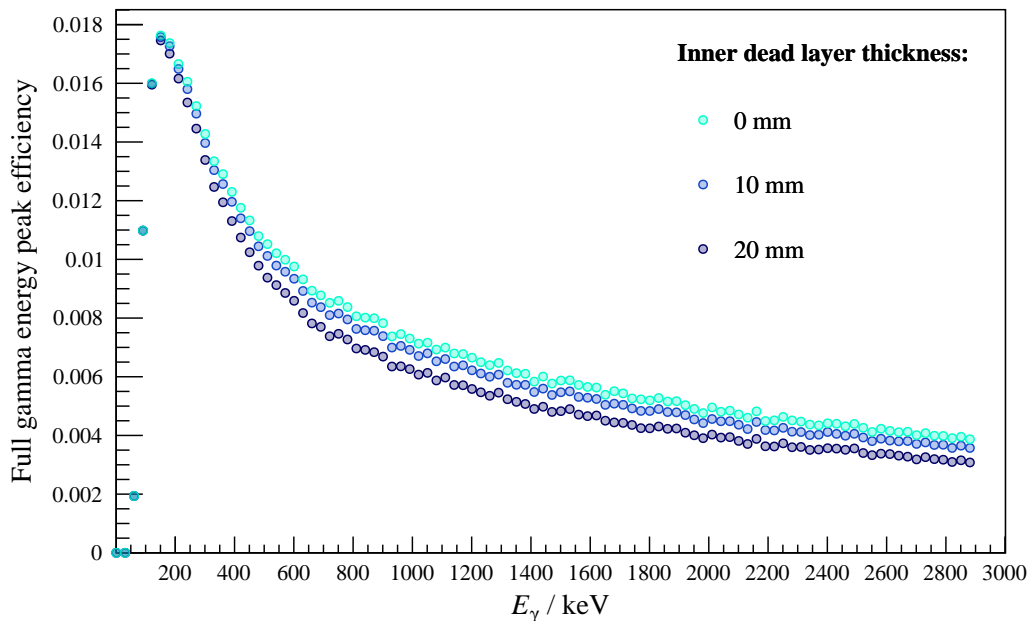


Figure D.1: Impact of the inner dead layer thickness on the ε_{FEP} .

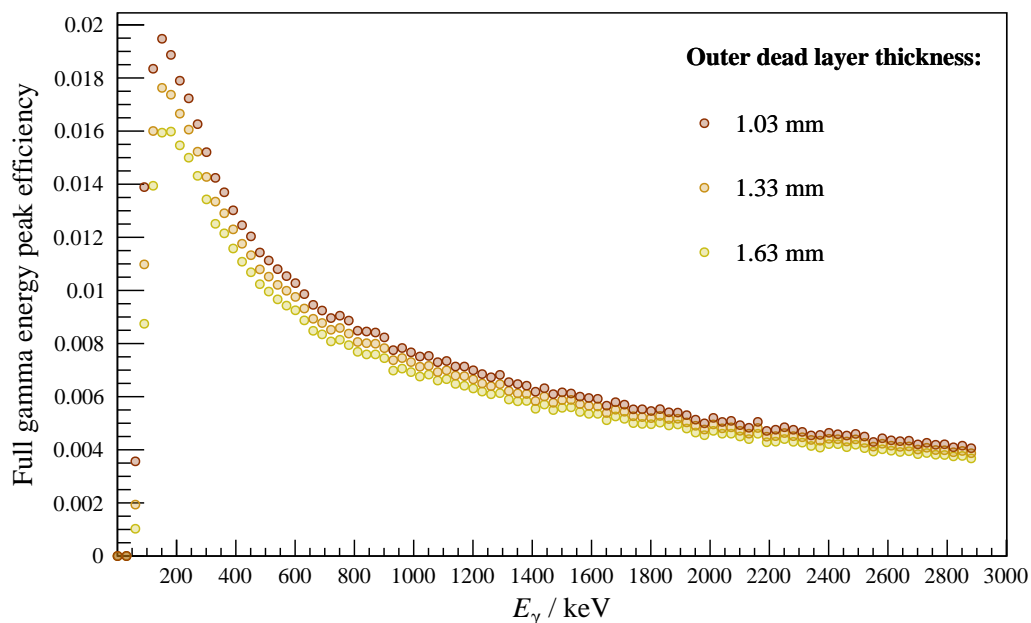


Figure D.2: Impact of the outer dead layer thickness on the ε_{FEP} .

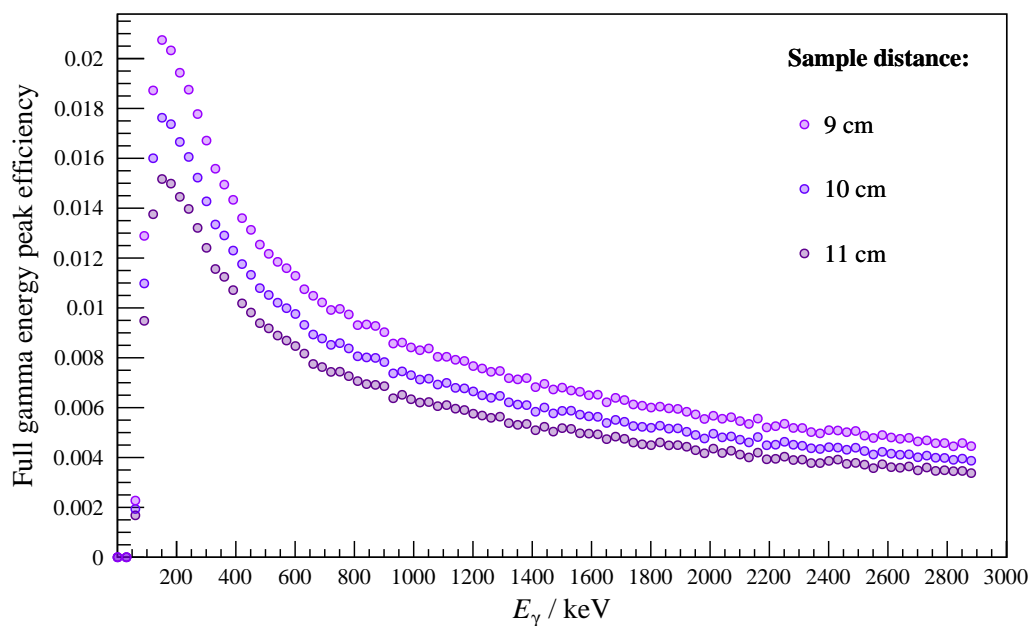


Figure D.3: Impact of sample distance on the ε_{FEP} .

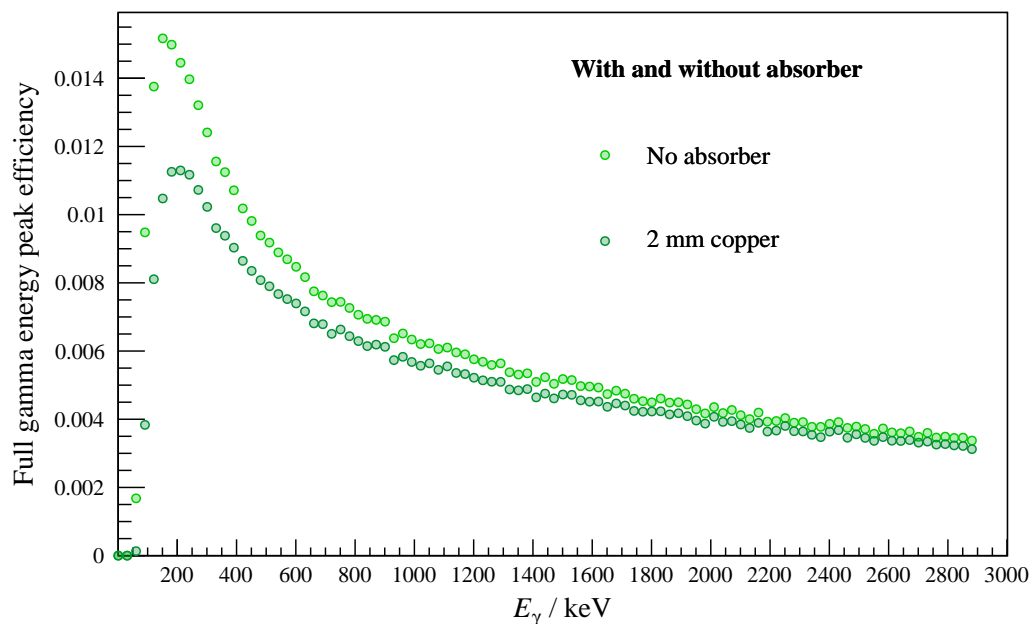


Figure D.4: The ε_{FEP} with and without a 2 mm absorber plate of copper.

Appendix E

Effective proton energies for the activation of ruthenium

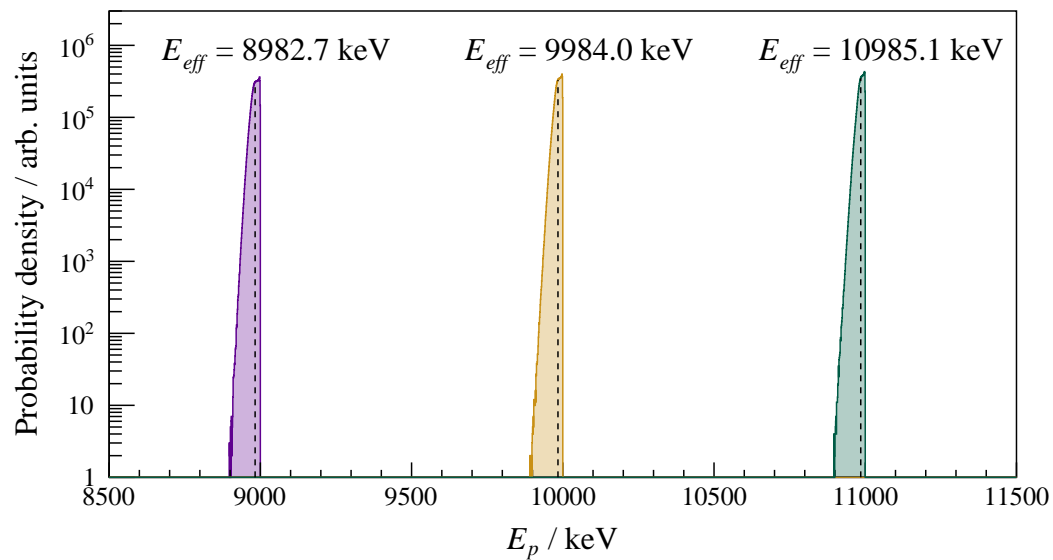


Figure E.1: Simulated effective proton energy distribution considering energy loss in the ruthenium layer for incident proton energies of 9 MeV, 10 MeV and 11 MeV.

Bibliography

- [1] Benjamin P Abbott et al. “GW170817: observation of gravitational waves from a binary neutron star inspiral”. In: *Physical review letters* 119.16 (2017), p. 161101.
- [2] Agostinelli et al. “GEANT4—a simulation toolkit”. In: *Nuclear instruments and methods in physics research section A: Accelerators, Spectrometers, Detectors and Associated Equipment* 506.3 (2003), pp. 250–303.
- [3] Bezshyiko et al. “Isomer Ratios for Products of Photonuclear Reactions $^{121}\text{Sb}(\gamma, 3n)$ $^{118}\text{m}, \text{g Sb}$ and $^{121}\text{Sb}(\gamma, 5n)$ $^{116}\text{m}, \text{g Sb}$ ”. In: *WDS'12 Proceedings of Contributed Papers* 3 (2012), pp. 147–151.
- [4] Daniel R Albert. *Monte Carlo uncertainty propagation with the NIST uncertainty machine*. 2020.
- [5] RP Anand et al. “25 keV-neutron capture cross-sections”. In: *Il Nuovo Cimento A (1971-1996)* 50.2 (1979), pp. 247–257.
- [6] OU Anders. “Determination of fluorine by neutron activation”. In: *Analytical Chemistry* 32.10 (1960), pp. 1368–1369.
- [7] Almudena Arcones, H-Th Janka, and L Scheck. “Nucleosynthesis-relevant conditions in neutrino-driven supernova outflows-I. Spherically symmetric hydrodynamic simulations”. In: *Astronomy & Astrophysics* 467.3 (2007), pp. 1227–1248.
- [8] WD Arnett and JW Truran. “Carbon-burning nucleosynthesis at constant temperature”. In: *The Astrophysical Journal* 157 (1969), p. 339.
- [9] Marcel Arnould and Stéphane Goriely. “The p-process of stellar nucleosynthesis: astrophysics and nuclear physics status”. In: *Physics Reports* 384.1-2 (2003), pp. 1–84.
- [10] Peter Axel. “Electric dipole ground-state transition width strength function and 7-MeV photon interactions”. In: *Physical Review* 126.2 (1962), p. 671.
- [11] Adriana Banu et al. “Photoneutron reaction cross section measurements on Mo 94 and Zr 90 relevant to the p-process nucleosynthesis”. In: *Physical Review C* 99.2 (2019), p. 025802.
- [12] Harry Bateman. “The solution of a system of differential equations occurring in the theory of radio-active transformations”. In: *Proc. Cambridge Phil. Soc., 1908* 15 (1908), pp. 423–427.
- [13] H Beer and F Käppeler. “Neutron capture cross sections on Ba 138, Ce 1 4 0, 1 4 2, Lu 1 7 5, 1 7 6, and Ta 181 at 30 keV: Prerequisite for investigation of the Lu 176 cosmic clock”. In: *Physical Review C* 21.2 (1980), p. 534.

- [14] Hermann Beer et al. “The fast cyclic neutron activation technique at the Karlsruhe 3.75 MV Van de Graaff accelerator and the measurement of the 107,109 Ag (n, γ) 108,110 Ag cross sections at kT= 25 keV”. In: *Nuclear Instruments and Methods in Physics Research Section A: Accelerators, Spectrometers, Detectors and Associated Equipment* 337.2-3 (1994), pp. 492–503.
- [15] Sara Bisterzo et al. “The branchings of the main s-process: their sensitivity to α -induced reactions on 13C and 22Ne and to the uncertainties of the nuclear network”. In: *Monthly Notices of the Royal Astronomical Society* 449.1 (2015), pp. 506–527.
- [16] Jean Blachot. “Nuclear data sheets for A = 108”. In: *Nuclear Data Sheets* 91.2 (2000), pp. 135–296.
- [17] Jean Blachot. “Nuclear data sheets for A= 104”. In: *Nuclear Data Sheets* 108.10 (2007), pp. 2035–2172.
- [18] AM Boesgaard. “Stellar abundances of lithium, beryllium, and boron.” In: *Publications of the Astronomical Society of the Pacific* 88.524 (1976), p. 353.
- [19] O Bohigas, RU Haq, and A Pandey. “Nuclear data for science and technology”. In: *Reidel, Dordrecht* (1983), p. 809.
- [20] JK Böhlke et al. “Isotopic compositions of the elements, 2001”. In: *Journal of Physical and Chemical Reference Data* 34.1 (2005), pp. 57–67.
- [21] Niels Bohr. “Neutron capture and nuclear constitution”. In: *Nature* 137.3461 (1936), pp. 344–348.
- [22] MV Bokhovko et al. *Measurement of the neutron radiative capture cross-sections for silver in the energy region 4-400 keV*. Tech. rep. 1988.
- [23] J Bork et al. “Proton capture cross sections of the ruthenium isotopes”. In: *Physical Review C* 58.1 (1998), p. 524.
- [24] DM Brink. “Individual particle and collective aspects of the nuclear photoeffect”. In: *Nuclear Physics* 4 (1957), pp. 215–220.
- [25] Benjamin Brückner et al. “Investigation of the 7Li (p, n) neutron fields at high energies”. In: *Journal of Physics: Conference Series*. Vol. 1668. 1. IOP Publishing. 2020, p. 012003.
- [26] E Margaret Burbidge et al. “Synthesis of the elements in stars”. In: *Reviews of modern physics* 29.4 (1957), p. 547.
- [27] Allan D Carlson et al. “Recent work leading towards a new evaluation of the neutron standards”. In: *Nuclear Data Sheets* 123 (2015), pp. 27–35.
- [28] Tyler B Coplen et al. “The Table of Standard Atomic Weights—an exercise in consensus”. In: *Rapid Communications in Mass Spectrometry* (2020), e8864.
- [29] Richard G Couch, Ann B Schmiedekamp, and W David Arnett. “S-PROCESS nucleosynthesis in massive stars: core helium burning”. In: *The Astrophysical Journal* 190 (1974), pp. 95–100.
- [30] FCL Crespi et al. “HPGe detectors timing using pulse shape analysis techniques”. In: *Nuclear Instruments and Methods in Physics Research Section A: Accelerators, Spectrometers, Detectors and Associated Equipment* 620.2-3 (2010), pp. 299–304.

- [31] John R De Laeter et al. “Atomic weights of the elements. Review 2000 (IUPAC Technical Report)”. In: *Pure and applied chemistry* 75.6 (2003), pp. 683–800.
- [32] Sophia Dellmann. “Messung des Protoneneinfangs an ^{118}Te am ESR - GSI”. In: *PHD thesis* (2022).
- [33] Yang Dong and Huo Junde. “Nuclear data sheets for $A = 52$ ”. In: *Nuclear Data Sheets* 128 (2015), pp. 185–314.
- [34] Carla Fröhlich. “Supernovae, neutrinos, and nucleosynthesis”. In: *Journal of Physics G: Nuclear and Particle Physics* 41.4 (2014), p. 044003.
- [35] Carl Friedrich Gauss. *Theoria combinationis observationum erroribus minimis obnoxiae*. Vol. 2. H. Dieterich, 1823.
- [36] WW Givens, WR Mills, and RL Caldwell. “Cyclic activation analysis”. In: *Nuclear Instruments and Methods* 80.1 (1970), pp. 95–103.
- [37] RW Gladen et al. “Efficient machine learning approach for optimizing the timing resolution of a high purity germanium detector”. In: *Nuclear Instruments and Methods in Physics Research Section A: Accelerators, Spectrometers, Detectors and Associated Equipment* 981 (2020), p. 164505.
- [38] J Glorius et al. “Approaching the Gamow Window with Stored Ions: Direct Measurement of $X e 124$ (p, γ) in the ESR Storage Ring”. In: *Physical Review Letters* 122.9 (2019), p. 092701.
- [39] Stéphane Goriely. “Radiative neutron captures by neutron-rich nuclei and the r-process nucleosynthesis”. In: *Physics Letters B* 436.1-2 (1998), pp. 10–18.
- [40] Stéphane Goriely et al. “The r-process nucleosynthesis: a continued challenge for nuclear physics and astrophysics”. In: *Nuclear Physics A* 758 (2005), pp. 587–594.
- [41] Joint Committee for Guides in Metrology. “Evaluation of measurement data — Guide to the expression of uncertainty in measurement.” In: *International Bureau of Weights and Measures (BIPM), Sèvres, France, 2011* (2008), p. 2. DOI: www.bipm.org/en/publications/guides/gum.html.
- [42] Joint Committee for Guides in Metrology. “Evaluation of measurement data — Supplement 2 to the “Guide to the expression of uncertainty in measurement” — Extension to any number of output quantities”. In: *International Bureau of Weights and Measures (BIPM), Sèvres, France, 2011* (2008). DOI: www.bipm.org/en/publications/guides/gum.html.
- [43] G Gürdal and FG Kondev. “Nuclear data sheets for $A = 110$ ”. In: *Nuclear Data Sheets* 113.5 (2012), pp. 1315–1561.
- [44] Gy Gyürky et al. “The activation method for cross section measurements in nuclear astrophysics”. In: *The European Physical Journal A* 55.3 (2019), pp. 1–31.
- [45] W Raphael Hix and F-K Thielemann. “Silicon Burning I: Neutronization and the Physics of Quasi-Equilibrium”. In: *arXiv preprint astro-ph/9511088* (1995).
- [46] Xiaolin Hou. “Cyclic activation analysis”. In: *Encyclopedia of Analytical Chemistry: Applications, Theory and Instrumentation* (2006).

- [47] NQ Huy, DQ Binh, and VX An. “Study on the increase of inactive germanium layer in a high-purity germanium detector after a long time operation applying MCNP code”. In: *Nuclear Instruments and Methods in Physics Research Section A: Accelerators, Spectrometers, Detectors and Associated Equipment* 573.3 (2007), pp. 384–388.
- [48] Christian Iliadis. *Nuclear Physics of Stars* Wiley. 2007.
- [49] *Institute Nuclear Astrophysics - Website*. URL: <https://isnap.nd.edu/research/facility/> (visited on 03/02/2022).
- [50] Hans-Thomas Janka. “Explosion mechanisms of core-collapse supernovae”. In: *Annual Review of Nuclear and Particle Science* 62 (2012), pp. 407–451.
- [51] Hao Jiang et al. “Measurement of the dead layer thickness in a p-type point contact germanium detector”. In: *Chinese Physics C* 40.9 (2016), p. 096001.
- [52] AC Kahler et al. “ENDF/B-VII. 1 neutron cross section data testing with critical assembly benchmarks and reactor experiments”. In: *Nuclear Data Sheets* 112.12 (2011), pp. 2997–3036.
- [53] Franz Käppeler et al. “The s process: Nuclear physics, stellar models, and observations”. In: *Reviews of Modern Physics* 83.1 (2011), p. 157.
- [54] Stephen J Kline. “Describing uncertainty in single sample experiments”. In: *Mech. Engineering* 75 (1953), pp. 3–8.
- [55] D Kolev et al. “A convenient method for experimental determination of yields and isomeric ratios in photonuclear reactions measured by the activation technique”. In: *Nuclear Instruments and Methods in Physics Research Section A: Accelerators, Spectrometers, Detectors and Associated Equipment* 356.2-3 (1995), pp. 390–396.
- [56] AJ Koning et al. “TENDL: complete nuclear data library for innovative nuclear science and technology”. In: *Nuclear Data Sheets* 155 (2019), pp. 1–55.
- [57] Motohiko Kusakabe et al. “Supernova neutrino process of Li and B revisited”. In: *The Astrophysical Journal* 872.2 (2019), p. 164.
- [58] Thomas Lafarge and Antonio Possolo. “The NIST uncertainty machine”. In: *NCSLI Measure* 10.3 (2015), pp. 20–27.
- [59] Ann-Cecilie Larsen et al. “Novel techniques for constraining neutron-capture rates relevant for r-process heavy-element nucleosynthesis”. In: *Progress in Particle and Nuclear Physics* 107 (2019), pp. 69–108.
- [60] Truong Thi Hong Loan et al. “Determination of the dead-layer thickness for both p- and n-type HPGe detectors using the two-line method”. In: *Journal of Radioanalytical and Nuclear Chemistry* 315.1 (2018), pp. 95–101.
- [61] K Lodders, H Palme, and H-P Gail. “Abundances of the elements in the solar system”. In: *arXiv preprint arXiv:0901.1149* (2009).
- [62] RL Macklin. “Neutron Capture Cross Sections of the Silver Isotopes 107ag and 109ag from 2.6 to 2000 keV”. In: *Nuclear Science and Engineering* 82.4 (1982), pp. 400–407.

- [63] M Mayer and M Bliss. “Optimization of lithium-glass fibers with lithium depleted coating for neutron detection”. In: *Nuclear Instruments and Methods in Physics Research Section A: Accelerators, Spectrometers, Detectors and Associated Equipment* 930 (2019), pp. 37–41.
- [64] Bo Mei et al. “First measurement of the Ru 96 (p, γ) Rh 97 cross section for the p process with a storage ring”. In: *Physical Review C* 92.3 (2015), p. 035803.
- [65] Paul W Merrill. “Spectroscopic observations of stars of class”. In: *The Astrophysical Journal* 116 (1952), p. 21.
- [66] *National Electrostatics Corp. - Website*. URL: <https://www.pelletron.com/products/pelletron-charging-chains/> (visited on 03/04/2022).
- [67] *National Nuclear Data Center (2022), data retrieved from NuDat3 database*. URL: <https://www.nndc.bnl.gov/nudat3/> (visited on 03/01/2022).
- [68] N Nishimura et al. “Uncertainties in the production of p nuclides in thermonuclear supernovae determined by Monte Carlo variations”. In: *Monthly Notices of the Royal Astronomical Society* 474.3 (2018), pp. 3133–3139.
- [69] Keith A Olive, Gary Steigman, and Terry P Walker. “Primordial nucleosynthesis: Theory and observations”. In: *Physics Reports* 333 (2000), pp. 389–407.
- [70] Richard H Pehl et al. “Radiation damage resistance of reverse electrode Ge coaxial detectors”. In: *IEEE Transactions on Nuclear Science* 26.1 (1979), pp. 321–323.
- [71] M Pignatari et al. “The weak s-process in massive stars and its dependence on the neutron capture cross sections”. In: *The Astrophysical Journal* 710.2 (2010), p. 1557.
- [72] Marco Pignatari et al. “The s-process in massive stars: the Shell C-burning contribution”. In: *PoS* (2006), p. 061.
- [73] CM Raiteri et al. “S-process nucleosynthesis in massive stars and the weak component. I-Evolution and neutron captures in a 25 solar mass star”. In: *The Astrophysical Journal* 367 (1991), pp. 228–238.
- [74] T Rauscher et al. “Nucleosynthesis in massive stars with improved nuclear and stellar physics”. In: *The Astrophysical Journal* 576.1 (2002), p. 323.
- [75] Thomas Rauscher and F-K Thielemann. “Astrophysical reaction rates from statistical model calculations”. In: *arXiv preprint astro-ph/0004059* (2000).
- [76] M Rayet et al. “The p-process in Type II supernovae.” In: *Astronomy and Astrophysics* 298 (1995), p. 517.
- [77] Hubert Reeves. “On the origin of the light elements ($Z_i \leq 6$)”. In: *Reviews of Modern Physics* 66.1 (1994), p. 193.
- [78] R Reifarth, C Lederer, and F Käppeler. “Neutron reactions in astrophysics”. In: *Journal of Physics G: Nuclear and Particle Physics* 41.5 (2014), p. 053101.
- [79] René Reifarth and Yuri A Litvinov. “Measurements of neutron-induced reactions in inverse kinematics”. In: *Physical Review Special Topics-Accelerators and Beams* 17.1 (2014), p. 014701.

- [80] René Reifarh et al. “Neutron-induced cross sections—from raw data to astrophysical rates”. In: *The European Physical Journal Plus* 133.10 (2018), p. 424.
- [81] René Reifarh et al. “PINO—a tool for simulating neutron spectra resulting from the ${}^7\text{Li}$ (p, n) reaction”. In: *Nuclear Instruments and Methods in Physics Research Section A: Accelerators, Spectrometers, Detectors and Associated Equipment* 608.1 (2009), pp. 139–143.
- [82] Keiichi Shibata et al. “JENDL-4.0: a new library for nuclear science and engineering”. In: *Journal of Nuclear Science and Technology* 48.1 (2011), pp. 1–30.
- [83] Zuzana Slavkovska, Jan Glorius, and Christoph Langer. “Astrophysics with storage rings. 124 Xe beam at ESR”. In: *Verhandlungen der Deutschen Physikalischen Gesellschaft* (2017).
- [84] N Spyrou. “Cyclic activation analysis—A review”. In: *Journal of Radioanalytical and Nuclear Chemistry* 61.1-2 (1981), pp. 211–242.
- [85] Gary Steigman. “Primordial nucleosynthesis in the precision cosmology era”. In: *arXiv preprint arXiv:0712.1100* (2007).
- [86] Benedikt Thomas et al. “Production of ${}^{91}\text{Nb}$ for a measurement of the ${}^{91}\text{Nb}$ (p, γ) reaction at FRANZ”. In: *XIII Nuclei in the Cosmos (NIC XIII)* (2014), p. 168.
- [87] C Travaglio et al. “Role of core-collapse supernovae in explaining solar system abundances of p nuclides”. In: *The Astrophysical Journal* 854.1 (2018), p. 18.
- [88] Meiko Volkmandt. “Neutroneneinfangsreaktionen kurzlebiger Isotope”. In: *PHD thesis* (2022).
- [89] George Wallerstein et al. “Synthesis of the elements in stars: forty years of progress”. In: *Reviews of Modern Physics* 69.4 (1997), p. 995.
- [90] RR Winters, RL Macklin, and J Halperin. “ ${}^{51}\text{V}(n, \gamma)$ reaction in the keV incident neutron energy range”. In: *Physical Review C* 18.5 (1978), p. 2092.
- [91] SE Woosley and WM Howard. “The p-process in supernovae”. In: *The Astrophysical Journal Supplement Series* 36 (1978), pp. 285–304.
- [92] James F Ziegler, Matthias D Ziegler, and Jochen P Biersack. “SRIM—The stopping and range of ions in matter (2010)”. In: *Nuclear Instruments and Methods in Physics Research Section B: Beam Interactions with Materials and Atoms* 268.11-12 (2010), pp. 1818–1823.